

3-2020

## Theoretical and Computational Analyses on Transition and Turbulence in Purely Oscillating Pipe Flow

Ali Ahmed Abdulrasool

Follow this and additional works at: <https://commons.erau.edu/edt>



Part of the [Computer Engineering Commons](#), and the [Mechanical Engineering Commons](#)

---

This Dissertation - Open Access is brought to you for free and open access by Scholarly Commons. It has been accepted for inclusion in Dissertations and Theses by an authorized administrator of Scholarly Commons. For more information, please contact [commons@erau.edu](mailto:commons@erau.edu).

THEORETICAL AND COMPUTATIONAL ANALYSES ON  
TRANSITION AND TURBULENCE IN PURELY  
OSCILLATING PIPE FLOW

*A Dissertation*

*Submitted to the Faculty*

*of*

Embry-Riddle Aeronautical University

*by*

Ali Ahmed Abdulrasool

*In Partial Fulfillment of the Requirements for the Degree of*

*Doctor of Philosophy in Mechanical Engineering*

March 2020

Daytona Beach, Florida

THEORETICAL AND COMPUTATIONAL ANALYSES ON TRANSITION  
AND TURBULENCE IN PURELY OSCILLATING PIPE FLOW

by

Ali Ahmed Abdurassool

This dissertation was prepared under the direction of the candidate's committee chairman, Dr. Yongho Lee, Department of Mechanical Engineering, and has been approved by the members of the dissertation committee. It was submitted to the College of Engineering and was accepted in partial fulfillment of the requirements for the degree of

Doctor of Philosophy in Mechanical Engineering

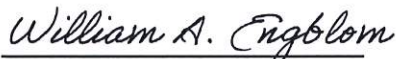
DISSERTATION COMMITTEE



Chairman, Dr. Yongho Lee



Member, Dr. Eduardo Divo



Member, Dr. William Engblom



Member, Dr. Bertrand Rollin



Member, Dr. Birce Dikici



Graduate Program Coordinator, Dr. Eric Coyle

4/20/2020

Date



Department Chair, Dr. Eduardo Divo

4/16/2020

Date



Dean of the College of Engineering, Dr. Maj  
Mirmirani

04/20/2020

Date



Senior Vice President for Academic Affairs and  
Provost, Dr. Lon Moeller

4/20/2020

Date

## Abstract

The hydrodynamic instability of purely oscillating pipe flows is investigated in terms of the quasi-steady formulation assuming the temporal changes of the laminar base flow relative to disturbances are slow. A simple model equation is introduced to compare the exact solution of the current approach with those of the major theories dedicated for unsteady flows. The results of the analysis show that the quasi-steady assumption and the multiple scales method are more efficient and accurate than the formal Floquet theory in predicting the transient instabilities within a period in addition to the long-term growth or decay of disturbances. The most significant contribution of the present quasi-steady analysis is the neutral stability curves, from which the critical Reynolds numbers are obtained for a wide range of oscillation frequencies. The stability criterion pertains to the cycle-averaged growth rates obtained from the eigenvalues of the parametric stability problem. Moreover, the approximate accuracy of the quasi-steadiness is assessed by proposing a new mathematical relation, confirming the validity of the method for the stability analysis. The theoretical findings are consistent with some experimental results although some others show quantitative discrepancies, which can be attributed mostly to the deviations in the second spatial derivative of base flow.

In the computational analyses of this research, direct numerical simulations (DNS) based on the spectral element method are performed to verify the theoretical predictions and to accurately examine the transition to turbulence. The onset of transition in smooth pipe, identified as a disturbed laminar flow after imposing small random perturbations as initial conditions, qualitatively agrees with that estimated by the quasi-steady theory. The later

transition stage at which the turbulence and relaminarization phenomena first emerge is detected from the high-amplitude velocity fluctuations. The turbulence intensity increases with the Stokes number proportional to oscillation frequency. Furthermore, surface roughness constructed utilizing the overset-grid technique is also considered as the triggering mechanism to induce transition and turbulence with small wavy imperfections distributed along the inner wall of a pipe. The influence of the surface roughness on flow stability is evaluated and the critical Reynolds number is close to that of the smooth pipe unless the roughness height is large. The friction coefficients at a few flow conditions for both smooth and rough pipes are determined according to the maximum values of the wall shear stress and found to be compatible with those shown by experiments in the literature.

*“Stay soaring with the eagles, never be dragged to the ground”*



*“The more you keep producing, the longer your life will be”*



*“Engineering is meant to simplify things, so do not make it complicated”*



With genuine gratefulness and warmest regard, my wife and I dedicate this  
work to our family members without whom nothing would happen.

## Acknowledgements

First and foremost, I thank God Almighty for the blessings He has bestowed upon us. I would like to thank my wife for her patience throughout my entire journey of pursuing a doctorate degree abroad. She is incredible, and I could not do anything without her support. Last but not least, I am grateful to my parents and my younger brother for their support and encouragement to let me follow my dream. I would like to thank my little brother and my older sisters for supporting me spiritually throughout the study period.

I would like to acknowledge the Higher Committee for Education Development (HCED) in Iraq and Kerbala University (the Iraqi Ministry of Higher Education and Scientific Research) for providing financial support during this research. I would like to express my profound gratitude to my advisor Dr. Yongho Lee for his enormous patience, immense knowledge, and tremendous effort to introduce me first to the world of the computational fluid Dynamics (CFD) and to motivate me completing a doctoral degree in this field. His guidance helped me in all the time of research and writing of this dissertation. I could not have imagined having a better advisor and mentor for my PhD study than him.

Besides my advisor, I would like to thank the rest of my dissertation committee: Dr. Eduardo Divo, Dr. William Engblom, Dr. Bertrand Rollin and Dr. Birce Dikici not only for their insightful comments and encouragement, but also for their pieces of advice which made me widening my research in var-

ious perspectives. A special thank to Dr. Eduardo Divo for teaching me all the fundamentals to algorithms and numerical studies during my first year of university. I am grateful to Dr. Bertrand Rollin for enlightening me the first glance of this research, and I could not have accomplished my study goals without his valuable advice. My sincere thanks also go to Dr. William Engblom and Mr. Scott Hicks, who gave me an opportunity to work on the clustered systems installed in one of our college facilities. I would like to thank Dr. Birce Dikici and Dr. Reda Mankbadi for the stimulating discussions and for teaching me other essential study materials. I would like to thank my friends, Yuan Tian and Isabel McBrayer, for accepting nothing less than excellence from me.



# Contents

<b>Title</b>	<b>i</b>
<b>Abstract</b>	<b>i</b>
<b>List of Figures</b>	<b>vii</b>
<b>List of Tables</b>	<b>xii</b>
<b>Nomenclature</b>	<b>xiv</b>
<b>1 Introduction</b>	<b>1</b>
<b>2 Linear Stability Theories</b>	<b>10</b>
2.1 Overview . . . . .	10
2.2 Analysis . . . . .	12
2.2.1 Floquet method for the model equation and its extension . . . . .	18
2.2.2 Multiple scales method applied to the model equation . . . . .	20
2.2.3 Present method for the model equation (quasi-steady method) . . . . .	22
2.2.4 Extension to the hydrodynamic stability problem . . . . .	25
2.2.5 Transformation of the hydrodynamic stability problem . . . . .	28
2.2.5.1 Chebyshev polynomials . . . . .	30
2.2.5.2 Chebyshev Derivatives . . . . .	31
2.3 Results and Discussions . . . . .	33
2.3.1 Flow stability by the quasi-steady method . . . . .	33
2.3.2 Approximate accuracy of the quasi-steady method . . . . .	44

<b>3</b>	<b>Transition in Purely Oscillating Pipe Flow</b>	<b>47</b>
3.1	Overview . . . . .	47
3.2	Governing equations . . . . .	48
3.3	Numerical solver . . . . .	49
3.4	CFD code validation . . . . .	50
3.5	Grid convergence analysis . . . . .	51
3.6	Results and Discussions . . . . .	56
3.6.1	Critical Reynolds numbers estimated by DNS . . . . .	56
3.6.2	The onset of transition . . . . .	61
<b>4</b>	<b>Turbulence in Purely Oscillating Pipe Flow</b>	<b>67</b>
4.1	Overview . . . . .	67
4.2	Mesh modeling . . . . .	69
4.3	Implementation process . . . . .	71
4.3.1	Kolmogorov length scale . . . . .	72
4.3.2	Grid convergence for turbulent flows . . . . .	74
4.3.3	Grid Resolution in terms of wall units . . . . .	77
4.3.4	The length of the computational domain . . . . .	78
4.4	Parallel computing . . . . .	79
4.5	Results and discussions . . . . .	79
4.5.1	Flow behavior at $Re_\delta = 400$ . . . . .	79
4.5.2	Flow behavior at $Re_\delta = 800$ . . . . .	83
4.5.3	Wall shear stress (WSS) . . . . .	85
4.5.4	Turbulence intensity . . . . .	90
4.5.5	Turbulence kinetic energy (TKE) . . . . .	92
4.5.6	Spatial autocorrelation function . . . . .	93
4.5.7	One-dimensional energy spectra . . . . .	96
4.5.8	Vortices in the turbulent flow . . . . .	99
4.5.9	Velocity profiles in terms of wall units . . . . .	100

4.5.10	Oscillating pressure field . . . . .	101
<b>5</b>	<b>Roughness-induced Transition and Turbulence</b>	<b>103</b>
5.1	Overview . . . . .	103
5.2	Overset grid . . . . .	105
5.2.1	Surface roughness parametrization . . . . .	106
5.2.2	Grid convergence study and implementation . . . . .	108
5.3	Laminar flows with rough wall . . . . .	109
5.4	Transitional flows with rough wall . . . . .	111
5.5	Turbulent flows with rough wall . . . . .	113
5.6	Time-dependent wall shear stress ( $\tau_w^*$ ) . . . . .	119
5.7	Friction coefficient ( $C_f$ ) . . . . .	121
5.8	Vorticity in the presence of surface roughness . . . . .	123
<b>6</b>	<b>Conclusions and Recommendations</b>	<b>125</b>
6.1	Conclusions . . . . .	125
6.2	Future work . . . . .	128
	<b>References</b>	<b>130</b>
	<b>Appendices</b>	<b>139</b>

# List of Figures

1.1	Axial velocity magnitudes ( $ u^* $ ) at five different radial positions ( $\zeta$ ), taken from <a href="#">Hino <i>et al.</i> (1976)</a> 's experiment for one oscillation cycle. . . . .	6
2.1	Exact solutions (blue solid and green dashed curves) of Eqn. (2.14) combined with the growth rate, $\text{Im}[\omega(t)] \times 10^{-2}$ , predicted using the quasi-steady method (red dash-dotted curve) for $a(t) = \sin(t)$ , $\xi(0) = 0.01$ , and $0 \leq t \leq 10T$ : blue solid curve; $b = -0.05$ , green dashed curve; $b = 0$ . . . . .	24
2.2	Chebyshev points obtained by the projection of radially equispaced points on a horizontal line as shown by <a href="#">Trefethen (2000)</a> . . . . .	31
2.3	Results of quasi-steady method represented by instantaneous growth rates during a cycle at $\lambda = 20$ and $\kappa = 8$ : $Re_\delta = 80, 125$ and $250$ for blue dash-dotted, green dashed and red solid curves, respectively. The green circles are the peaks at $Re_\delta = 500$ , and the red squares are the peaks at $Re_\delta = 1000$ . . . . .	35
2.4	Time variation of the laminar base flow velocity at the axis of symmetry (blue dash-dotted curve) and its derivatives at the wall (green dashed and red solid curves for the first and second derivatives, respectively) for $\lambda = 20$ and $Re_\delta = 250$ . The circles are the near-wall velocity overshoot due to Richardson's annular effect. . . . .	37
2.5	Neutral stability curves for six values of $\lambda$ ranging from 5.5 to 60, computed by the cycle-averaged growth rates. Note the different scales in (a) and (b). . . . .	39
2.6	Critical Reynolds numbers calculated by the cycle-averaged growth rates of quasi-steady assumption (green circles) compared with those of <a href="#">Kurzweg <i>et al.</i> (1989)</a> 's experiment (blue solid curve), Floquet analysis of <a href="#">Blennerhassett &amp; Bassom (2006)</a> (red squares), and 'Other experimental data' compiled by <a href="#">Cooper <i>et al.</i> (1993)</a> (bounded area between the two arrows). . . . .	40

3.1	The laminar velocity at the flow condition of $Re_\delta = 100$ and $\lambda = 10$ predicted by Nek5000 using the driving force concept at five different times during a cycle, compared with that of the exact solution of <a href="#">Sexl (1930)</a> . . . . .	51
3.2	The profiles of $U_{\text{rms}}$ produced by the two-dimensional axisymmetric simulations of the oscillating flows performed at $Re_\delta = 250$ and $\lambda = 10$ using four different numbers of elements, $E$ , and a polynomial degree of $N = 7$ . The velocity statistics are taken at the mid-plane of the pipe. . . . .	53
3.3	The normalized residuals of the velocity vector, $\mathbf{u}$ , in terms of the number of iterations with the polynomial degree of $N = 7$ ; two-dimensional axisymmetric simulations at $Re_\delta = 250$ and $\lambda = 10$ with four different values of the number of elements, $E$ . . . . .	54
3.4	Computational mesh used for three-dimensional flow simulations at $Re_\delta = 200$ and $\lambda = 20$ with the polynomial of degree 7, and the number of elements, $E$ , are $11 \times 16 \times 9$ in the radial, azimuthal, and axial direction, respectively: (a) a quarter of a cross-sectional view and (b) the longitudinal view. . . . .	55
3.5	A comparison of the critical Reynolds numbers: blue solid diamonds — present DNS results (2-D), blue open circles — theoretical results of the present method (quasi-steady), red open squares — Floquet analysis of <a href="#">Blennerhassett &amp; Bassom (2006)</a> , red dash-dotted curve — Floquet analysis of <a href="#">Thomas et al. (2012)</a> , blue dashed curve — experiments of <a href="#">Kurzweg et al. (1989)</a> , blue open triangles — experiments of <a href="#">Lodahl et al. (1998)</a> , green solid triangle — turbulent flow (3-D DNS) of <a href="#">Feldmann &amp; Wagner (2012)</a> , green open triangle — laminar flow (3-D DNS) of <a href="#">Feldmann &amp; Wagner (2012)</a> , red solid triangles — conditionally turbulent flows of <a href="#">Hino et al. (1976)</a> , blue solid line — critical $Re_\delta$ of weakly turbulent flows of <a href="#">Hino et al. (1976)</a> . The experimental data compiled by <a href="#">Cooper et al. (1993)</a> for $\lambda > 7.07$ and those of <a href="#">Eckmann &amp; Grotberg (1991)</a> are located between the two black horizontal arrows. . . . .	57
3.6	Time-dependent axial velocity obtained by the two-dimensional axisymmetric DNS at the center plane between the two ends of the pipe and the exact laminar flow solution for the critical condition of $Re_\delta = 213$ and $\lambda = 10$ (see Tab. <a href="#">3.1</a> ). . . . .	63
3.7	Time-dependent axial velocities at the center plane between the two ends of the pipe for an unstable flow condition of $Re_\delta = 250$ and $\lambda = 10$ by: (a) the two-dimensional axisymmetric DNS and (b) the three-dimensional DNS. . . . .	64

3.8	Longitudinal and cross-sectional contour plots of the three components of velocity (m/s): (a) the axial velocity at $\tau/T = 1/8$ , (b) the axial velocity at $\tau/T = 3/8$ , (c) the radial velocity at $\tau/T = 3/8$ , and (d) the azimuthal velocity at $\tau/T = 3/8$ . The flow conditions are $Re_\delta = 250$ and $\lambda = 10$ . . . . .	66
4.1	Computational mesh with the GP3 resolution utilized for the flow condition of $Re_\delta = 400$ and $\lambda = 10$ : (a) a half of the cross-sectional view and (b) a half of the longitudinal view. . . . .	71
4.2	Kolmogorov length scales in $\mu\text{m}$ from the simulations with the GP4 mesh resolution at $\lambda = 10$ and: (a) $Re_\delta = 400$ and (b) $Re_\delta = 800$ . . . . .	73
4.3	RMS fluctuation velocities with respect to $\zeta$ , showing the grid convergence for the simulations performed with the four resolutions at $\lambda = 10$ and: (a) $Re_\delta = 400$ and (b) $Re_\delta = 800$ . . . . .	76
4.4	Instantaneous axial velocities with $Re_\delta = 800$ and $\lambda = 10$ at two locations: (a) $Z = 0$ and (b) $Z = 10$ , where $Z = z^*/R^*$ . . . . .	78
4.5	The temporal evolutions of the axial velocity at different radial positions ( $\zeta = 0, 0.9, 0.95$ and $0.99$ ) viewed at a cross section midway along the pipe with $Re_\delta = 400$ and $\lambda = 10$ and computed using the GP4 mesh. . . . .	80
4.6	The temporal evolutions of the axial velocities at one radial position ( $\zeta = 0.99$ ) viewed at a cross section midway along the pipe for three different values of $\lambda$ : (a) 10, (b) 20 and (c) 25. . . . .	82
4.7	The contour plots of the axial velocity at $Re_\delta = 400$ and $\lambda = 10$ using the GP4 mesh during: (a) the acceleration phase and (b) the deceleration phase. . . . .	83
4.8	The temporal evolutions of the axial velocity at different radial positions ( $\zeta = 0, 0.9, 0.95$ and $0.99$ ) viewed at a cross section midway along the pipe with $Re_\delta = 800$ and $\lambda = 10$ and computed using the GP4 mesh. . . . .	84
4.9	The contour plots of the axial velocity at $Re_\delta = 800$ and $\lambda = 10$ using the GP4 mesh during: (a) the acceleration phase and (b) the deceleration phase. . . . .	85
4.10	The time-dependent wall shear stresses at $\lambda = 10$ and: (a) $Re_\delta = 400$ and (b) $Re_\delta = 800$ ; the DNS result (red curve) and the laminar solution (black curve). . . . .	86
4.11	The profiles of the wall shear stress at flow conditions of $Re_\delta = 400$ and three Stokes numbers: (a) $\lambda = 10$ , (b) $\lambda = 20$ , and (c) $\lambda = 25$ . . . . .	89

4.12	Experimental validation for the present DNS result in terms of the wall shear stress utilizing <a href="#">Lodahl <i>et al.</i> (1998)</a> 's data at flow conditions of $Re_\delta = 600$ and $\lambda = 53$ (red); the wall shear stress of the present DNS (blue) is scaled by a factor of 0.0165. . . . .	90
4.13	Turbulence kinetic energy per unit mass computed at the two flow conditions of $Re_\delta = 400$ and $800$ for $\lambda = 10$ . . . . .	93
4.14	Spatial autocorrelation functions for a turbulent signal taken along the $z$ -direction from $Z = 5$ to $10$ at: (a) $\zeta = 0$ , (b) $\zeta = 0.9$ and (c) $\zeta = 0.9$ ; the flow conditions are $Re_\delta = 800$ and $\lambda = 10$ for the time-averaged quantities of three intervals at: acceleration phase (AP), deceleration phase (DP) and late deceleration phase (LD). . . . .	95
4.15	Energy spectrum of a turbulent signal along the $z$ -direction from $Z = 5$ to $10$ at: (a) $\zeta = 0$ and (b) $\zeta = 0.9$ ; the flow conditions are $Re_\delta = 800$ and $\lambda = 10$ for the time-averaged quantities of three intervals at: acceleration phase (AP), deceleration phase (DP) and late deceleration phase (LD). . . . .	98
4.16	The time-averaged axial vortices (rev/s) at the flow conditions of $Re_\delta = 800$ and $\lambda = 10$ for two intervals of the: (a) the acceleration phase (AP) and (b) the deceleration phase (DP). . . . .	99
4.17	The time-averaged axial velocities in the near-wall region nondimensionalized by the amplitude of the friction velocity for three intervals of the: acceleration phase (AP) (Green), deceleration phase (DP) (red), flow reversal phase (RV) (blue), $\bar{u}^+ = r_w^+$ (black dot-dashed curve) and log law (black dashed curve). . . . .	101
4.18	Axial velocity ( $u$ ) and gauge pressure ( $p$ ) for the flow conditions of $Re_\delta = 400$ and $\lambda = 10$ at: (a) $\zeta = 0.95$ and (b) $\zeta = 0.99$ . . . . .	102
5.1	Computational meshes including the frames of finite elements and Gauss-Lobatto-Legendre ( GLL) points: (a) outer mesh for $\Omega_o$ , (b) inner mesh for $\Omega_i$ , and (c) combined mesh for $\Omega_{o+i}$ . finite elements near the wall: (d) outer elements, (e) inner elements, and (f) combined elements. . . . .	107
5.2	The axial laminar velocity profile of the combined domain ( $\Omega_{o+i}$ ) at $Re_\delta = 100$ , $\lambda = 10$ , and $\tau/T = 1/16$ compared with the exact solution of <a href="#">Sexl (1930)</a> for the smooth pipe: (a) $\varepsilon_{sr} = 0$ and (b) $\varepsilon_{sr} = 0.0075$ and $\varepsilon_{sr} = 0.0125$ . . . . .	110
5.3	The temporal evolution of the axial velocity at three radial positions ( $\zeta = 0$ (blue), $0.9$ (green), and $0.99$ (red)). the transition induced by surface roughness only at different $Re_\delta$ 's ranging from $200$ to $235$ for $\lambda = 10$ and $\varepsilon_{sr} = 0.0075$ . . . . .	112

5.4	DNS comparisons for the smooth pipe: (a) instantaneous axial velocity of the present dns, (b) instantaneous axial velocity of <b>Feldmann &amp; Wagner (2012)</b> s' DNS, (c) phase-averaged velocity ( $\bar{u}^p$ ), and (d) RMS fluctuation velocity ( $u_{rms}^p$ ). the curves in (a) and (b) are at four radial positions: $\zeta = 0.02$ (blue), 0.74 (orange), 0.94 (green), and 0.98 (red). mean statistics are at the early deceleration (ED), late deceleration (LD), and flow reversal (RV) phases. . . . .	116
5.5	Contour plots of the axial velocity: (a) outer subdomain ( $\Omega_o$ ), (b) inner subdomain ( $\Omega_i$ ), and (c) combined domain ( $\Omega_{o+i}$ ) at $Re_\delta = 800$ , $\lambda = 10$ and $\tau/T = 0.32$ for $\epsilon_{sr} = 0.0075$ . . . . .	117
5.6	The time-varying axial velocities at $Re_\delta = 800$ and $\lambda = 10$ for two roughness heights: (a) $\epsilon_{sr} = 0$ and (b) $\epsilon_{sr} = 0.0075$ . . . . .	118
5.7	Root-mean-square (RMS) velocity with respect to the radial direction at $Re_\delta = 800$ and $\lambda = 10$ for $\epsilon_{sr} = 0.0075$ : (a) azimuth direction and (b) axial direction. . . . .	119
5.8	The time-dependent wall shear stresses, $\tau_w^*/\rho^*$ (cm/s) <sup>2</sup> , at $Re_\delta = 800$ and $\lambda = 10$ for $\epsilon_{sr} = 0$ (blue) and 0.0075 (red). . . . .	120
5.9	The friction coefficients at different $Re_\delta$ 's, $\lambda$ 's, and $\epsilon_{sr}$ 's, presenting a comparison between the present dns for the smooth and rough pipes and the results of <b>Jensen et al. (1989)</b> , <b>Lodahl et al. (1998)</b> , <b>Sleath (1987)</b> . . . . .	122
5.10	Cross-section contours of the instantaneous axial vorticity (rev/s) of the early acceleration (EA) and early deceleration (ED) phases at $Re_\delta = 800$ , $\lambda = 10$ , and $z = 5$ for the two roughness heights: (a) and (b) for $\epsilon_{sr} = 0$ , (c) and (d) for $\epsilon_{sr} = 0.0075$ . . . . .	124
1	Chebyshev derivatives of the time-dependent function $H$ appearing in Eqn. (1) along the radial direction: the exact solution obtained from $0.25(1 - \cos(2\pi\zeta))$ , solid curves, and the numerical representations, circles. . . . .	140
2	The instantaneous solution ( $H(\zeta, \tau)$ ) of Eqn. (1) utilized CPSM. . . . .	140
3	The instantaneous solution ( $H(\zeta, \tau)$ ) of Eqn. (1), circles, compared with the exact solution of $0.25e^{-3\tau}(1 - \cos(2\pi\zeta))$ , solid curves, at three different times. . . . .	141



# List of Tables

2.1	Approximate percent errors of $\omega$ obtained according to the mathematical relation in Eqn. (2.25) with various flow conditions. . . . .	46
3.1	Critical Reynolds numbers with respect to the Stokes number estimated by the two and three-dimensional simulations. Only the possible ranges of critical $Re_\delta$ are shown for the 3-D case at $\lambda = 10$ and 20. . . . .	59
4.1	The total number of grid points (GP) utilized for the pipe simulations at the flow conditions of $Re_\delta = 400$ and 800 with $\lambda = 10$ . . . . .	70
4.2	DNS-database of the flow conditions at $Re_\delta = 400$ and 800 for $\lambda=10$ . . . . .	74
4.3	3-D mesh (GP4 resolution) information in terms of wall units for the flow conditions of $Re_\delta = 400$ and 800 with $\lambda = 10$ . . . . .	77
4.4	Turbulence intensity ( $TI$ ) appearing in Eqn. (4.3) at four radial positions for two Reynolds numbers and $\lambda = 10$ . . . . .	91
5.1	DNS parameters used for a flow condition at $Re_\delta = 800$ and $\lambda = 10$ . . . . .	114
1	The friction Reynolds numbers, three-dimensional components of the velocity, gauge pressure fluctuations, Wall shear stresses, and Kolmogorov length scales at $Re_\delta = 800$ , $\lambda = 10$ , $0 < E_z < 25$ and $\tau/T = 3/8$ . . . . .	142
2	The friction Reynolds numbers, three-dimensional components of the velocity, gauge pressure fluctuations, Wall shear stresses, and Kolmogorov length scales at $Re_\delta = 800$ , $\lambda = 10$ , $25 < E_z < 50$ and $\tau/T = 3/8$ . . . . .	143
3	The friction Reynolds numbers, three-dimensional components of the velocity, gauge pressure fluctuations, Wall shear stresses, and Kolmogorov length scales at $Re_\delta = 800$ , $\lambda = 10$ , $50 < E_z < 75$ and $\tau/T = 3/8$ . . . . .	144

- 4 The friction Reynolds numbers, three-dimensional components of the velocity, gauge pressure fluctuations, Wall shear stresses, and Kolmogorov length scales at  $Re_\delta = 800$ ,  $\lambda = 10$ ,  $75 < E_z < 100$  and  $\tau/T = 3/8$ . . . . . 145

# Nomenclature

## Symbols

$\bar{u}$	Cycle-averaged velocity normalized by $\hat{u}^*$
$\mathbf{A}$	Time-dependent matrix used in Eqn. (2.13)
$\mathbf{B}$	Constant matrix used in Eqn. (2.13)
$\mathbf{I}$	identity matrix
$\mathbf{X}$	Fundamental solution matrix
$\tilde{A}$	Dimensionless pressure gradient amplitude
$\tilde{F}$	Dimensionless driving force in the axial direction
$c$	Disturbance wave velocity, $\omega/k$
$E$	Number of elements
$f$	Time-dependent function
$k$	Dimensionless wavenumber of disturbance scaled by $1/\delta$
$L$	Linear operator
$m$	Parameter used in Eqn. (2.25)
$N$	Polynomial degree
$n$	Integer
$r$	Radial coordinate nondimensionalized by $\delta^*$
$s$	dummy variable
$T$	Dimensionless period of flow oscillation
$U$	Axial laminar velocity normalized by $\hat{u}^*$
$u$	Instantaneous axial velocity normalized by $\hat{u}^*$
$x$	Axial coordinate of the axisymmetric domain nondimensionalized by $\delta^*$
$Z$	Dimensionless axial coordinate defined as $z/\lambda = z^*/R^*$
$z$	Axial coordinate nondimensionalized by $\delta^*$
$\mathbf{i}$	Unit imaginary number, $\sqrt{-1}$

## Greek Letters

$\alpha$	Time-dependent function used in Eqn. (2.15)
$\beta$	Time-dependent function used in Eqn. (2.15)
$\eta$	Disturbance amplitude function
$\gamma$	Floquet multiplier
$\iota$	Roughness parameter normalized by $R^*$
$\kappa$	Dimensionless wave number
$\Omega$	Angular frequency nondimensionalized by $\hat{u}^*/R^*$
$\phi$	eigenfunction in Eqn. (2.18), nondimensionalized by $\hat{u}^*.(R^*)^2$
$\Psi$	Stream function of the laminar base flow nondimensionalized by $\hat{u}^*.( \delta^* )^2$
$\psi$	Stream function of small disturbance field, nondimensionalized by $\hat{u}^*.( \delta^* )^2$
$\sigma$	Floquet exponent
$\tau$	Time nondimensionalized by $R^*/\hat{u}^*$
$\theta$	Azimuth angle in the cylindrical coordinates
$\varepsilon$	Dimensionless expansion parameter
$\varepsilon_{sr}$	Dimensionless roughness amplitude defined as $\varepsilon_{sr}^*/R^*$
$\xi$	Real scalar function used in Eqn. (2.14)
$\zeta$	Dimensionless radial distance defined as $r/\lambda = r^*/R^*$
$O$	Order of magnitude

## Superscripts

$\bar{u}^p$	Phase-averaged velocity normalized by $\hat{u}^*$
$\delta^*$	Stokes thickness ( $\sqrt{2\nu^*/\Omega^*}$ )
$\hat{u}_\tau^*$	Dimensional friction velocity amplitude ( $\sqrt{ \hat{\tau}_w^* /\rho^*}$ )
$\hat{\tau}_w^*$	Dimensional wall shear stress amplitude
$\hat{u}^*$	Dimensional axial velocity amplitude at $r = 0$
$\nu^*$	Dimensional kinematic viscosity
$\rho^*$	Dimensional density
$\tau_w^*$	Dimensional wall shear stress
$v^*$	Dimensional radial velocity
$\Lambda^*$	Kolmogorov length scale
$D^*$	Dimensional pipe diameter
$L^*$	Dimensional pipe length
$p^*$	Dimensional static pressure

$r_w^+$	Dimensionless distance from the wall
$R^*$	Dimensional pipe radius
$t^*$	Dimensional time
$u_{\text{rms}}^p$	Root-mean-square (RMS) velocity, associated with the phase average, normalized by $\hat{u}^*$

### Subscripts

$\Omega_i$	Inner subdomain
$\Omega_{0+i}$	Combined domain
$\Omega_o$	Outer subdomain
$C_f$	Friction coefficient
$J_0$	Bessel function of the first kind
$t_1$	Slow time scale
$u_{\text{rms}}$	Root-mean-square (RMS) velocity normalized by $\hat{u}^*$

### Dimensionless Numbers

$\lambda$	Dimensionless pipe radius, $R^*/\delta^*$ (Stokes number)
$Re_\delta$	Reynolds number based on $\hat{u}^*$ and $\delta^*$

### Acronyms

<b>DNS</b>	Direct numerical simulation
<b>GLL</b>	Gauss-Lobatto-Legendre points
<b>TKE</b>	Turbulence kinetic energy
<b>WSS</b>	Wall shear stress
$TI$	Turbulence intensity defined with respect to the laminar velocity, $U$
<b>SEM</b>	Spectral element method

# Chapter 1

## Introduction

When the properties of fluid flow such as the velocity and pressure change with time, the flow is simply called unsteady. Pulsating and oscillating flows are the common terms of unsteady/time-dependent flows. Examples are found in many engineering disciplines such as the oil pressure supply systems, reciprocating engines, heat exchangers, and biological systems etc. Basically, the second type (oscillating flows) with zero mean velocity is a sub-branch of the pulsating flows, where the oscillations are superimposed on the base flow. Although the two types of flow have been studied by many investigators with different tools, limited analytical and numerical solutions of the continuity, momentum, and energy equations are found due to the complexity of these flows. The problems of analyzing the flow become even more complicated if the fluid is non-Newtonian.

The analytical solution for the governing equations of an incompressible Newtonian fluid flow subjected to the long-time oscillation of time-dependent pressure gradient,  $\partial p^*/\partial z^* = A^* e^{\Omega^* t^*}$ , was obtained by [Sexl \(1930\)](#). Following a similar procedure of analysis, [Womersley \(1955\)](#) used the same flow characteristics of [Sexl \(1930\)](#) in a biological perspective to find a general formulation for the velocity. He represented the phase lag between the pressure and velocity to that between the voltage and current in a conductor carrying an alternating current, so that the relation can be expressed in one single non-dimensional

parameter called Womersley number, or  $Wo = R^* \sqrt{\Omega^* / \nu^*}$ . The flow patterns of the laminar pulsating flow are classified into quasi-steady, intermediate, and inertia dominant parts by [Ohmi \*et al.\* \(1981\)](#). For the same flow, an experimental representation of the laminar velocity profiles was conducted by [Harris \*et al.\* \(1969\)](#), and the results showed that the peak of the flow becomes closer to the wall when the frequency of base flow increases.

Further measurements for the velocity profiles at different phases of oscillation cycle are conducted by [Ohmi \*et al.\* \(1982\)](#) experimentally for a wide range of oscillation frequencies. They confirmed that the turbulence in oscillating flows is comparable to that of the steady flows in the sense of Blasius 1/7 law, but the relaminarized velocity in the acceleration phase is not like that of the theoretical long-time oscillation. However, the study of [Iguchi \*et al.\* \(1987\)](#) showed that the periodic turbulence slugs do not resemble those of the steady flows, albeit their velocity profiles at low oscillation frequencies outside the slug were approximated to those of analytical solutions of the steady flows. The coherent structures of turbulent flow were also captured by a camera installed on a gearing system of the scotch yoke of [Fishler & Brodkey \(1991\)](#)'s experiment. They noticed that most of the turbulence activity appears in the deceleration phase, and its intensity increases with the Reynolds number.

In the literature, the determination of the critical Reynolds number for this type of flow is questionable. The study of [Çarpınlioğlu & Gündoğdu \(2001\)](#) about the transition to turbulence in the oscillating flows categorized the process into four stages: disturbed laminar flow, finite-amplitude perturbation, first appearing of turbulence bursts, and persisting turbulence bursts. Several strategies were employed to detect the onset of transition starting from the visual observations (see, for example, [Sergeev \(1966\)](#)), electronic detections of a hot wire anemometer (see, for example, [Hino \*et al.\* \(1976\)](#)), and possible developments of vorticity (see, for example, [Merkli & Thomann \(1975\)](#)). Some related the appearance of turbulence bursts to the variations of wall shear stress with time so that the

critical Reynolds number can be evaluated (see, for example, [Lodahl \*et al.\* \(1998\)](#)). Since the generation of turbulence for the oscillating and steady flows is defined similarly by the well-known 1/7 power law, [Ohmi & Iguchi \(1982\)](#) found their critical Reynolds numbers at the stage where the origin of the turbulence was built up in the flow field, which is the same way usually used for the steady flows.

Regarding the stability problems, the quasi-steady assumption has been performed in a few different forms to study the development of disturbance. [Obremski & Morkovin \(1969\)](#) used the quasi-steady method to investigate the stability-transition process of unsteady periodic boundary layer on a flat plate. Their criterion of instability depends on the amplification of disturbance creating wave packets downstream. They found that the theoretical results are consistent with some experimental observations, and they claimed that their quasi-steady formulation needs more verifications to be considered as a working tool. Another application of the quasi-steady method is found in the study of [Mackley & Stonestreet \(1995\)](#), that introduced the flow oscillation in the tube side to enhance the heat transfer for a shell-and-tube heat exchanger. In their study, the principle of frozen profiles was assumed for the pressure, not for the velocity, and the power density was plotted at different amplitudes of oscillation revealing that the quasi-steady prediction is in agreement with the experimental data at large amplitudes of oscillation rather than other cases.

The order-of-magnitude analysis was utilized in the quasi-steady method of [Jan \*et al.\* \(1989\)](#) in addition to the experimental data for a single bifurcation of lung-like geometry to identify three flow regimes according to the influence of: unsteadiness, viscous, and convective acceleration. The new assumption of [Vilaina \*et al.\* \(1989\)](#), which is essentially based on the quasi-steady boundary layer theory, successfully described the flow through the glottis, and the results were compared with measured data and showed a good agreement except when the unsteady or viscous terms become predominant. A similar technique of dealing with the base flow and its disturbances was carried out by [Che & Jin](#)



(2017) on the stability analysis of oscillatory Taylor-Culick flow. The equations of linearized motion for a flow combining the steady and periodic acoustic parts were solved by the multiple time scale assumption, and the results showed that the maximum growth rates are related to the frequency and amplitude of the acoustic oscillation.

The application of the linear stability analysis differs between the steady flows and unsteady flows. For example, Davis (1976) reported that the stability results of steady flows may not be suitable for unsteady flows unless a precise scale representation is fulfilled. A similar conclusion was reached in the theoretical study of Tozzi & von Kerczek (1986) about the linear stability of pulsating flows, and it was found that the flow becomes slightly more stable to the axisymmetric disturbances if low-frequency oscillations are imposed to the mean velocity. Although Young & Tsai (1973) emphasized that many of the experimental results of the steady flow are valid for the oscillating flows with some differences, their measurements revealed that the stability of oscillating flows is affected by the amount of area constriction within the fluid flow. The unsteady flow was more stable than the current flow at a mild area reduction, but the opposite scenario observed when the area was extremely narrow.

A transition in the pipe flow driven by a time-dependent pressure gradient has attracted many investigators for several decades. For example, Cooper *et al.* (1993) compiled data collection of experimental studies in the period between 1954 to 1989, trying to determine the onset of transition. Since the critical Reynolds numbers ( $Re_\delta$ ), based on the axial velocity amplitude and Stokes thickness, depend on the flow characteristics including the oscillation frequency, their reported levels were between 113 and 566 approximately for high Stokes numbers, the ratio between the radius of the pipe to the Stokes thickness. It is noticed that the compiled numbers by Cooper *et al.* (1993) differ not only from one experiment to another, but also between the experiments and theories. Some possible reasons of these discrepancies were mentioned by Hino *et al.* (1976) who ultimately stated

the following sentence: “there is no reason to believe that the experimental and the theoretical results should be precisely compatible”.

Oscillating flows may reach similar behaviors at high-frequency oscillations in the near-wall region of the three main geometries: circular pipe, planer channel, and flat plate, revealing that the frequency of base flow has the same role within the Stokes layer regarding the wall-bounded flows (Lodahl *et al.* (1998)). On the other hand, the amplitude of oscillation is not only an important factor for the shape of the flow in the different geometries, but also affects the values of the critical conditions. The experimental study of Miller & Fejer (1964) conducted in a closed-circuit wind tunnel showed that the oscillating boundary layer is very sensitive to the amplitude of oscillation at the transitional stage, and the spatial locations and time periods of turbulent bursts are associated entirely with the fluctuations of the free stream velocity.

At relatively high Reynolds numbers, the flow experiences highly disturbed waviness or transient turbulence which could provide some advantages of being created in the flow field. For instance, the importance of transition to turbulence can be found in the mechanism of heat transfer, where the heat transfer coefficient of oscillatory flows increases with the turbulence. Similarly, the quality of fuel-air mixture is enhanced with turbulence so that a high speed of oscillating piston is required. In contrast, transitional-turbulent blood flow in arteries or in some stenosed areas is the most frequent cause of the cardiovascular diseases. However, for other purposes, the turbulent flow can be relaminarized when the current flow is combined with oscillating waves, when they are dominated and in the laminar regime (see, for example, Lodahl *et al.* (1998)).

The periodic turbulence and relaminarization within one oscillation cycle is a common phenomenon observed in many experiments regarding this flow (see, for example, Hino *et al.* (1976), Iguchi & Ohmi (1982), Kurzweg *et al.* (1989), Merkli & Thomann (1975), Zhao & Cheng (1996)). The majority of investigators agrees that the repeated inertial

forces are behind such behavior, mostly reported at the intermittent turbulent flow conditions. However, the nature of turbulence bursts in the oscillating flows is still unclear, although some including [Wu \*et al.\* \(1993\)](#) emphasized that the nonlinear interactions induce the evolution of disturbances to cause an explosive growth leading to these sudden bursts. In order to show an example for this type of the flow behavior at turbulence conditions, the magnitudes of axial velocity spatially probed at different positions by [Hino \*et al.\* \(1976\)](#) are shown below in Fig. 1.1. The flow is obviously experiencing turbulence and then relaminarizes within the oscillation cycle of length  $2\pi$ , or  $\Omega T$  with a non-dimensionalized angular frequency  $\Omega$  and a time period  $T$ . Note that  $\zeta$  is a non-dimensional coordinate in the radial direction.

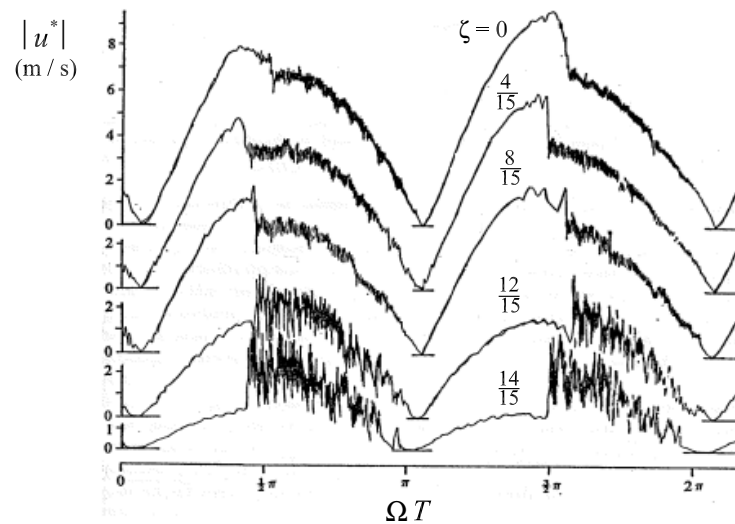


**Figure 1.1:** Axial velocity magnitudes ( $|u^*|$ ) at five different radial positions ( $\zeta$ ), taken from [Hino \*et al.\* \(1976\)](#)'s experiment for one oscillation cycle.

[Hino \*et al.\* \(1976\)](#) identified two possible factors altering the stability limits of the purely oscillating flow: the representation of the base flow profile and the flow sensitivity to finite amplitude disturbances. They reported that in a range from 70 to 550 of Reynolds numbers, the flow is disturbed, whereas the turbulence effects start to strengthen at  $Re_\delta = 550$ . Although [Ramaprian & Muller \(1980\)](#) could not find a critical Reynolds number,

they stated that the disturbances can grow rapidly above  $Re_\delta = 370$  as their experiment revealed. Luo & Wu (2010) concluded that the nonlinearity of the oscillating channel flow is very responsive to the surface roughness, for example  $0.1 \mu\text{m}$  roughness height can trigger the flow at  $Re_\delta \geq 300$ . The finding of Collins (1963), where the critical values of  $Re_\delta$  changed considerably when the a non-smooth plate was used, was also reported in Luo & Wu (2010)'s study.

Therefore, in spite of different strategies that have been used to study the behavior of purely oscillating pipe flow (with zero-mean velocity) over many years, a robust transition criterion for this well-known flow is still unclear. The objectives of the proposed research are to find the critical Reynolds numbers at which the flow undergoes periodic disturbances or turbulence for a wide range of parameters and to provide a detailed description of the transition mechanism and the turbulence characteristics. In this regard, the thesis will be divided into two main sections: the theoretical and computational study.

In Chapter Two, the major methods in the framework of the linear stability analysis, which are the Floquet theory and the multiple scales approach, were compared with the quasi-steady method of the current study. The solution of a model equation proposed for the linear stability equation was calculated and plotted for several oscillation cycles to explore the main differences among those three theories. The assumption of the quasi-steady method was tested to predict the transient instability for the hydrodynamic equation. The conditions at which the quasi-steady theory is valid were determined with a new mathematical basis, which can be used to produce the approximate accuracy of the theoretical results at any flow condition.

In Chapter Three, critical Reynolds numbers at six different Stokes numbers have been found by performing direct numerical simulations (DNS) using Nek5000 solver (based on the spectral-element method) for two and three-dimensional flows. The two-dimensional perturbations were introduced to the axisymmetric flow domain to find the minimum crit-

ical Reynolds numbers in line with the Squire's theorem of the stability theory, although the disturbances may be asymmetric and three-dimensional naturally in the smooth pipe. That was also confirmed by simulating 3-D flows at a few flow conditions and predicting the critical Reynolds numbers within small bounds. To give a comprehensive background to the onset of transition, experiments and theories were compiled and compared with the present DNS results showing a qualitative agreement.

Regarding the accuracy of the quasi-steady method, DNS results were used to validate the assumptions and the relation created to predict the transient flow instability within a cycle. In addition, critical Reynolds numbers for a planar channel flow were determined in the two-dimensional domains at two Stokes numbers. A comparison was made against the corresponding values of the pipe flow to highlight some remarks. The stability was examined at relatively two high-frequency oscillations, and the results showed that the Stokes number must be higher than 30 to consider that the predictions attributed to the two flow geometries will not be affected by the surface shape.

In Chapter Four, additional numerical simulations were performed for turbulent flows. At comparatively two high Reynolds numbers, the flows were studied to demonstrate the differences and similarities between different quantities such as the axial velocity around the time history of two consecutive cycles. Although most of the turbulence happens during the deceleration phase, the grid resolution was increased for the whole oscillation cycle to cover the smallest length scales of motion, which were calculated explicitly from the DNS data. The existence of turbulence was also discovered in the profiles of the wall shear stress, which were evaluated for the two flow conditions during the two cycles. Other statistical quantities were produced such as the root-mean-square velocity fluctuations, spatial autocorrelation functions, and one-dimensional energy spectra.

In Chapter Five, instability initiated by wall imperfections is one of the fundamental issues that most oscillating flows deal with. In particular, the wall irregularities augment

disturbances to develop during parts of the oscillation cycle when the deceleration phases begin. Since the overshoot velocity shifts toward the wall, especially at higher oscillation frequencies, the surface shape is a significant factor of accelerating or even delaying the transition and then turbulence. Regarding the computational approaches, unstructured grids are not always a good representation for the surface roughness and thus they need to be reshaped to capture the most significant features of the oscillatory flow. Herein, over-set mesh or known as chimera was implemented to model the wall roughness in the axial direction and to reduce the computational cost required for the near-wall zone. This methodology divides the whole domain into two partitions in which grids may be easily constructed with maintaining their structured shapes. Accordingly, smoothly corrugated roughness elements in the longitudinal direction were mounted at the outer domain and combined with the inner one with interface boundaries. Examining this new approach in details at three flow regimes and how the transition of the oscillatory flow can be caused by the wall influence only have been investigated. In addition, friction losses, when turbulence bursts clearly appear, were found and compared with multiple cases of the existing experiments for smooth and rough walls, and the results showed a good agreement.

# Chapter 2

## Linear Stability Theories

### 2.1 Overview

Introducing two-dimensional perturbations with small amplitude to unsteady flows such as the oscillating flows, where the pressure gradient is time-periodic, can lead to a linear instability at relatively low Reynolds numbers. This case is in contrast to the steady Poiseuille flow with a constant pressure gradient, where the flow is found to be stable to all axisymmetric infinitesimal disturbances in a wide range of Reynolds numbers as well as wavenumbers (see, for example, [Salwen & Grosch \(1972\)](#)). However, some investigators noticed instabilities in the experiments of Poiseuille flow conducted at certain conditions, and some of them attributed those experimental observations of unstable modes to either finite-amplitude effects or a very slow rotation of the inlet flow (see, for example, [Drazin & Reid \(1981\)](#)).

In the literature, there are two major methods that can solve the hydrodynamic stability equation for oscillating flows: the Floquet theory and the multiple scales analysis. First, the former is known as a rigorous approach, and it has been applied successfully in many

problems involving stability. Nevertheless, the onset of transition as observed in experiments was not achieved by some researchers who applied the formal Floquet method to the Stokes layer problem (see, for example, Hall (1978), von Kerczek & Davis (1974)). Second, the validity of the multiple scales approach in the stability problems was first studied by Benney & Rosenblat (1964), and some who utilized this method for oscillating flows were able to predict the transient growth rate inducing instability during an oscillation cycle (see, for example, Cowley (1987), Monkewitz & Bunster (1987)). For a few different unsteady planar flows (see, for example, Lee (2002), Lee & Beddini (1999)), a special version of multiple scales approach to analyze the parametric flow stability was also successful in showing the mechanism of transient disturbance growth.

The failure of the Floquet method conducted on a modulated planar channel flow by Singer *et al.* (1989) was reported via comparing the theoretical results with those of direct numerical simulations. The investigation of Yang & Yih (1977) did not show any instability indicated by the Floquet exponents when two-dimensional disturbances were introduced to the same flow investigated herein. In both axisymmetric and planar geometries, the Floquet analysis of Blennerhassett & Bassom (2006) showed a linear instability at high Reynolds numbers above 1000, revealing a big discrepancy against those of experiments. At their flow conditions, where the analysis of Floquet theory led to stability, turbulence was reported in the direct numerical simulations they cited, although the numerical data were not directly related to the theoretical results. Therefore, it is clear that the Floquet method is not capable of producing an accurate flow transition for this kind of flow under the typical circumstances described in many studies (see, for example, Singer *et al.* (1989)).

In this chapter, a quasi-steady formulation is applied to the linear stability equation of oscillating pipe flow by imposing two-dimensional axisymmetric disturbances. The basic idea of this method is that the temporal changes of disturbance occur much faster than



those of the base velocity so that the frozen profiles can be assumed. The Floquet analysis and the multiple scales method are also compared to discuss the differences and similarities among those two major theories and the quasi-steady assumption. Although different attempts employing a similar theory with some modifications are found in other studies, the accuracy of their results demands that the Reynolds number should be very large, but how large it should be has not been determined in the literature. Therefore, depending on the order-of-magnitude analysis, a simple formula is developed herein to evaluate the approximate accuracy of the quasi-steady method at various flow conditions.

## 2.2 Analysis

In this chapter, an axisymmetric domain is considered with the  $x^*$  and  $r^*$  coordinates in the axial and radial directions, respectively. Two components of velocity corresponding to each axis are denoted by  $u^*$  and  $v^*$  for the current analysis. The governing equations according to the mass and momentum conservation laws for an incompressible flow with constant transport properties are written as

$$\frac{1}{r^*} \frac{\partial}{\partial r^*} (r^* v^*) + \frac{\partial u^*}{\partial x^*} = 0, \quad (2.1)$$

$$\frac{\partial u^*}{\partial t^*} + v^* \frac{\partial u^*}{\partial r^*} + u^* \frac{\partial u^*}{\partial x^*} = -\frac{1}{\rho^*} \frac{\partial p^*}{\partial x^*} + v^* \left\{ \frac{1}{r^*} \frac{\partial}{\partial r^*} \left( r^* \frac{\partial u^*}{\partial r^*} \right) + \frac{\partial^2 u^*}{\partial (x^*)^2} \right\}, \quad (2.2)$$

$$\frac{\partial v^*}{\partial t^*} + v^* \frac{\partial v^*}{\partial r^*} + u^* \frac{\partial v^*}{\partial x^*} = -\frac{1}{\rho^*} \frac{\partial p^*}{\partial r^*} + v^* \left\{ \frac{1}{r^*} \frac{\partial}{\partial r^*} \left( r^* \frac{\partial v^*}{\partial r^*} \right) + \frac{\partial^2 v^*}{\partial (x^*)^2} - \frac{v^*}{(r^*)^2} \right\}, \quad (2.3)$$

where  $p^*$ ,  $\rho^*$ , and  $\nu^*$  are the dimensional pressure, density, and kinematic viscosity. The two momentum equations can be combined if differentiations are made to Eqn. (2.2) and Eqn. (2.3) with respect to  $r^*$  and  $x^*$ , respectively, as follows:

$$\begin{aligned} \frac{\partial^2 u^*}{\partial r^* \partial t^*} + \nu^* \frac{\partial^2 u^*}{\partial (r^*)^2} + \frac{\partial u^*}{\partial r^*} \frac{\partial v^*}{\partial r^*} + u^* \frac{\partial^2 u^*}{\partial r^* \partial x^*} + \frac{\partial u^*}{\partial x^*} \frac{\partial u^*}{\partial r^*} = -\frac{1}{\rho^*} \frac{\partial^2 p^*}{\partial r^* \partial x^*} \\ + \nu^* \left\{ \frac{\partial}{\partial r^*} \left[ \frac{1}{r^*} \frac{\partial}{\partial r^*} \left( r^* \frac{\partial u^*}{\partial r^*} \right) \right] + \frac{\partial^3 u^*}{\partial r^* \partial (x^*)^2} \right\}, \end{aligned} \quad (2.4)$$

$$\begin{aligned} \frac{\partial^2 v^*}{\partial x^* \partial t^*} + \nu^* \frac{\partial^2 v^*}{\partial (x^*)^2} + \frac{\partial v^*}{\partial x^*} \frac{\partial u^*}{\partial x^*} + \nu^* \frac{\partial^2 v^*}{\partial x^* \partial r^*} + \frac{\partial v^*}{\partial x^*} \frac{\partial v^*}{\partial r^*} = -\frac{1}{\rho^*} \frac{\partial^2 p^*}{\partial x^* \partial r^*} \\ + \nu^* \left\{ \frac{1}{r^*} \frac{\partial}{\partial r^*} \left[ r^* \frac{\partial}{\partial r^*} \left( \frac{\partial v^*}{\partial x^*} \right) \right] - \frac{1}{(r^*)^2} \frac{\partial v^*}{\partial x^*} + \frac{\partial^3 v^*}{\partial (x^*)^3} \right\}. \end{aligned} \quad (2.5)$$

The pressure term is eliminated after subtracting Eqn. (2.5) from Eqn. (2.4), thereby

$$\begin{aligned} \frac{\partial}{\partial t^*} \left( \frac{\partial u^*}{\partial r^*} - \frac{\partial v^*}{\partial x^*} \right) + \nu^* \frac{\partial}{\partial r^*} \left( \frac{\partial u^*}{\partial r^*} - \frac{\partial v^*}{\partial x^*} \right) + u^* \frac{\partial}{\partial x^*} \left( \frac{\partial u^*}{\partial r^*} - \frac{\partial v^*}{\partial x^*} \right) - \frac{1}{r^*} \nu^* \left( \frac{\partial u^*}{\partial r^*} - \frac{\partial v^*}{\partial x^*} \right) \\ = \nu^* \left\{ \frac{\partial}{\partial r^*} \left[ \frac{1}{r^*} \frac{\partial}{\partial r^*} \left( r^* \frac{\partial u^*}{\partial r^*} \right) \right] - \frac{1}{r^*} \frac{\partial}{\partial r^*} \left[ r^* \frac{\partial}{\partial r^*} \left( \frac{\partial v^*}{\partial x^*} \right) \right] + \frac{1}{(r^*)^2} \frac{\partial v^*}{\partial x^*} + \frac{\partial^2}{\partial (x^*)^2} \left( \frac{\partial u^*}{\partial r^*} - \frac{\partial v^*}{\partial x^*} \right) \right\}. \end{aligned} \quad (2.6)$$

The concept of stream function ( $\tilde{\psi}^*$ ) satisfying the continuity Eqn. (2.1) can be applied, and then the two velocity components are

$$u^* \equiv \frac{1}{r^*} \frac{\partial \tilde{\psi}^*}{\partial r^*} \quad v^* \equiv -\frac{1}{r^*} \frac{\partial \tilde{\psi}^*}{\partial x^*}.$$

Thus, Eqn. (2.6) can be simplified in terms of  $\tilde{\psi}^*$  by incorporating the following component of the vorticity:

$$\frac{\partial u^*}{\partial r^*} - \frac{\partial v^*}{\partial x^*} = \frac{1}{r^*} \Delta^* \tilde{\psi}^*,$$

where the operator  $\Delta^*$  written as

$$\Delta^* \equiv \frac{\partial^2}{\partial (r^*)^2} - \frac{1}{r^*} \frac{\partial}{\partial r^*} + \frac{\partial^2}{\partial (x^*)^2},$$

is the same as the Laplace operator except the negative sign in the second term. Substituting the above velocities and their derivatives into Eqn. (2.6) yields the following equation written in the cylindrical coordinate system for a non-dimensional stream function,  $\tilde{\psi}$ :

$$\frac{\partial}{\partial t} (\Delta \tilde{\psi}) - \frac{1}{r} \frac{\partial \tilde{\psi}}{\partial x} \frac{\partial}{\partial r} (\Delta \tilde{\psi}) + \frac{1}{r} \frac{\partial \tilde{\psi}}{\partial r} \frac{\partial}{\partial x} (\Delta \tilde{\psi}) + \frac{2}{r^2} \frac{\partial \tilde{\psi}}{\partial x} (\Delta \tilde{\psi}) = \frac{1}{Re_\delta} \Delta (\Delta \tilde{\psi}), \quad (2.7)$$

where the velocity, length, and time are non-dimensionalized by the velocity amplitude at the axis of symmetry,  $\hat{u}^*$ , Stokes thickness,  $\delta^*$ , and  $\delta^*/\hat{u}^*$ , respectively. Henceforth, the parameter  $Re_\delta$  is the Reynolds number defined as

$$Re_\delta = \frac{\sqrt{2} \hat{u}^*}{\sqrt{\nu^* \Omega^*}},$$

where  $\Omega^*$  is the angular frequency of oscillation for the base flow, and the Stokes thickness is

$$\delta^* = \sqrt{\frac{2\nu^*}{\Omega^*}}.$$

To obtain a fully developed laminar flow, a low-amplitude sinusoidal pressure gradient is imposed in the axial direction of a circular pipe, and accordingly, the solution derived by [Sexl \(1930\)](#) will be used for this study. The base velocity,  $U(t, r)$ , in the  $x$ -direction is a  $2\pi$ -periodic function, whereas the radial component of the base velocity is zero. The stream function is decomposed as follows:

$$\tilde{\psi}(t, r, x) = \Psi(t, r) + \psi(t, r, x), \quad (2.8)$$

where  $\Psi$  is the stream function of the unsteady laminar base flow, and  $\psi$  is that of the axisymmetric disturbances. Equation. (2.8) can be substituted into Eqn. (2.7), and the linearized stream function equation for disturbance is obtained by eliminating the equation of  $\Psi$  from the final result, neglecting the nonlinear terms, and rearranging the equation to

$$\frac{\partial}{\partial t}(\Delta\psi) = -\frac{1}{r} \frac{\partial\Psi}{\partial r} \frac{\partial}{\partial x}(\Delta\psi) + \left( \frac{1}{r} \frac{\partial}{\partial r}(\Delta\Psi) - \frac{2}{r^2} \Delta\Psi \right) \frac{\partial\psi}{\partial x} + \frac{1}{Re_\delta} \Delta(\Delta\psi), \quad (2.9)$$

where  $\Delta\Psi \equiv \frac{\partial^2\Psi}{\partial r^2} - \frac{1}{r} \frac{\partial\Psi}{\partial r}$ . The axial base velocity and its first and second derivatives based on the definition of the stream function are

$$U \equiv \frac{1}{r} \frac{\partial\Psi}{\partial r}, \quad \frac{\partial U}{\partial r} = \frac{1}{r} \Delta\Psi, \quad \frac{\partial^2 U}{\partial r^2} = \frac{1}{r} \left[ \frac{\partial}{\partial r}(\Delta\Psi) - \frac{1}{r} \Delta\Psi \right],$$

respectively, being utilized to convert Eqn. (2.9) to

$$\frac{\partial}{\partial t}(\Delta\psi) = -U \frac{\partial}{\partial x}(\Delta\psi) - \left( \frac{1}{r} \frac{\partial U}{\partial r} - \frac{\partial^2 U}{\partial r^2} \right) \frac{\partial\psi}{\partial x} + \frac{1}{Re_\delta} \Delta(\Delta\psi). \quad (2.10)$$

The solution of Eqn. (2.10) is pursued by introducing the following assumption for the

disturbance stream function:

$$\psi(t, r, x) = \eta(t, r) e^{ikx}, \quad (2.11)$$

where the dimensionless parameter,  $k$ , represents the axial wave number of disturbance nondimensionalized by  $1/\delta^*$ , and  $i$  is the unit imaginary number. Note that the type of disturbance is a traveling wave. After substituting Eqn. (2.11) into Eqn. (2.10), the latter can be modified to

$$\frac{\partial}{\partial t} L(\eta) = -ik \left\{ U L(\eta) + \left( \frac{1}{r} \frac{\partial U}{\partial r} - \frac{\partial^2 U}{\partial r^2} \right) \eta \right\} + \frac{1}{Re_\delta} L^2(\eta), \quad (2.12)$$

where the linear operator,  $L$ , is defined as

$$L \equiv \frac{\partial^2}{\partial r^2} - \frac{1}{r} \frac{\partial}{\partial r} - k^2.$$

The boundary conditions are applied to the wall with a no-slip condition and to the axis of symmetry with a bounded velocity at  $r = 0$ , i.e.,

$$\eta = 0 = \frac{\partial \eta}{\partial r},$$

at the two locations. For the spatial discretization of the partial differential Eqn. (2.12),  $N \times N$  derivative matrices mapping on the collocation points along the  $r$ -direction are implemented. This spatial representation allows the solution to be a vector including the values of  $\eta$  at each grid point. The higher-order derivative matrices in Eqn. (2.12) can be constructed from the matrix multiplication of lower-order ones. Consequently, the partial

differential Eqn. (2.12) may be converted into a first-order ordinary differential equation written as

$$\mathbf{F} \frac{d}{dt} \boldsymbol{\eta}(t) = \{\mathbf{A}(t) + \mathbf{B}\} \boldsymbol{\eta}(t), \quad (2.13)$$

where  $\boldsymbol{\eta}(t)$  is an unknown  $N \times 1$  column matrix, and  $\mathbf{F}$ ,  $\mathbf{A}(t)$  and  $\mathbf{B}$  are square matrices of size  $N \times N$ . The matrices of the operator  $L$  on the left side of Eqn. (2.12) are embedded in the coefficient  $\mathbf{F}$ . The function  $\mathbf{A}(t)$  is a time-dependent matrix representing the terms of time-dependent base flow velocity, and the derivative matrices from  $L^2$  and  $Re_\delta$  are included in the term  $\mathbf{B}$ . Note that both  $\mathbf{F}$  and  $\mathbf{B}$  matrices are time-independent, whereas  $\mathbf{A}(t)$  is a time-periodic matrix.

Applications of the Floquet theory (see, for example, Hall (1978), von Kerczek & Davis (1974), Yang & Yih (1977)) and the method of multiple scales (see, for example, Cowley (1987), Lee (2002), Monkewitz & Bunster (1987)), formulated as that shown in Eqn. (2.13), are found in the literature regarding the linear stability problem of unsteady base flows. In this study, these two methods are revisited analytically and compared with the assumption of quasi-steady method. The differences among the Floquet theory, the multiple scales approach and the present method can be investigated via introducing a first-order ordinary differential equation for a real scalar function,  $\xi(t)$ , similar to Eqn. (2.13) obtained from Eqn. (2.12) as follows:

$$\frac{d}{dt} \xi(t) = \{a(t) + b\} \xi(t), \quad (2.14)$$

where  $a(t) + b$  is a  $T$ -periodic function since  $a(t)$  is a real  $T$ -periodic term and  $b$  is a real constant. Note that the above problem can be extended simply with complex  $a(t) + b$  and  $\xi(t)$ .

### 2.2.1 Floquet method for the model equation and its extension

The Floquet theory is a well-known method for many dynamic systems seeking a class of solution to periodic linear differential equations. Herein, two time-dependent functions,  $\alpha(t)$  and  $\beta(t)$ , are introduced to solve the differential Eqn. (2.14) (see, for example, [Iooss & Joseph \(1990\)](#)) so that the exact solution is

$$\xi(t) = \xi(0) \alpha(t) = \xi(0) \beta(t) e^{\sigma t}, \quad (2.15)$$

where  $\sigma$  is the Floquet exponent by which the stability of flow can be examined. If the solution in Eqn. (2.15) is substituted into the differential Eqn. (2.14), and then the result is integrated by imposing the natural initial condition,  $\alpha(0) = 1 = \beta(0)$ , the function  $\beta(t)$  is

$$\beta(t) = \exp \left[ \int_0^t \{a(s) + b - \sigma\} ds \right],$$

with a dummy variable,  $s$ , assuming that  $\xi(t)/\xi(0)$  and accordingly  $\alpha(t)$  and  $\beta(t)$  are positive. Thus, the solution for Eqn. (2.14) can be obtained from

$$\xi(t) = \xi(0) \alpha(t) = \xi(0) \exp \left[ \int_0^t \{a(s) + b\} ds \right].$$

since the function  $\beta(t)$  is a  $T$ -periodic function owing to  $\alpha(t)$ , which is the solution of the differential equation with  $\xi(0) = 1$ , i.e.,  $\alpha(T) = \exp[\sigma T]$ , the Floquet exponent can be found explicitly from

$$\sigma = \frac{1}{T} \ln[\alpha(T)] + \frac{2\pi ni}{T} = \frac{1}{T} \int_0^T \{a(s) + b\} ds + \frac{2\pi ni}{T}$$

for  $n = 0, \pm 1, \pm 2, \dots$ . Note that the exponential solution for  $\xi(t)$  approaches zero as  $t \rightarrow \infty$ , if the real part of  $\sigma$  is negative. A time-integration during a full period  $T$  is required to calculate  $\sigma$ .

Regarding the system of ordinary differential Eqn. (2.13), the Floquet analysis can be implemented by incorporating a fundamental solution matrix,  $\mathbf{X}(t)$ , of size  $N \times N$ . The columns involved in  $\mathbf{X}(t)$  are the  $N$  linearly independent solutions of Eqn. (2.13) satisfying the boundary conditions. The initial conditions are imposed to the system (2.13) giving linearly independent solutions for a set of  $N$ . If the Floquet exponent,  $\sigma$ , and a  $T$ -periodic column vector  $\boldsymbol{\beta}(t)$  are considered, the solution of Eqn. (2.13) is

$$\boldsymbol{\eta}(t) = \boldsymbol{\beta}(t) e^{\sigma t}.$$

In general, the fundamental solution matrix can be constructed by numerically solving  $N$  initial value problems of Eqn. (2.13) with  $N$  columns of the  $N \times N$  identity matrix as the initial conditions. Note that the  $j$ -th column of  $\mathbf{X}(t)$  is the solution related to the  $j$ -th column of the identity matrix  $\mathbf{I}$  presented as an initial condition. According to the general aspects of the Floquet theory, the monodromy matrix can be formed by computing the fundamental solution matrix at  $t = T$ , namely  $\mathbf{X}(T)$ . The Floquet multipliers,  $\gamma_j$ , may be defined as the eigenvalues of  $\mathbf{X}(T)$  for  $j = 1, \dots, N$ , and as a result, the Floquet exponents,  $\sigma_j$ , are determined by

$$\sigma_j = \frac{1}{T} \{ \ln |\gamma_j| + i \arg[\gamma_j] \} + \frac{2\pi ni}{T} \quad (2.16)$$

for  $n = 0, \pm 1, \pm 2, \dots$ , or  $\gamma_j = \exp[\sigma_j T]$ . In Eqn. (2.16), when  $\text{Re}[\sigma_j] < 0$  for  $j = 1, \dots, N$ , the solution decays exponentially as  $t \rightarrow \infty$ . In addition, for all Floquet multipliers in the spectrum of monodromy matrix, the solution is stable when  $|\gamma_j| < 1$  (see [Iooss & Joseph](#)



(1990)). In the case where there is only one unstable mode, [Robichaux \*et al.\* \(1999\)](#) discussed a method by which the magnitude of the largest Floquet multiplier can be calculated. However, in order to implement the Floquet theory numerically in any case, a very high accuracy in both time advancement and spatial discretization should be achieved for a good representation of the flow field.

### 2.2.2 Multiple scales method applied to the model equation

The analysis of the multiple scales method suggests that a uniformly valid expansion can be achieved for all times of disturbance growth or decay. Since this technique deals with the time scales very effectively, it has been used for unsteady flows to predict the transient behavior and the frequency of the system. To convert the linear stability equation into an eigenvalue problem, the slow time scale is assumed for the base velocity whereas the fast time scale represents the disturbance. Referring to other studies of Stokes flows, [Cowley \(1987\)](#) and [Monkewitz & Bunster \(1987\)](#) utilized the modified multiple scales formulation. The new technique of [Lee \(2002\)](#) converting the spatial multiple scales of [Saric & Nayfeh \(1975\)](#) to temporal multiple scales was applied to the oscillatory planar Poiseuille flows to study the linear instabilities. If the method of [Lee \(2002\)](#) is utilized to Eqn. (2.14), the solution is

$$\xi(t) = \varphi(t_1; \varepsilon) e^{i\theta},$$

where  $\varepsilon$  is a dimensionless parameter appearing as a factor in  $t_1 \equiv \varepsilon t$  with a slow time,  $t_1$ , and a fast time,  $t$ . Note that both the multiple scales and the quasi-steady methods for disturbed laminar flows tackle the fast variation of disturbance (see 2.3.1). Since  $a(t)$  in Eqn. (2.14) resembles  $\mathbf{A}(t)$ , where the laminar flow in Eqn. (2.13) is contained, it can be formulated in terms of  $t_1$ , viz.,  $a(t_1)$ . A part of the exponent,  $\theta$ , is defined as

$$\theta = -\frac{1}{\varepsilon} \int \omega(t_1) dt_1,$$

and then  $d\theta/dt = -\omega(t_1)$  by which the chain rule associated with the time derivative of Eqn. (2.14) is

$$\frac{d}{dt} = \frac{\partial}{\partial \theta} \frac{d\theta}{dt} + \frac{\partial}{\partial t_1} \frac{dt_1}{dt} = -\omega(t_1) \frac{\partial}{\partial \theta} + \varepsilon \frac{\partial}{\partial t_1}.$$

In order to convert the differential Eqn. (2.14) into an eigenvalue problem without considering any time-integration,  $\varphi(t_1; \varepsilon)$  can be written in the form of series with a small parameter  $\varepsilon$  as in

$$\varphi(t_1; \varepsilon) = \varphi_0(t_1) + \varepsilon \varphi_1(t_1) + \varepsilon^2 \varphi_2(t_1) + \dots,$$

and this series expansion and other relations mentioned above are substituted into Eqn. (2.14) so that the resulting zeroth-order equation for  $\varphi_0(t_1)$  produces the eigenvalue,

$$\omega(t_1) = \{a(t_1) + b\} i,$$

for any nontrivial solution,  $\varphi_0(t_1)$ . The solution errors of the eigenvalue and  $\varphi_0(t_1)$  can be estimated to be on the order of  $\varepsilon$ , or  $O(\varepsilon)$ . However,  $\omega$  does not incorporate  $\varepsilon$  since  $\varepsilon$  is not involved in the expansion of the eigenvalue. When  $\text{Im}[\omega(t_1)] > 0$ , the solution is unstable, and it becomes stable if  $\text{Im}[\omega(t_1)] < 0$ . This special variation of the multiple scales method is able to examine the flow stability by only calculating the eigenvalue  $\omega(t_1)$ , which is independent of  $\varepsilon$ , meaning that the first-order and higher-order equations are not required to be solved. Note that, to achieve a high accuracy for  $\varphi(t_1)$ , the first-

order equation involving the time derivative of  $\varphi_0(t_1)$  should be solved. In fact, one can find a relation between the eigenvalue,  $\omega(t_1)$ , and the Floquet exponent mathematically as it will be presented in the following sections.

### 2.2.3 Present method for the model equation (quasi-steady method)

The linear stability of oscillating flows can be studied with a simpler method than those of the Floquet theory and the multiple scales approach. In fact, the proposed quasi-steady formulation is similar to those reported in the literature regarding the partial differential equations of hydrodynamic stability problems, as it will be shown in the following analyses. Recalling the simple model Eqn. (2.14), the assumption suggests that the equation admits the solution of a complex form,

$$\xi(t) = \xi(0) \exp \left[ -i \int_0^t \omega(s) ds \right]. \quad (2.17)$$

By using this equation, the time-derivative of  $\xi$  in Eqn. (2.14) is eliminated, and the differential equation can be transformed into an eigenvalue problem without requiring a temporal integration. If the solution in Eqn. (2.17) is substituted into Eqn. (2.14), the eigenvalue of the system is

$$\omega(t) = \{a(t) + b\}i.$$

It turns out that the result of Eqn. (2.17) and that of the Floquet theory in 2.2.1 regarding the solution  $\xi(t)$  are the same, and the eigenvalue of Eqn. (2.17) is equivalent to that produced by the method of multiple scales in 2.2.2. Furthermore, the simplicity of Eqn. (2.17) allows to add another time-dependent function to the solution of  $\xi(t)$ , for example,

$$\xi(t) = \xi(0)f(t) \exp \left[ -i \int_0^t \omega(s) ds \right],$$

from which the exact solution simply reveals that  $f(t) = 1$ . Therefore, the time-dependence of  $\xi(t)$  can be sufficiently assessed by the exponential function of the quasi-steady formulation, in contrast to the Floquet method. When  $\text{Im}[\omega(t)] > 0$ , the solution grows instantaneously, whereas  $\text{Im}[\omega(t)] < 0$  indicates the decay of the solution. If  $a(t) + b$  is periodic, a relation between  $\sigma$  and  $\omega$  can be extracted as follows:

$$\text{Re}[\sigma] = \frac{1}{T} \ln \alpha(T) = \frac{1}{T} \int_0^T \text{Im}[\omega(t)] dt,$$

since the equations of the Floquet theory yield

$$\alpha(t) = \exp \left[ \int_0^t \text{Im}[\omega(s)] ds \right].$$

For the model equation in Eqn. (2.14), the real part of the Floquet exponent is equal to the cycle average of  $\text{Im}[\omega(t)]$  calculated either by the quasi-steady method or by the multiple scales method in 2.2.2. In summary, the formulation presented herein gives the possibility of calculating the solution of the model Eqn. (2.14) more efficiently than the other two methods discussed earlier. The technique is able to find the instantaneous growth as well as the long-term growth of an oscillating function such as  $a(t) + b$  more easily at various flow conditions. In addition, this method can be applied to aperiodic  $a(t) + b$ , but the interpretation may be unclear when extended to hydrodynamic stability problems.

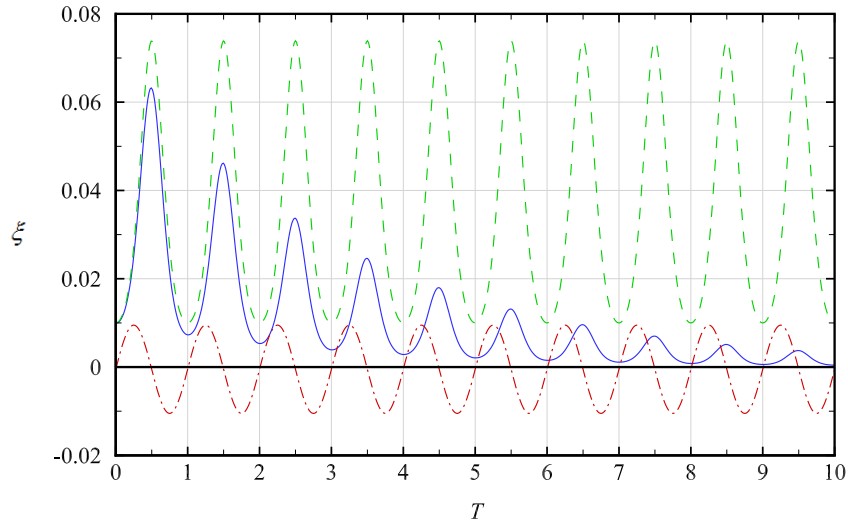


**Figure 2.1:** Exact solutions (blue solid and green dashed curves) of Eqn. (2.14) combined with the growth rate,  $\text{Im}[\omega(t)] \times 10^{-2}$ , predicted using the quasi-steady method (red dash-dotted curve) for  $a(t) = \sin(t)$ ,  $\xi(0) = 0.01$ , and  $0 \leq t \leq 10T$ : blue solid curve;  $b = -0.05$ , green dashed curve;  $b = 0$ .

The exact solutions of Eqn. (2.14) are shown in Fig. 2.1 at  $0 \leq t \leq 10T$  to highlight some important information. The blue solid curve is for  $a(t) = \sin(t)$ ,  $\xi(0) = 0.01$  and  $b = -0.05$ , and the green dashed curve is for the same  $a(t)$  and  $\xi(0)$  but  $b = 0$ . The comparison is made with the red dash-dotted curve representing  $\text{Im}[\omega(t)] \times 10^{-2}$ , calculated by the quasi-steady method for the blue solid curve with  $b = -0.05$ . The growth rate of the green dashed curve was also produced, but not shown since it turns out to be nearly the same as that of the red dash-dotted one. The equality in  $\text{Re}[\sigma] = b$  denotes the decay of solution for the blue solid curve in Fig. 2.1. The long-term decay of the solution indicated by the Floquet exponent is equally estimated by the cycle-averaged growth rate of the quasi-steady formulation. Although both Floquet and quasi-steady methods have exactly the same prediction of the long-term or cycle-averaged growth rates of the simple model Eqn. (2.14), there is no proof currently that the Floquet exponent of the partial differential Eqn. (2.12) is equivalent to the cycle-averaged growth rates of the quasi-steady solution for Eqn. (2.12).

Furthermore, two important points can be described about the green dashed curve in Fig. 2.1. First, the solution being considered is neutrally stable in the Floquet sense since the Floquet exponent is zero, although there is a large magnitude of  $\xi$  continuing its appearance in a part of each cycle and indicating a possible transient instability. This behavior raises a question that the Floquet exponent alone may not be sufficient for a transient instability prediction during an oscillation cycle in spite of its ability to determine the disturbance growth or decay over each cycle. Second, as clarified in Fig. 2.1, the quasi-steady method also leads to a neutral stability, and in addition, it can explain the large instantaneous growth of the solution within the cycle. Therefore, the quasi-steady method may be more relevant than the Floquet exponent in detecting the periodic turbulence bursts, although it requires an *ad hoc* stability criterion that ties with the magnitude of disturbance amplitude. Additionally, the validity of the quasi-steady assumption must be verified before it is used for the hydrodynamic stability equations, since the solution may not be sufficiently accurate in certain problems as will be explained in 2.3.2.

#### 2.2.4 Extension to the hydrodynamic stability problem

As demonstrated in the previous section, the current method is simpler in both formulation and implementation than the Floquet theory and the multiple scales method in seeking a solution for Eqn. (2.12). In order to extend the method to the hydrodynamic problem, it is proposed that

$$\eta(t, r) = \phi(r) \exp \left[ -i \int_0^t \omega(s) ds \right], \quad (2.18)$$

where  $\phi$  and  $\omega$  are complex functions. Equation (2.18), categorized as an *ad hoc* method due to  $\phi(r)$ , is very close to the equation of Luo & Wu (2010) used in their quasi-steady analysis for the stability of finite Stokes layer. Luo & Wu (2010) reported that their quasi-

steady results are highly accurate when  $Re_\delta \gg 1$ . Furthermore, direct numerical simulations (DNS's) were performed by [Akhavan \*et al.\* \(1991\)](#) for oscillatory Stokes flows, and their results, showing the transient growth of infinitesimal disturbance, agree well with the predictions of the quasi-steady theory for  $Re_\delta \gg 1$ .

In Eqn. (2.18), the time dependence of  $\phi$  is not shown explicitly, but the time-varying eigenvalue,  $\omega$ , allows the estimation of the corresponding eigenfunction,  $\phi$ , at each instant. The dependence of  $\phi$  on time in the current quasi-steady analysis is parametric, viz.,  $\phi(r;t)$ . [Drazin & Reid \(1981\)](#) reported that the method of normal modes for steady flows is not necessarily valid for unsteady base flows because the separation of the exponential time-dependence of disturbance cannot be attained due to time-dependent coefficients. However, the normal modes in the stability analysis of steady flows is not the same as what Eqn. (2.18) implies, regarding the disturbance stream function,  $\psi$ , employing  $\eta$  proposed in Eqn. (2.18). In this regard, [Drazin & Reid \(1981\)](#) noted that a solution had been obtained by [Shen \(1961\)](#) with the eigenfunction considered in the same way for the stability analysis of a type of unsteady flow. Further discussion about the time-dependence of  $\phi$  will be given later in this study, and the accuracy of the quasi-steady assumption in Eqn. (2.18) will be assessed in 2.3.1 because it can be estimated *a posteriori*.

When Eqn. (2.18) is substituted into Eqn. (2.12), the following stability equation appears:

$$L^2(\phi) - ikRe_\delta \left\{ (U - c)L(\phi) + \left( \frac{1}{r} \frac{\partial U}{\partial r} - \frac{\partial^2 U}{\partial r^2} \right) \phi \right\} = 0, \quad (2.19)$$

where  $c \equiv \omega/k$ . Equation (2.19) casts the generalized boundary-value eigenvalue problem with four boundary conditions,  $\phi = 0 = \phi'$  at the wall and the axis of symmetry. The parameter  $c$  is a complex eigenvalue and represents the wave velocity scaled by  $\hat{u}^*$ , and  $\phi$  is the complex eigenfunction nondimensionalized by  $\hat{u}^* \cdot (\delta^*)^2$ . This equation, which is a fourth-order ordinary differential equation for the disturbance amplitude  $\phi$ , is Orr-

Sommerfeld equation with time-dependent coefficients (parametric stability problem).

It is known that the hydrodynamic stability problem is classified into a spatial and/or a temporal stability problem. The second type is chosen for this study, where the disturbance waves evolve with time. If the growth rate of disturbance,  $\text{Im}[\omega]$  or  $\text{Im}[c]$  with a real  $k$  and a complex  $\omega$ , is positive, it means the flow has a locally unstable mode. Based on this criterion, the flow is described monotonically stable if all the  $\text{Im}[\omega]$  values decay monotonically at each moment, whereas the flow is unstable if a disturbance grows over a cycle. The importance of  $\text{Im}[\omega]$  value is more manifested in the transient instability, where some disturbances grow partly during the period but decay in the rest of the cycle (see, [Davis \(1976\)](#), [Monkewitz & Bunster \(1987\)](#)).

The explicit time dependence of  $\phi$  was included in the multiple scales formulation of [Lee & Beddini \(1999\)](#) by employing a small expansion parameter for planar channel problems. They acquired the leading-order equation which is basically the planar counterpart of Eqn. (2.19). Based on their analysis, the appearance of the time derivative of  $\phi$  is only in the first-order equation (but not in the leading-order equation). Since the eigenvalues are independent of the expansion parameter, they were obtained only from the leading-order equation. In other words, the eigenvalues evaluated by the multiple scales formulation do not involve the explicit time-dependence of the eigenfunction, as a consequence of converting the spatial multiple-scales analysis performed by [Saric & Nayfeh \(1975\)](#) into a temporal one using multiple scales in time. Another implication that can be pointed out is that if the multiple scales method of [Lee & Beddini \(1999\)](#) is utilized for the current analysis, the zeroth-order equation will be equivalent to Eqn. (2.19) with  $\phi$  replaced by  $\phi_0$  and will produce the same eigenvalues. Therefore, under those circumstances, the solution accuracy for  $\phi$  (but not the eigenvalue) in Eqn. (2.19) can be elucidated as being of the order of a small expansion parameter similar to that used in 2.2.2. The reason for the interpretation is that  $\phi$  does not have an explicit time-dependence in Eqn. (2.18), which



can be related to the frozen profiles of the laminar flow with respect to the fast variation of disturbance. Recall that, the expansion parameter in 2.2.2 will be the ratio of the slow time of laminar flow to the fast time of disturbance if it is applied to the hydrodynamic stability.

### 2.2.5 Transformation of the hydrodynamic stability problem

The  $r$ -coordinate in Eqn. (2.18) and Eqn. (2.19) is now rescaled using  $\zeta \equiv r/\lambda$ , where

$$\lambda = \frac{R^*}{\delta^*} \quad (2.20)$$

is the nondimensional duct radius called Stokes number, or Womersley number that differs by a factor of  $\sqrt{2}$ , so that  $0 \leq \zeta \leq 1$  since  $\zeta = r^*/R^*$  with  $R^*$  representing the dimensional duct radius. With this transformation, Eqn. (2.19) is rewritten as

$$\mathcal{L}^2(\Phi) - i\kappa\lambda Re_\delta \left\{ (U - c)\mathcal{L}(\Phi) + \left( \frac{1}{\zeta} \frac{\partial U}{\partial \zeta} - \frac{\partial^2 U}{\partial \zeta^2} \right) \Phi \right\} = 0, \quad (2.21)$$

where  $\kappa = k^*R^*$  is the  $k^*$  scaled by the pipe radius,  $\Phi$  is  $\phi^*$  nondimensionalized by  $\hat{u}^* \cdot (R^*)^2$ , albeit the scaling of eigenfunction is insignificant, and the operator  $\mathcal{L}$  is written as

$$\mathcal{L} \equiv \frac{\partial^2}{\partial \zeta^2} - \frac{1}{\zeta} \frac{\partial}{\partial \zeta} - \kappa^2.$$

Note that, in Eqn. (2.21),  $\Phi$  is a function of  $\zeta$ , and  $U$  depends on both  $\zeta$  and time. The stability of unsteady flow characterized by  $U$  is determined by the three parameters,  $\kappa$ ,  $\lambda$  and  $Re_\delta$ . The boundary conditions at the pipe centerline ( $\zeta = 0$ ) and at the wall ( $\zeta = 1$ ) are both given by

$$\Phi = 0 = \frac{\partial \Phi}{\partial \zeta}.$$

The solution of unsteady laminar velocity subjected to a long-time oscillation is normalized by the velocity amplitude at the axis of symmetry and written in terms of the Stokes number,  $\lambda$ , as follows (Sexl (1930)):

$$U(\tau, \zeta) = \left| \frac{J_0(\sqrt{-2i}\lambda)}{J_0(\sqrt{-2i}\lambda) - 1} \right| \cdot \text{Re} \left[ \left\{ 1 - \frac{J_0(\sqrt{-2i}\lambda \zeta)}{J_0(\sqrt{-2i}\lambda)} \right\} \frac{e^{i\Omega\tau}}{i} \right], \quad (2.22)$$

where  $J_0$  is the Bessel function of the first kind, and  $\Omega$  and  $\tau$  are the angular frequency and the time nondimensionalized by  $\hat{u}^*/R^*$  and  $R^*/\hat{u}^*$ , respectively. As a remark, Eqn. (2.22) with the parameter  $\Omega = 2\lambda/Re_\delta$  is the base flow in this thesis. In addition, the reciprocal of the dimensionless velocity amplitude at the axis of symmetry in Eqn. (2.22) becomes unity when  $\lambda \geq 12$ , i.e.,

$$\left| \frac{J_0(\sqrt{-2i}\lambda)}{J_0(\sqrt{-2i}\lambda) - 1} \right| \approx 1.$$

The eigenvalue problem, Eqn. (2.21), with four boundary conditions can be solved by a few different numerical methods. In this study, the Chebyshev pseudo-spectral matrix (CPSM) approach is selected for the spatial discretization in  $\zeta$ . This numerical scheme incorporates highly accurate spatial derivatives with a Chebyshev series spanning the global domain, and the boundary conditions can be applied more efficiently than those of the Galerkin spectral method.

### 2.2.5.1 Chebyshev polynomials

There are two common types of interpolants regarding the orthogonal basis function that can be utilized for the spatial discretization: Legendre and Chebyshev polynomials. The former deals with the Legendre points of Gauss quadrature with an order of  $2N-1$ , and the following expression is usually used for the Chebyshev case:

$$P(x_c) = \sum_{n=0}^N a_{c_n} T_{c_n}(x_c) \quad x_c \in [-1, 1], \quad (2.23)$$

where  $P$  is a linear combination of Chebyshev polynomial ( $T_c$ ) of degree  $N$ , and  $a_c$  is a coefficient which can be obtained from the discrete orthogonality condition. This type of expansion is treated with Dirac delta functions which are centered at the collocation points ( $x_c$ ) with a unit magnitude and zeros at other locations. The discrete points known as Chebyshev points are

$$x_{c_i} = \cos\left(\frac{i\pi}{N}\right) \quad 0 \leq i \leq N.$$

The distribution of these points is demonstrated in Fig. 2.2, where evenly spaced points on a unit semicircle are projected on a horizontal line to create the Chebyshev nodes.

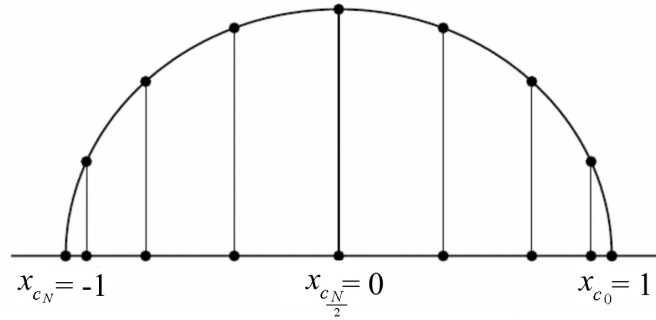


**Figure 2.2:** Chebyshev points obtained by the projection of radially equispaced points on a horizontal line as shown by [Trefethen \(2000\)](#).

Thus, these collocation points, also called Gauss-Lobatto grid points, are the roots of the Chebyshev polynomials of the first kind in the interval  $(-1, 1)$ . With an appropriate number of these points, especially in the near-wall region, the solution for problems involving a small boundary layer thickness can be adequately evaluated ([Fletcher \(1991\)](#), [Peyret \(1986\)](#)).

### 2.2.5.2 Chebyshev Derivatives

The stability Eqn. (2.21) is converted into a matrix eigenvalue problem via CPSM. The explicit formulae for the lower order derivatives can be found in some references (see, for example, [Peyret \(2002\)](#)). The first derivative matrix with the Gauss-Lobatto collocation points in a domain  $(-1, 1)$  is

$$D_{ij}^{(1)} = \begin{cases} \frac{c_i(-1)^{i+j}}{c_j(x_{c_i}-x_{c_j})}, & 0 \leq i, j \leq N, \quad i \neq j \\ -\frac{x_{c_i}}{2(1-x_{c_i}^2)}, & 1 \leq i = j \leq N-1 \\ D_{00}^{(1)} = -D_{NN}^{(1)} = \frac{2N^2+1}{6}, & \end{cases}$$

and the equation of the second derivative is

$$D_{ij}^{(2)} = \begin{cases} \frac{(-1)^{i+j}(x_{c_i}^2+x_{c_i}x_{c_j}-2)}{c_j(1-x_{c_i})^2(x_{c_i}-x_{c_j})^2}, & 1 \leq i \leq N-1 \\ & 0 \leq j \leq N, i \neq j \\ -\frac{(N^2-1)(1-x_{c_i}^2)+3}{3(1-x_{c_i}^2)^2}, & 1 \leq i = j \leq N-1 \\ \frac{2(-1)^j(2N^2+1)(1-x_{c_j})-6}{3c_j(1-x_{c_j})^2}, & i = 0, 1 \leq j \leq N \\ \frac{2(-1)^{j+N}(2N^2+1)(1+x_{c_j})-6}{3c_j(1+x_{c_j})^2}, & i = N, 0 \leq j \leq N-1 \\ \frac{N^4-1}{15}, & i = j = 0, N \end{cases}$$

where  $c_i = 2$  for  $i = 0, N$  and  $c_j = 1$  for  $1 \leq j \leq N-1$ . The strategy of mapping the collocation points on the axisymmetric domain of  $(0, 1)$  is to utilize the chain rule, where the spatial discretization is performed with collocation points  $(\zeta_j)$  described by

$$\zeta_i = \frac{x_{c_i} + 1}{2} \quad \zeta \in [0, 1], \quad \text{for } i = 0, 1, \dots, N,$$

and then the derivatives with respect to  $\zeta$  can be found from

$$\frac{\partial}{\partial \zeta} = 2 \frac{\partial}{\partial x_c}, \quad \frac{\partial^2}{\partial \zeta^2} = 4 \frac{\partial^2}{\partial x_c^2},$$

where  $x_c$  are the general Chebyshev collocation points between -1 and 1. Equation (2.21) containing the third and fourth derivatives can be decomposed into two second-order differential equations to minimize the numerical errors in constructing higher-order matrices. Note that the singularity in Eqn. (2.21) can be avoided after applying the homogeneous boundary conditions to the matrix equation.

## 2.3 Results and Discussions

### 2.3.1 Flow stability by the quasi-steady method

The eigenvalue problem represented by the boundary-modified matrix system of Eqn. (2.21) was solved by utilizing LAPACK subroutines, adopting the generalized upper Hessenberg and the generalized Schur decomposition (see [Anderson \*et al.\* \(1994\)](#)). The accuracy of the numerical solution obtained using the CPSM and LAPACK routines was verified with pre-calculated eigenvalues for the axisymmetric steady Poiseuille flow, and the results showed a good agreement with those in the literature (see, for example, [Drazin & Reid \(1981\)](#)). In this study, the eigenvalues produced from the numerical solution of the quasi-steady method are either the most unstable ones with the highest growth rate,  $\text{Im}[\omega]$ , at each instant of time or the cycle-averaged values of those least stable modes. Note that the eigenvalues are complex numbers, and the growth rate of disturbance is calculated from the imaginary part only. The numerical convergence of the solution was examined at a few resolutions, and the number of collocation points was chosen to be 61 to ensure a sufficient accuracy at various flow conditions.

Figure 2.3 shows the time-varying growth rates during one period of laminar flow oscilla-

tion, computed at  $\lambda = 20$  and  $\kappa = 8$  for three different Reynolds numbers:  $Re_\delta = 80$  (blue dash-dot curve), 125 (green dashed curve) and 250 (red solid curve). It can be seen that the flow is stable during the entire period of oscillation at the lowest Reynolds number, although there are harmonic appearances in disturbance during the reversal times with values less than zero. In contrast, these sudden increases of growth rate climb to positive values indicating the instability of flow at the other two Reynolds numbers ( $Re_\delta = 125$ , and 250). The shown behaviors are somewhat consistent with the phenomenon of periodic turbulence and relaminarization within specific parts of the oscillation cycle, as observed in many experiments such as those of [Merkli & Thomann \(1975\)](#), [Hino \*et al.\* \(1976\)](#), [Iguchi & Ohmi \(1982\)](#), and [Zhao & Cheng \(1996\)](#).

In the bottom part of Fig. 2.3 (below the zero line), the variations of growth rates are so small in the presented scale that the curves appear to be straight lines. The quasi-steady method was also applied for  $Re_\delta$  of 500 and 1000, of which peaks of growth rates are represented by green circles and red squares, respectively, in Fig. 2.3. At a much higher  $Re_\delta$  of 1000, the value of  $\text{Im}[\omega]$  stays continuously positive during the whole cycle. However, at a low oscillation frequency with  $\lambda = 5.5$  (and  $\kappa = 1.6$ , close to the most unstable wave number), the growth rates declined to negative values within the cycle even for  $Re_\delta = 3 \times 10^6$ , although they are not shown in the figure.

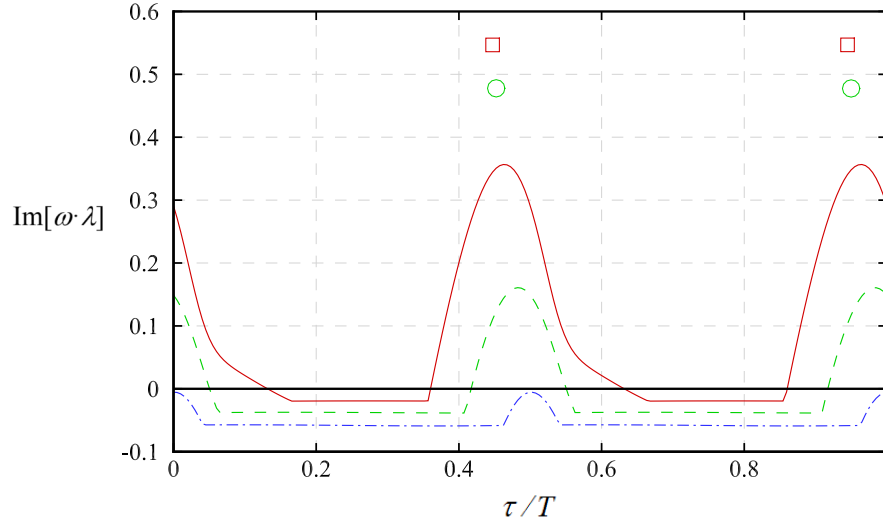


**Figure 2.3:** Results of quasi-steady method represented by instantaneous growth rates during a cycle at  $\lambda = 20$  and  $\kappa = 8$ :  $Re_\delta = 80, 125$  and  $250$  for blue dash-dotted, green dashed and red solid curves, respectively. The green circles are the peaks at  $Re_\delta = 500$ , and the red squares are the peaks at  $Re_\delta = 1000$ .

The relation between the velocity at the axis of symmetry and its first and second derivatives evaluated at the wall is illustrated in Fig. 2.4 for one oscillation cycle. The maximum magnitude of the second derivative represented by a red solid line in Fig. 2.4 is around the time when the pressure gradient ( $\partial p/\partial x$ ) proportional to  $\cos(\Omega \tau)$  reaches its extrema, associated with the zero velocity magnitude at  $\zeta = 0$ , the flow reversal, and the maximum tidal displacement of the fluid. Therefore, the peaks of disturbance growth in Fig. 2.3 occur at the aforementioned times, i.e.,  $\tau/T \approx 0, 0.5$ , and  $1$ . These results are in agreement with the experimental observation of [Monkewitz & Bunster \(1987\)](#) stating that the disturbances of Stokes layer first appear shortly before and at the flow reversal.

The Richardson's annular effect shown by circles in Fig. 2.4 varies similarly to  $U$  at  $\zeta = 0$  during the oscillation cycle with  $Re_\delta = 250$  and  $\lambda = 20$ . The zero magnitude of them seems to be slightly more in phase with the maximum growth rate of disturbance in Fig. 2.3, and the behavior persists at somewhat smaller values of Stokes numbers, although not



presented herein. Note that the phase difference between the laminar velocity and the pressure can be calculated from Eqn. (2.22). For example, the phase of laminar velocity at  $\zeta = 0$  is different from that of the pressure gradient by nearly 90 degrees at  $\lambda \geq 4$ , and this phase lag reverses at  $\tau/T$  close to 0.5 and 1. In contrast, at smaller values of  $\lambda$ , the phase shift becomes so small so that the velocity oscillates with a slowly varying  $\partial p/\partial x$  at  $\lambda < 1$  approximately.

At low oscillation frequencies, the velocity  $U$  and its spatial derivatives are of the same order of magnitude compared with their profiles at large values of  $\lambda$ , where the second derivative of  $U$  increases greatly owing to the thin boundary layer and dominates the stability Eqn. (2.21). In Fig. 2.4, the first and second spatial derivatives of  $U$  at  $\zeta = 1$  are scaled by some factors so that their maximum values are almost 800 times and 30 times that of  $U$  evaluated at  $\zeta = 0$ . The spatial derivatives of  $U$  are zeros at  $\zeta = 0$  due to the symmetry, and the overshoot of velocity is closer to the wall than to the central axis because of the Richardson's annular effect, but the maximum of  $|U|$  is still not much greater than unity at the laminar conditions. Therefore, Fig. 2.3 and Fig. 2.4 clarify the role of the laminar velocity derivatives on the coefficients and eigenvalues of the stability Eqn. (2.21), particularly the effect of the second derivative of velocity, of which extrema are related to the maximum growth rates of disturbance.

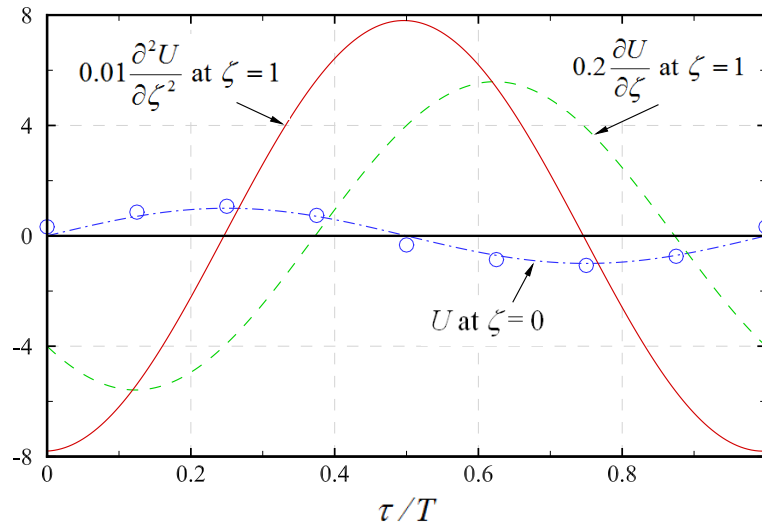


**Figure 2.4:** Time variation of the laminar base flow velocity at the axis of symmetry (blue dash-dotted curve) and its derivatives at the wall (green dashed and red solid curves for the first and second derivatives, respectively) for  $\lambda = 20$  and  $Re_\delta = 250$ . The circles are the near-wall velocity overshoot due to Richardson's annular effect.

Discrepancy was noticed by [Hino \*et al.\* \(1976\)](#) between the laminar velocity distribution in experiments and that of the theoretical solution, causing distortion with a significant amount of phase lag in the central region of the duct. Note that a slight deviation from the theoretical velocity distribution can consequently lead to a big difference in the magnitude of the second spatial derivative of  $U$ . Thus, it is believed that the comparison between experimental and theoretical results at the same conditions is not sufficiently meaningful unless an agreement is verified between the derivatives of  $U$  as well as  $U$  itself for the two approaches. For example, this accordance between the velocity derivatives is required to find an accurate onset of transition as will be shown in the next figures.

Some experiments showed that the flow becomes turbulent during the decelerating phase (see, [Iguchi & Ohmi \(1982\)](#), [Zhao & Cheng \(1996\)](#)) and then relaminarizes. However, depending on the flow conditions, transition to weakly turbulent flows was observed in the experiment of [Hino \*et al.\* \(1976\)](#) even when the velocity increases with time, whereas

most of the turbulence bursts were still detected during the deceleration phase of the velocity. Another distinctive remark was made by Merkli & Thomann (1975) that showed turbulence bursts, followed by an immediate relaminarization, only at the times when the velocity reached its peaks between the accelerating and decelerating phases. In contrast to what Hino *et al.* (1976)'s experiment revealed at the flow condition of weak turbulence, Kurzweg *et al.* (1989) could not find any sign of turbulence at the same conditions of Hino *et al.* (1976). These differences in the experimental observations and the reasons of a wide range of critical Reynolds numbers reported in the literature were attributed by some researchers to a few reasons – asymmetric or three-dimensional disturbances, turbulence detection techniques, dissimilarities in experimental conditions, and transition criteria.

The peaks of  $\text{Im}[\omega]$  shown in Fig. 2.3 for  $\lambda = 20$  shift slightly toward the beginning of the decelerating phase, where the flow begins to experience disturbance growths leading to instability, increasing further with  $Re_\delta$ . However, at low Stokes numbers (approximately less than 2), the increase in  $\text{Im}[\omega]$  obtained by the quasi-steady method was completely in phase with the deceleration of  $U$ , although the sign of  $\text{Im}[\omega]$  was negative throughout the whole cycle.

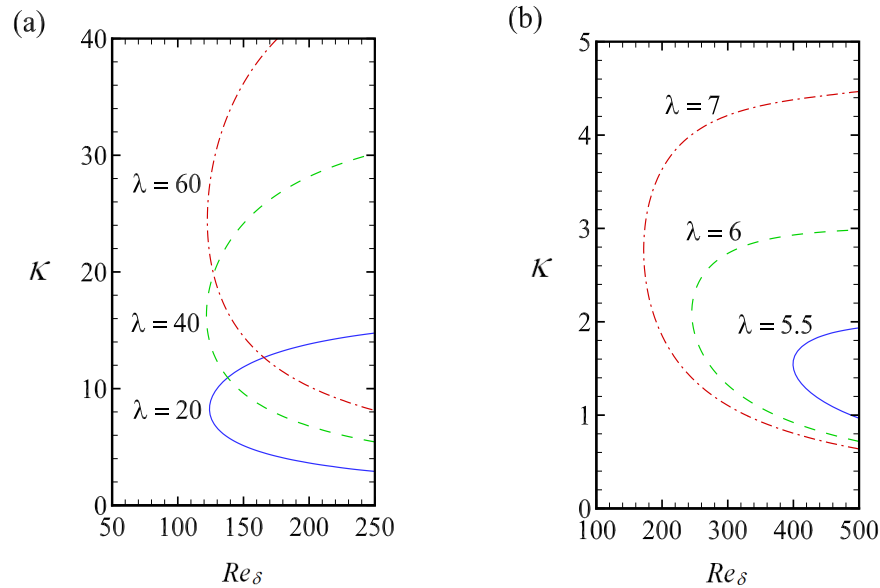


**Figure 2.5:** Neutral stability curves for six values of  $\lambda$  ranging from 5.5 to 60, computed by the cycle-averaged growth rates. Note the different scales in (a) and (b).

As mentioned previously in Chapter 1, there have been several attempts to provide a suitable stability criterion for the flow of interest, but none of them is quite satisfactory. For instance, [Hino \*et al.\* \(1976\)](#) stated that the energy stability theory tends to produce relatively low critical Reynolds numbers. Figure 2.5 displays two stability maps calculated by  $\frac{1}{T} \int_0^T \text{Im}[\omega(\tau)] d\tau = 0$ , a tentative criterion obtained from the cycle-averaged growth rate of the quasi-steady method. Note that the curves representing the neutral stability shown in Fig. 2.5 do not necessarily provide a proper stability criterion for the oscillating flows because of the reasons explained for Fig. 2.1. Note that the cycle-averaged growth rate from the simple model equation used in Fig. 2.1 is equivalent to the Floquet exponent, but it is not certain that the statement is also true for the partial differential Eqn. (2.12). More importantly, even if the flow is neutrally stable in the average, there is a possibility that the disturbance reaches very high amplitudes during part of the cycle and causes instability.

The stability maps are produced for large and small Stokes numbers: Fig. 2.5 (a) at 20, 40

and 60 and Fig. 2.5 (b) at 5.5, 6 and 7. The first map has wide areas of instability zones extending to higher wave numbers, which increase with the Stokes number while the critical Reynolds number remains almost the same. The trends of the neutral stability are close to those of the planar channel flow shown by Lee (2002) at large Stokes numbers, because the thin oscillatory boundary layer near the wall behaves similarly in the two geometries. Another remark is that whenever the Stokes number increases, the instability region becomes wider revealing that the flow sensitivity to disturbances with smaller size becomes higher as the thickness of the boundary layer decreases. The relative difference between the neutral stability curves appearing in different scales,  $0 < \kappa \leq 5$  and  $100 \leq Re_\delta \leq 500$ , is more manifested in Fig. 2.5 (b) at  $\lambda < 10$ . The figure shows that the critical Reynolds number varies inversely with  $\lambda$ , and the flow is more stable at the flow conditions of Fig. 2.5 (b) than those of Fig. 2.5 (a). The reason for the increasing stability at low Stokes numbers is because of the viscous effects dampening out the growth of disturbances, as noted by Kurzweg *et al.* (1989).

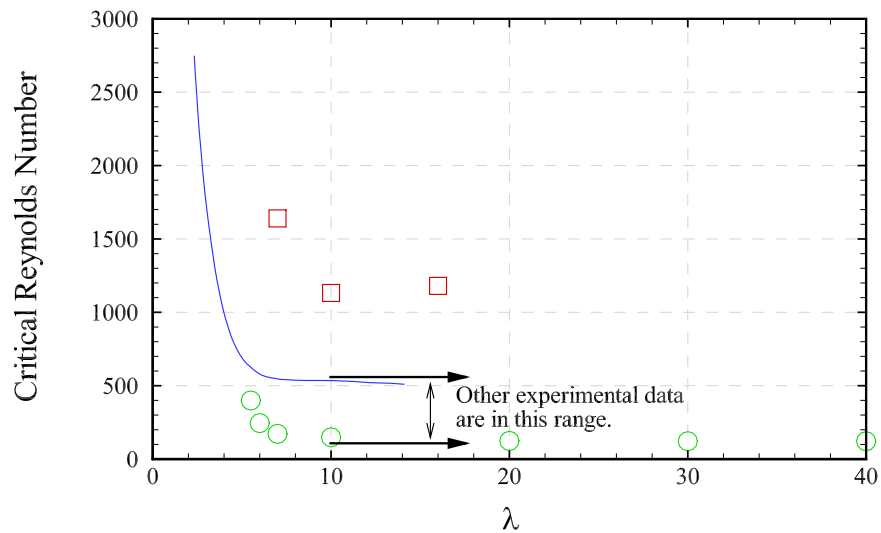


**Figure 2.6:** Critical Reynolds numbers calculated by the cycle-averaged growth rates of quasi-steady assumption (green circles) compared with those of Kurzweg *et al.* (1989)'s experiment (blue solid curve), Floquet analysis of Blennerhassett & Bassom (2006) (red squares), and 'Other experimental data' compiled by Cooper *et al.* (1993) (bounded area between the two arrows).

By utilizing the quasi-steady analysis, the critical Reynolds numbers were determined at different Stokes numbers and shown with green circles in Fig. 2.6. The experimental findings of *Kurzweg et al. (1989)*, depicted by a blue solid line, are plotted to show the transition in oscillating pipe flows. The theoretical results of the current study qualitatively agree with the stability trend of *Kurzweg et al. (1989)*. Note that the extended curve in the paper of *Kurzweg et al. (1989)* is not included in Fig. 2.6. It is clearly seen that the value of the critical Reynolds number of the current study decreases rapidly in  $5.5 \leq \lambda < 7$ , whereas it slightly changes for  $10 \leq \lambda < 20$  before it becomes nearly constant ( $\approx 123$ ) at large Stokes numbers,  $\lambda > 20$ . Note that the Reynolds number of *Kurzweg et al. (1989)* has been converted into  $Re_\delta$  since their Reynolds number incorporates the cross-stream averaged value of the velocity, of which the ratio to  $\hat{u}^*$  in  $Re_\delta$  is not a constant but a function of  $\lambda$ , and the equation of that conversion will be shown in the next chapter.

It should be mentioned that the hydrodynamic instability in the present analysis is predicted by the cycle-averaged growth rates, which is not necessarily an appropriate method for the flow being studied. This may explain the differences between the values of the present results and those of *Kurzweg et al. (1989)* shown in Fig. 2.6 despite the similar trends of the critical Reynolds number with respect to the Stokes number. With the tentative stability criterion proposed herein, it was found that the flow is stable even up to  $Re_\delta = 2500$  and  $\lambda = 5$ , and thus the critical Stokes number is approximately 5 and the flow is stable for  $\lambda < 5$ . When  $\Omega$  and  $\lambda$  decrease to zero, the laminar flow approaches the parabolic steady Poiseuille flow. In this regard, it is known experimentally that the steady Poiseuille flow in a pipe is stable with respect to all axisymmetric disturbances (see, for example, *Drazin & Reid (1981)*), and that is fairly consistent with the current findings. In addition, the resulting data of *Cooper et al. (1993)* located between the two horizontal arrows displayed in Fig. 2.6 are to show the bounded zone of critical Reynolds numbers for several experiments at  $\lambda \geq 10$ .

There is a similar formulation regarding the quasi-steady analysis presented in the study of [Das & Arakeri \(1998\)](#), but with a different stability criterion. They considered that all the positive growth rates indicate instability, declaring 82 as the critical Reynolds number at  $\lambda = 10$ . In [Fig. 2.6](#), the current critical Reynolds number is around 123 at  $\lambda = 10$ , somewhat higher than that of [Das & Arakeri \(1998\)](#). This discrepancy may be because that they regarded all positive growth rates as the instability even for a very short time, which are not likely sufficient for the flow to experience instability leading to transition – consider  $Re_\delta$  slightly higher than 80 in [Fig. 2.3](#), for example. A similar conclusion was reached via the experiment of [Das & Arakeri \(1998\)](#) when they noticed that enough time should be allowed for the disturbance growth to cause instability even if the critical Reynolds number is exceeded.

Therefore, the onset of transition for the flow studied herein depends not only on the positive values of growth rate, but also requires a sufficient time during which the flow sustains instability. Another point stated by [Das & Arakeri \(1998\)](#) was that their critical Reynolds number is related to the onset of disturbed laminar flows rather than the intermittently turbulent flows. Their findings explain somewhat higher critical Reynolds numbers of this study at turbulence condition, and they are also compatible with the experimental data reported in [Fig. 2.6](#). Some of those experiments clearly revealed disturbed laminar flows, and some of the declared turbulent flows were later considered as disturbed laminar flows.

Shown in [Fig. 2.6](#) with red square symbols, the study of [Blennerhassett & Bassom \(2006\)](#) presented the linear instability of the flow by applying the Floquet method to find the critical Reynolds numbers at certain flow conditions. Neither their values nor their trends are in agreement with those of [Kurzweg \*et al.\* \(1989\)](#) and the current quasi-steady results. [Blennerhassett & Bassom \(2006\)](#) noticed that two direct numerical simulations had shown turbulence at the conditions where their Floquet analysis indicates stability, albeit their

results were not directly related to the two DNS results of Juárez & Ramos (2003) and Cosgrove *et al.* (2003).

The Floquet instability of Blennerhassett & Bassom (2006) can be interpreted as the global instability of disturbances growing over each cycle, different from the transient instability by which the flow may be disturbed or the flow experiences periodic turbulence bursts at the Reynolds numbers much lower than those of the global instability. This interpretation is partly in line with the results of the simple model equation used in Fig. 2.1, where the transient growth of the solution was not predictable by the Floquet method. In addition, the direct numerical simulation of Singer *et al.* (1989) for a modulated channel flow showed that the instantaneous strength of disturbances can be high enough to trigger transition even when the Floquet theory declares stability. Moreover, because the linearization could be questioned if the large Reynolds numbers of Blennerhassett & Bassom (2006) are considered, Luo & Wu (2010) reported that the Floquet instability is not necessarily more relevant than that of the quasi-steady method in the linear perspective, even though it is mathematically more rigorous.

Furthermore, Feldmann & Wagner (2012) discussed the stability of this flow and reported that the Floquet method can only be used to capture the long-term instability for unsteady base flows because of its limitations in predicting the transient instability, as Zhao *et al.* (2004) and Trukenmüller (2006) had stated. Note that the study of Trukenmüller (2006) was also mainly about the quasi-steady method for the same flow considered herein, but the results are not included in Fig. 2.6 because the critical Reynolds number curve was found to be incompatible with the value obtained at a condition of the DNS results of Feldmann & Wagner (2012).



### 2.3.2 Approximate accuracy of the quasi-steady method

The explanation found in the literature review of Ghidaoui & Kolyshkin (2002) stated that the quasi-steady approach can be interpreted as the first term in the asymptotic expansion of WKB type. In their study, the instability of pipe flow subject to rapid acceleration and/or deceleration was investigated and an important remark was made that, although the quasi-steady approximation can be used successfully to predict transition, the accuracy of the results may not be sufficient in certain cases. In fact, there are a few researchers who studied the oscillating flow transition via the quasi-steady approximation, although the validity of their applications and/or results may not be acceptable. The majority requires two bases in order to verify the assumptions involved in the quasi-steady analysis. The first is that  $Re_\delta$  should be large enough, but this assessment has uncertainty since the limits are not provided. The second is that the growth rate of disturbance,  $\text{Im}[\omega]$ , should be much higher than the angular frequency (or the rate of change) of laminar flow. In fact, the latter can be evaluated only *a posteriori*, and the role of  $\text{Re}[\omega]$ , the frequency of disturbance, in the stability analyses may be more important than  $\text{Im}[\omega]$ .

Hereafter, the above two conditions are combined in a more comprehensive criterion by maintaining the time-derivative of  $\phi$  on the left side of Eqn. (2.12) when Eqn. (2.18) is substituted, i.e., by incorporating the time-dependence of  $\phi$ . After the exponential function is canceled out, Eqn. (2.12) becomes

$$L\left(\frac{\partial\phi}{\partial t} - i\phi\omega\right) = -ik\left\{UL(\phi) + \left(\frac{1}{r}\frac{\partial U}{\partial r} - \frac{\partial^2 U}{\partial r^2}\right)\phi\right\} + \frac{1}{Re_\delta}L^2(\phi). \quad (2.24)$$

Under the assumption of the quasi-steady formulation,  $(\frac{\partial\phi}{\partial t} - i\phi\omega)$  is replaced with  $(-i\phi\omega)$ , by which Eqn. (2.18) through Eqn. (2.21) can be verified. This reduction is suitable as long as the condition of  $O(\frac{\partial\phi}{\partial t}) \ll O(i\phi\omega)$  is valid. After taking the medium value of  $t$

during an oscillation cycle with  $0 \leq t \leq 2\pi\lambda/\Omega$  and by using  $\Omega = 2\lambda/Re_\delta$ , one can find that  $\frac{\partial\phi}{\partial t}$  is  $O(\frac{2\phi}{\pi Re_\delta})$  in Eqn. (2.24). Note that the mean magnitude of  $1/t$  equals  $2/(\pi Re_\delta)$ , and if  $2/(\pi Re_\delta) \ll |\omega|$ , the term  $O(\frac{2\phi}{\pi Re_\delta})$  can be omitted in the average sense. Based on these details of Eqn. (2.24), the following inequality is introduced as a simple basis for the quasi-steady assumption by accounting for the time variation of the complex  $\omega$ :

$$\frac{2m}{\pi Re_\delta} \leq \frac{1}{T} \int_0^T |\omega| d\tau, \quad (2.25)$$

where the parameter  $m$  determines the size of  $O(\frac{\partial\phi}{\partial t})$  relative to that of  $O(i\phi\omega)$  in the average during an oscillation cycle. Therefore, the approximate amount of error encountered in the quasi-steady analysis can be estimated by calculating the value of the parameter  $m$ . For example, the error in  $\omega$  of the quasi-steady method is on the order of one percent or smaller if  $m = 100$ . Moreover, it can be seen that both  $\text{Re}[\omega]$  and  $\text{Im}[\omega]$  are involved in the condition of Eqn. (2.25) since Eqn. (2.24) has  $\omega$  and  $\phi$  which are complex.

Consequently, according to the criterion in Eqn. (2.25), when  $Re_\delta$  is large, the magnitude of  $\frac{\partial\phi}{\partial t}$  will be small, and it is naturally related to a low frequency of the base flow, implying a small rate of change of the laminar flow. Thus,  $Re_\delta$  is not required to be infinitely large to obtain accurate results as Luo & Wu (2010) confirmed, and  $\text{Re}[\omega]$  is as significant as  $\text{Im}[\omega]$  for the quasi-steady assumption. In other words, the results produced from the quasi-steady analysis are still accurate even if  $\text{Im}[\omega]$  is small and  $Re_\delta$  is not very high, when  $\text{Re}[\omega]$  is sufficiently large to satisfy Eqn. (2.25). To provide some examples of the approximate accuracy of the current theory, the presented Eqn. (2.25) was utilized and some values are listed in Tab. 2.1. The approximate percent errors of  $\omega$  in the average during a cycle are also incorporated into Tab. 2.1 to show how the accuracy of the quasi-steady method changes with the flow conditions. When  $Re_\delta = 1000$ , it turns out that the error is reduced to 0.29 % at  $\kappa = 8$  and  $\lambda = 20$  in comparison with the error of 0.45 % at

$\kappa = 1.5$  and  $\lambda = 5.5$ . In addition, the presented numbers in Tab. 2.1 show that the eigenvalues employed to create the critical  $Re_\delta$  curve plotted in Fig. 2.6 are reasonably accurate. Note that, in Tab. 2.1, because the dimensional eigenvalue is normalized by  $\hat{u}^*/\delta^*$ , there is a small decrease in the cycle-averaged  $|\omega|$  with increasing  $Re_\delta$ .

**Table 2.1:** Approximate percent errors of  $\omega$  obtained according to the mathematical relation in Eqn. (2.25) with various flow conditions.

$\lambda = 20$ and $\kappa = 8$			
$Re_\delta$	$(1/T) \cdot \int_0^T  \omega  d\tau$	$m$	Error (%)
80	0.258	32.5	3.08
125	0.248	48.7	2.05
250	0.239	94.0	1.06
1000	0.220	346.2	0.29
$\lambda = 5.5$ and $\kappa = 1.5$			
$Re_\delta$	$(1/T) \cdot \int_0^T  \omega  d\tau$	$m$	Error (%)
100	0.164	25.8	3.88
200	0.158	49.6	2.01
400	0.153	96.1	1.04
1000	0.141	221.5	0.45

# Chapter 3

## Transition in Purely Oscillating Pipe Flow

### 3.1 Overview

Previous studies on the transition of oscillating flows showed several important remarks. Because of its relevance of causing many engineering problems, investigators have made tremendous efforts to explore all the scenarios involved in the transition process. The preliminary signs of transition may appear as natural modes like Tollmien-Schlichting waves or sometimes as forced modes like periodic unsteady wakes. Herein, to verify the theoretical results of this study under various oscillation frequencies, a more sophisticated tool such as direct numerical simulation (DNS) has to be utilized to fully understand the whole process of transition.

The onset of flow instability is uncertain since it is not clearly determined under different conditions in the previous studies. It is partly because there are several factors altering the transition thresholds so that the critical conditions are not estimated accurately without

defining a suitable criterion. Some experimentalists stated that the appearance of turbulence bursts or shear stress fluctuations near the wall are the common ways to announce the transition, and the critical conditions have been reported based on those evidences.

Controversially, “wiggles” or sometimes “weak puffs” were noticed even below  $Re_\delta \approx 500$ , depending on the equipments used to measure the velocity fluctuations, and the above number has been cited as a critical value in general (see, for example, [Hino \*et al.\* \(1976\)](#)). The study of [Eckmann & Grotberg \(1991\)](#) reported two occasions of instability by immersing the wire probe at different radial positions. Some researchers stated that a time-dependent wall shear stress can produce a transition signal once it is disturbed, although this behavior may imply the existence of intense turbulence bursts at certain flow conditions, but not necessarily the early stages of transition.

One of the important motivations of this study is to explore in depth the transition to turbulence in the oscillating pipe flow, since there are discrepancies among various approaches regarding the issue of a suitable stability criterion for this type of flow. Fully resolved direct numerical simulations (DNS’s) for the transition in purely oscillating pipe flow were not found, and most of the experiments were not conducted to investigate the stability for a wide range of oscillation frequencies at this stage of transition, where the flow starts to deviate from the laminar flow.

### 3.2 Governing equations

All the computational works presented in this chapter are dedicated for the first stage of transition which is defined herein as a disturbed laminar flow. A fully-developed oscillating flow in a straight circular pipe of the radius,  $R^*$ , and the length,  $10R^*$ , is considered. The flow is solely driven by a sinusoidal pressure gradient,  $(1/\rho^*)\partial p^*/\partial z^* = -\tilde{A}^* e^{i\Omega^* t^*}$ , where  $\tilde{A}^*$  is the oscillation amplitude of the pressure gradient,  $i$  is the unit imaginary

number, and  $\Omega^*$  is the angular frequency. The non-dimensional quantities of the current analysis are obtained by introducing the following parameters:  $\tilde{A} = \tilde{A}^*/(\hat{u}^{*2}/R^*)$ ,  $\tilde{F} = \tilde{F}^*/(\hat{u}^{*2}/\delta^*)$ , and  $z = z^*/\delta^*$ , where  $\tilde{F}^*$  is an axial force. The del operator is nondimensionalized by  $1/\delta^*$ , and after substituting all the relevant scales into the governing equations, the continuity equation and the time-dependent Navier-Stokes equations for an incompressible flow can be written as follows:

$$\nabla \cdot \mathbf{u} = 0, \quad (3.1)$$

$$\frac{1}{\lambda} \frac{\partial \mathbf{u}}{\partial \tau} + (\mathbf{u} \cdot \nabla) \mathbf{u} = -\nabla p + \frac{1}{Re_\delta} \nabla^2 \mathbf{u} + \tilde{\mathbf{F}}, \quad (3.2)$$

where  $\mathbf{u}$  is the dimensionless velocity vector. Instead of applying the pressure forces directly in the current simulations, a body force, which is a driving force per unit mass, is adopted, and its non-dimensional form is written as

$$\tilde{\mathbf{F}} = \tilde{A} e^{i\Omega \tau}. \quad (3.3)$$

### 3.3 Numerical solver

To accurately solve Eqns. (3.1) and (3.2), a high-order spectral element fluid dynamics solver called Nek5000 is employed. There are various applications that used this code for turbulent flows as well as transitional flows (see, for example, [Fischer \*et al.\* \(2002\)](#)). The basis function chosen in Nek5000 is the Legendre polynomial based on Gauss-Lobatto-Legendre (GLL) points for the velocity of order  $5 \leq N \leq 15$  and on Gauss-Legendre quadrature points for the pressure of order  $N-2$ , calculated by Poisson's equation. Note

that  $N$  can be changed as needed, but it was fixed at 7 in this investigation for transitional flows. The temporal discretization of Eqn. (3.2) is semi-implicit in which the viscous terms are solved implicitly with a third-order backward differencing (BDF3) and the non-linear terms are solved explicitly by a third order extrapolation (EXT3). The extrapolation is implemented to avoid the implicit treatment in some of the advection terms, where an iteration of a non-symmetric system is performed. It is known that Nek5000 has the flexibility of the finite element method and the high-order accuracy of spectral method of molding a mesh with locally refined elements. In other words, the technique divides the computational domain into hexahedral elements and collocation points (GLL) distributed inside each element (Deville *et al.* (2002)).

### 3.4 CFD code validation

Since the pipe flow is fully developed in the axial direction, periodic boundary conditions were imposed at the two ends of the pipe. The oscillating driving force was employed and initiated at zero velocity condition to reach the long-time oscillation after several cycles (approximately 16). The velocity profiles with overshoots near the wall at the oscillation condition of  $Re_\delta = 100$  and  $\lambda = 10$  are plotted in Fig. 3.1. In this figure, at five different times during one oscillation cycle, the computed velocity compared with the exact solution of laminar flow (Eqn. (2.22)) is shown in terms of  $\zeta$ . The high accuracy for the 2-D axisymmetric flow being considered is achieved by Nek5000, where the relative errors between the two velocity curves are very small along the radial coordinate at each instant. The accuracy of the solution was also confirmed for the 3-D case, where the numerical results of the three-dimensional simulation were found to be equivalent to those of Fig. 3.1.

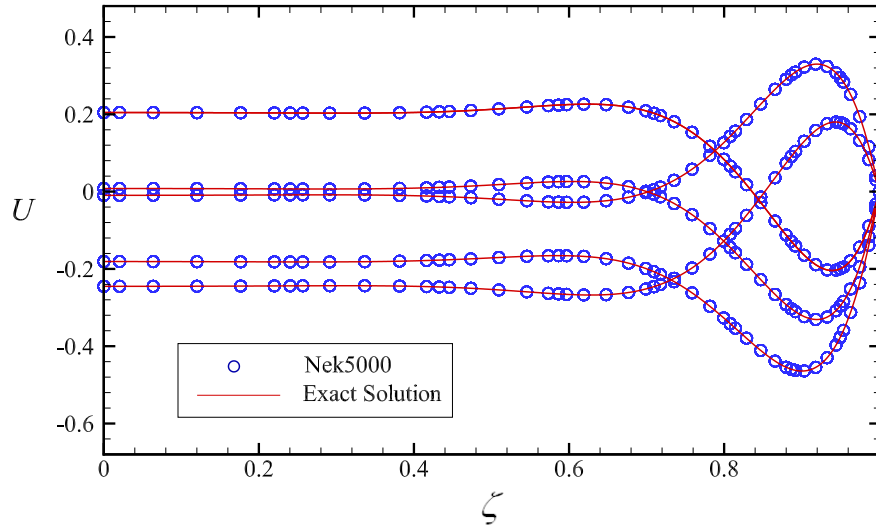


**Figure 3.1:** The laminar velocity at the flow condition of  $Re_\delta = 100$  and  $\lambda = 10$  predicted by Nek5000 using the driving force concept at five different times during a cycle, compared with that of the exact solution of [Sexl \(1930\)](#).

### 3.5 Grid convergence analysis

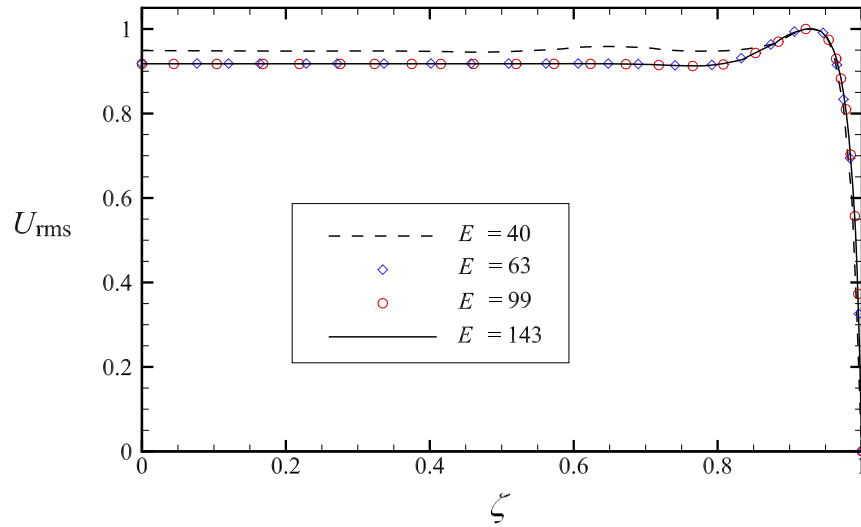
Small random perturbations were superimposed on the exact solution of the laminar velocity to cause instabilities in the flow. This strategy of triggering the flow transition is common in the DNS community, by which the disturbance growth can be investigated in accordance with the linear stability theory. The data statistics of the axial velocity produced by Nek5000 were found to be independent of the initial condition, and it is consistent with the findings of [Zhao \*et al.\* \(2004\)](#) about the effect of perturbations. Therefore, random white noises with the amplitude of  $10^{-4} \times \hat{u}^*$  were imposed, which is close to that of [Singer \*et al.\* \(1989\)](#) that investigated a modulated planar channel flow, where  $\hat{u}^*$  is the velocity amplitude at  $\zeta = 0$ .

The dimension of the geometry used in this chapter is  $0.01 \times 0.1$  ( $m^2$ ) in a two-dimensional axisymmetric plane ( $z$ - $r$  plane). The adequacy of a mesh refinement for this domain was tested at the very beginning stage of transition, where the velocity field starts deviating



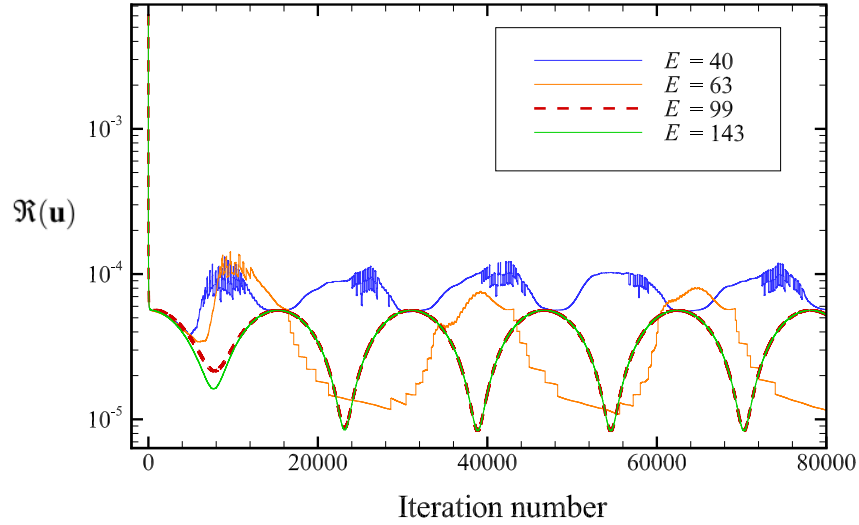
from that of the laminar flow, by increasing the number of elements ( $E$ ) and setting  $N$  to be 7. However, the realizations of the velocity are somewhat sensitive to the initial conditions associated with the mesh resolution, so cycle-averaged statistics (second moments) were chosen as criteria for the grid convergence study. DNS data showed that the velocity of a disturbed laminar flow are symmetrical in the time history of oscillations. Thus, the magnitudes of the cycle-averaged velocity (first moment) can be ignored, i.e., the value of  $\bar{u}$  is nearly zero, and the RMS velocity equation for one complete cycle is  $U_{\text{rms}} = \sqrt{\bar{u}^2}$ .

Figure 3.2 shows the profiles of  $U_{\text{rms}}$  evaluated with four different values of  $E$  and at a fixed polynomial degree. The flow conditions of Fig. 3.2 are chosen slightly above the critical levels so that the velocity is slightly different from the exact laminar flow solution. Note that the total grid points can be calculated from  $EN^2$  for the two-dimensional mesh clustered near the wall, although it is not shown herein. With  $E = 40$ , the flow patterns appear not to be well predicted by the mesh resolution at  $0 \leq \zeta \leq 0.85$  compared with that in the Stokes layer. In contrast, the rest of the meshes with three different grid refinements,  $E = 63, 99$ , and  $143$ , show approximately the same profile of  $U_{\text{rms}}$  at  $0 \leq \zeta \leq 1$ . Also, the relative errors between the RMS velocities decrease with the number of elements,  $E$ , although they are not shown herein. Based on the results of Fig. 3.2, it has been determined that  $E = 99$ , for flow conditions at and near  $Re_\delta = 250$  and  $\lambda = 10$ , is sufficient to resolve the structure of the disturbed laminar flow. The time step is chosen to be variable in this study, and its initial value was set at  $10^{-4}$  sec, with a value of the CFL number equal to 0.05. Note that aliasing errors are minimized when Nek5000 computes the nonlinear terms in the Navier-Stokes equations using over-integration, which is a technique often employed for de-aliasing. In addition, the weight of stabilizing filter, used to stabilize the computation, was controlled at 0.001 for all simulations performed at this level of flow transition.



**Figure 3.2:** The profiles of  $U_{\text{rms}}$  produced by the two-dimensional axisymmetric simulations of the oscillating flows performed at  $Re_\delta = 250$  and  $\lambda = 10$  using four different numbers of elements,  $E$ , and a polynomial degree of  $N = 7$ . The velocity statistics are taken at the mid-plane of the pipe.

Since Nek5000 is an iterative solver, the computational meshes can also be tested using the residual of the velocity vector,  $\mathbf{u}$ , for each time step. Let's consider the approximate solution of Eqns. (3.1) and (3.2) represented by  $\tilde{f}(\mathbf{u})$ , and accordingly the residual can be easily obtained from the following explicit expression:  $\mathfrak{R}(\mathbf{u}) = f(\mathbf{u}) - \tilde{f}(\mathbf{u})$ , where  $\mathfrak{R}$  is a quantitative measure of error between the solution  $\tilde{f}$  and the exact solution  $f$ . To compute such a difference between these solutions for the four presented resolutions in Fig. 3.2, the residuals of the velocity  $\mathbf{u}$  normalized with respect to volume, which is the summation of the computational cells within the whole domain, are shown in Fig. 3.3. This process was implemented implicitly in Nek5000 routines for each cell of the entire mesh.



**Figure 3.3:** The normalized residuals of the velocity vector,  $\mathbf{u}$ , in terms of the number of iterations with the polynomial degree of  $N = 7$ ; two-dimensional axisymmetric simulations at  $Re_\delta = 250$  and  $\lambda = 10$  with four different values of the number of elements,  $E$ .

It is obvious that the velocity residuals of the four elements have some rapid changes within the early stages of simulations, around  $1 \times 10^4$  of time steps. The first mesh of  $E=40$  is clearly insufficient for a solution convergence since its residual is relatively high compared with the others and continues randomly changing even when the number of iterations is up to  $8 \times 10^4$ . Although the errors involved in the computations using  $E = 63$  mesh do not change arbitrarily as seen in  $E = 40$  case, except those during the initial iterations, the results seem to be varied with the resolution. For the high numbers of grid elements,  $E=99$  and  $143$ , the profiles of residual are fairly equivalent, which gives another proof that the mesh with  $E=99$  is adequate for simulations of the transitional flows in both  $r$  and  $z$ -directions.

The three-dimensional mesh employed for the simulations of flow transition is visualized in Fig. 3.4 to highlight some important aspects of the hexahedral spectral elements. Nodes near the wall are distributed according to a function used by Nek5000, as exhibited for one quarter of the cross sectional area in Fig. 3.4 (a). The whole circular pipe of length

$10R^*$  is depicted longitudinally in Fig. 3.4 (b), where periodic boundary conditions are imposed at the ends. The total number of grid points is  $EN^3$  in the three-dimensional domain with  $N = 7$  and  $11 \times 16 \times 9$  elements in the radial, azimuthal, and axial directions, respectively. The presented mesh was utilized for a flow at  $Re_\delta = 200$  and  $\lambda = 20$ , and it was also found suitable for flows with close values of  $Re_\delta$  and a range of oscillation frequencies from  $\lambda = 10$  to 20. It is worth mentioning that the values of  $U_{\text{rms}}$  shown in Fig. 3.2 did not change significantly between the axisymmetric and the three-dimensional simulations at flow conditions of which the first stage of transition begins.

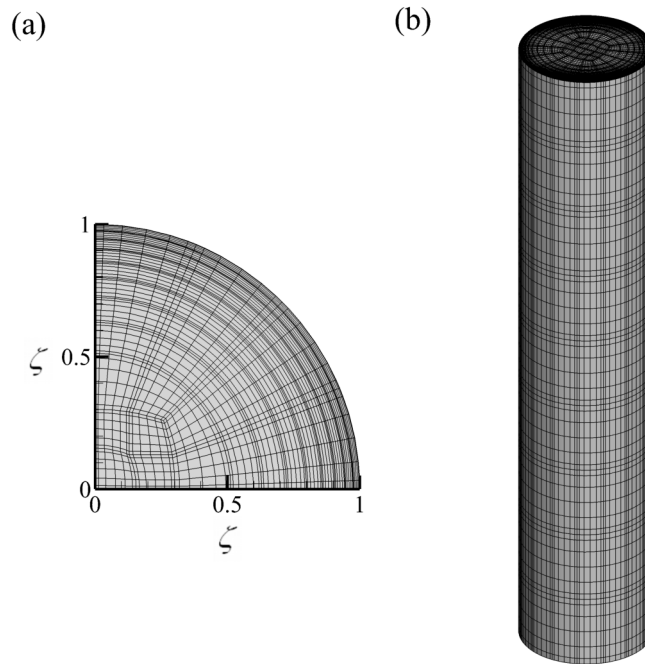


**Figure 3.4:** Computational mesh used for three-dimensional flow simulations at  $Re_\delta = 200$  and  $\lambda = 20$  with the polynomial of degree 7, and the number of elements,  $E$ , are  $11 \times 16 \times 9$  in the radial, azimuthal, and axial direction, respectively: (a) a quarter of a cross-sectional view and (b) the longitudinal view.

### 3.6 Results and Discussions

#### 3.6.1 Critical Reynolds numbers estimated by DNS

In this section, the onset of transition obtained from the linear stability analysis is compared with that predicted by the nonlinear direct numerical simulations at minimum critical values of the Reynolds number. Many 2-D simulations were performed at various Stokes numbers ranging from 3 to 30 to obtain critical Reynolds numbers by perturbing the flow for the initial condition only. These numbers were identified based on the criterion of the disturbed laminar flow, and they are plotted in Fig. 3.5 along with the present theoretical results of the quasi-steady method. Figure 3.5 also shows a collection of critical Reynolds numbers taken from several sources such as theories, numerical studies, and experiments. The flow parameters were converted to  $Re_\delta$  and  $\lambda$  as needed utilizing the following conversion equation:

$$\frac{\hat{u}_{(\zeta=0)}^*}{\hat{u}_{(mean)}^*} = \frac{\left| 1 - \frac{1}{J_0(\alpha\lambda)} \right|}{\left| 1 - \frac{2}{\alpha\lambda} \frac{J_1(\alpha\lambda)}{J_0(\alpha\lambda)} \right|}, \quad (3.4)$$

where  $\alpha = \sqrt{2}e^{\frac{3}{4}\pi i}$  as shown by [Hino \*et al.\* \(1976\)](#), and  $\hat{u}_{(\zeta=0)}^*$  is the velocity amplitude at the axis of symmetry whereas  $\hat{u}_{(mean)}^*$  is the amplitude of cross-sectional mean velocity. The comparison study for this flow transition is intended to prove the validity of the quasi-steady method, whose results are incorporated in Fig. 3.5 to show the differences and/or similarities with others including the present 2-D numerical data. Therefore, Fig. 3.5 presents the transitional values, for which the flow is not expected to experience turbulence bursts. First, all presented data demonstrate the relation between the critical Reynolds number ( $Re_\delta$ ) and the Stokes number ( $\lambda$ ), with approximately similar trends for various flow conditions, but different transition criteria and approaches. The flow at a very

low value of  $\lambda$  behaves almost as a steady Poiseuille flow, and thus the critical Reynolds numbers are high in that region. In contrast, the flow tends to be unstable when the Stokes number increases with relatively low critical Reynolds numbers. Note that it is known the steady Poiseuille flow is stable to all axisymmetric disturbances, which is confirmed at low values of  $\lambda$  in the current results, especially that of the quasi-steady method employing axisymmetric disturbances.

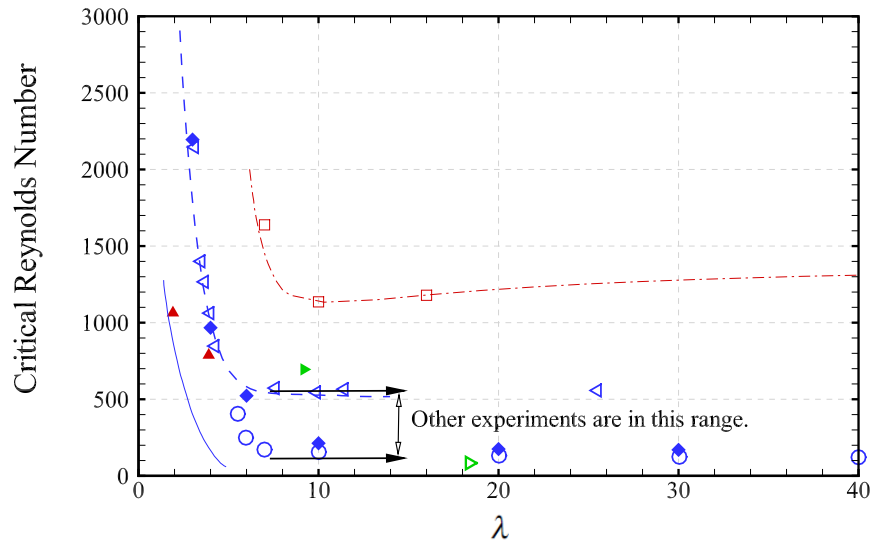


**Figure 3.5:** A comparison of the critical Reynolds numbers: blue solid diamonds — present DNS results (2-D), blue open circles — theoretical results of the present method (quasi-steady), red open squares — Floquet analysis of [Blennerhassett & Bassom \(2006\)](#), red dash-dotted curve — Floquet analysis of [Thomas \*et al.\* \(2012\)](#), blue dashed curve — experiments of [Kurzweg \*et al.\* \(1989\)](#), blue open triangles — experiments of [Lodahl \*et al.\* \(1998\)](#), green solid triangle — turbulent flow (3-D DNS) of [Feldmann & Wagner \(2012\)](#), green open triangle — laminar flow (3-D DNS) of [Feldmann & Wagner \(2012\)](#), red solid triangles — conditionally turbulent flows of [Hino \*et al.\* \(1976\)](#), blue solid line — critical  $Re_\delta$  of weakly turbulent flows of [Hino \*et al.\* \(1976\)](#). The experimental data compiled by [Cooper \*et al.\* \(1993\)](#) for  $\lambda > 7.07$  and those of [Eckmann & Grotberg \(1991\)](#) are located between the two black horizontal arrows.

Secondly, the results of Floquet analyses of [Blennerhassett & Bassom \(2006\)](#) and [Thomas \*et al.\* \(2012\)](#) represented by red open squares and a red dash-dotted line in Fig. 3.5, respectively, indicate distinguished levels of transition. Despite that the study of [Blennerhassett & Bassom \(2006\)](#) considered axisymmetric disturbances only whereas three-

dimensional perturbations were tested in the stability analysis of [Thomas \*et al.\* \(2012\)](#), their analyses yielded approximately the same critical  $Re_\delta$ , except a small deviation appearing at low Stokes numbers. Moreover, since the critical Reynolds numbers of both studies show a considerable amount of discrepancy against all the other data in [Fig. 3.5](#), it is believed that the Floquet method is not able to determine the accurate stability of oscillating flows, where the transient instability occurs within a cycle.

Thirdly, the predictions of the quasi-steady method presented in [Fig. 3.5](#) by blue open circles show the same trends as those of the experimental results (the blue open triangles) of [Lodahl \*et al.\* \(1998\)](#), another experiment (blue dashed curve) of [Kurzweg \*et al.\* \(1989\)](#), and the present two-dimensional DNS results marked with blue solid diamonds. The approximate solutions of the quasi-steady method as well as the DNS results of the current study have critical Reynolds numbers located between the data of the turbulent and laminar flows (the green solid and green open triangles indicating turbulent and laminar flows, respectively) of [Feldmann & Wagner \(2012\)](#). In addition to the two data shown, [Feldmann & Wagner \(2012\)](#) performed another DNS at  $Re_\delta = 4895.23$  with  $\lambda = 3.54$  and found that the flow is turbulent. However, the latter data are not shown in [Fig. 3.5](#) with the presented scale.

The theoretical and numerical results of the current study are both two-dimensional in [Fig. 3.5](#). In this respect, Squire's theorem states that two-dimensional disturbances are sufficient to seek the minimum critical Reynolds number (see, for example, [Drazin & Reid \(1981\)](#)). For the purpose of comparison, three-dimensional DNS's were also performed at two oscillation frequencies and compared with those of 2-D simulations. The critical Reynolds numbers were not pursued in the same way as implemented for the 2-D case, but the lower and upper bounds of those numbers were found and are listed in [Tab. 3.1](#).

**Table 3.1:** Critical Reynolds numbers with respect to the Stokes number estimated by the two and three-dimensional simulations. Only the possible ranges of critical  $Re_\delta$  are shown for the 3-D case at  $\lambda = 10$  and 20.

$\lambda$	DNS (pipe flow)		DNS (channel flow)
	2-D	3-D	2-D
3	2195		
4	967		
6	523		
10	213	210 ~ 225	
20	174	170 ~ 180	225
30	158		160

The effect of the wall shape on the flow stability is examined to confirm that the critical Reynolds numbers of different geometries may be the same when the oscillation frequency of the base flow increases. Additional simulations were performed in 2-D planar channel domains, and the results are combined with those of the circular pipe as shown in Tab. 3.1 for comparison. The height of the 2-D planar channel is equivalent to  $2R^*$ , where  $R^*$  is the radius of the pipe, and the length is  $10R^*$  in the axial direction. Also, the boundary conditions are periodic in the streamwise direction with no-slip conditions at the two channel walls.

The DNS results reveal that the critical Reynolds numbers of the planar channel are higher than those of the pipe at  $\lambda = 20$  and 30. At the lower oscillation frequency,  $\lambda = 20$ , the critical Reynolds number turns out to be 225 for the non-circular duct, indicating that the curvature of the pipe might destabilize the flow at some flow conditions. The difference between the critical Reynolds numbers of the two flows reduces at  $\lambda = 30$  due to the thin boundary layer thickness, i.e., the flow stability becomes more independent of the wall in-



fluence. Thus, it confirms that the critical flow conditions will be almost the same for the flows in the two geometries at high Stokes numbers, higher than 30, in agreement with the statement of [Lodahl \*et al.\* \(1998\)](#), especially at  $\lambda = 53$ .

Regarding the results presented in Tab. 3.1 for the three-dimensional simulations, it is important to mention that, by citing [Stuart \(1987\)](#), [White \(1991\)](#) attributed the maximum wave amplification of the disturbances to the unstable flows owing to a non-zero azimuthal wavenumber. In consequence, the critical  $Re_\delta$  evaluated by the 3-D DNS might have a minor deviation from that predicted by the 2-D simulations. Probably, one possible way of explaining the effect of 3-D disturbances on the flow stability is by the discrepancy between the results shown in Fig. 3.5 for the 2-D and 3-D cases of [Blennerhassett & Bassom \(2006\)](#) and [Thomas \*et al.\* \(2012\)](#), respectively. It should be pointed out that DNS results of the current study become closer to the theoretical counterparts as the Stokes number increases in agreement with some deductions from Eqn. (2.25) of the quasi-steady method, that indicate gaining more accuracy at high values of  $\lambda$ .

Fourthly, the compiled data of [Cooper \*et al.\* \(1993\)](#) show a possible range of critical Reynolds numbers, whose limits are indicated by the two black horizontal arrows in Fig. 3.5. It turns out that the predictions of the quasi-steady approach along with those of present DNS are qualitatively compatible with those compiled by [Cooper \*et al.\* \(1993\)](#) in addition to those produced by [Kurzweg \*et al.\* \(1989\)](#) and [Lodahl \*et al.\* \(1998\)](#). Note that the data points of the latter experiments show a small amount of difference from the highest numbers reported by [Cooper \*et al.\* \(1993\)](#). Also, the discrepancy between the theoretical and numerical data and those of the experiments, especially at large  $\lambda$  (i.e., high oscillation frequencies), is attributed to the role of the base flow velocity of which a small deviation can create a considerable change in the results as described in Chapter 2. Furthermore, for  $10.6 \leq \lambda \leq 23.3$ , the experiment of [Eckmann & Grotberg \(1991\)](#) revealed a nearly constant critical  $Re_\delta$  in agreement with those of [Kurzweg \*et al.\* \(1989\)](#) and another

curve cited by *Cooper et al. (1993)*. The experimental results of *Zhao & Cheng (1996)* were found to be consistent with those of the three papers included in the review study of *Cooper et al. (1993)*. Moreover, the data of *Lodahl et al. (1998)*'s experiment were compared with those of the linear stability theory of *Tromans (1978)* and they showed a good agreement.

The comprehensive study of *Hino et al. (1976)* declared two stages of transition. The first stage is represented by a blue solid line in Fig. 3.5 and stands for the division between the laminar and weakly turbulent flows. The second stage is associated with the two data points depicted by red solid triangles in Fig. 3.5 and refers to the conditionally turbulent flows, at which the turbulence appears only in the deceleration phase. Regarding this stage of transition, *Hino et al. (1976)* stated that the critical  $Re_\delta$  appears to be constant at  $\lambda > 1.6$  based on some experimental indications. Note that *Cooper et al. (1993)* did not include *Hino et al. (1976)*'s data in their table for  $\lambda \geq 7$ , and other researchers disputed *Hino et al. (1976)*'s results by mentioning that the critical  $Re_\delta$  of *Hino et al. (1976)* was underestimated despite the good agreement between their trend and other data shown in Fig. 3.5 at the low values of  $\lambda$ .

### 3.6.2 The onset of transition

The stability of the oscillating flow can be examined by perturbing the flow at a certain Reynolds number and maintaining the Stokes number at one value, herein at  $\lambda = 10$ . It is somewhat consistent with the interpretation of *Das & Arakeri (1998)* regarding the disturbed laminar flows. Further evolutions of these disturbances can lead to turbulence bursts occurring suddenly during the deceleration phase, if the  $Re_\delta$  is sufficiently high. This is in contrast with the idea that the beginning of turbulence bursts in the flow can be detected by tracking the imperfections of the wall shear stress profiles, as determined by *Lodahl et al. (1998)*. Note that some explosive disturbance growths resembling the tur-

bulence bursts may emerge at lower Reynolds numbers than what [Lodahl \*et al.\* \(1998\)](#) reported, as will be shown later in the turbulence chapter.

Due to the sensitivity of the Stokes boundary layer to disturbances, the flow profiles are affected mostly in the near-wall region even though the imposed perturbations are equally distributed in the pipe at  $t^* = 0$ . To show this flow behavior, the velocity curves are plotted at four radial positions in [Fig. 3.6](#) during one cycle at  $\lambda = 10$  and  $Re_\delta = 213$ , which is the current critical Reynolds number listed in [Tab. 3.1](#) for the 2-D simulation. It is noticed that the flow at  $\zeta = 0$  is equivalent to that of the exact solution of [Grace \(1928\)](#) and [Sexl \(1930\)](#) in [Eqn. \(2.22\)](#). On the contrary, the flow experiences low-amplitude waves near the wall region, which continue their appearances for several cycles, although they are shown for one cycle only. The same scenario was observed in [Eckmann & Grotberg \(1991\)](#)'s study, where the growth of disturbances was confined in the Stokes region, whereas the flow was relatively stable near the central axis of the pipe.

The waviness of the velocity profiles shown in [Fig. 3.6](#) is manifested in the decelerating phase, which agrees with many experimental observations (see, for example, [Cooper \*et al.\* \(1993\)](#)). The flow underwent five and a half cycles of oscillation initiated at  $t^* = 0$  to develop a temporally periodic motion after imposing the random noises. Although it is known that the introduced perturbations as an initial condition are necessary to induce transition in a straight smooth pipe, additional simulations were performed with zero initial conditions to confirm it. This is essentially because the objective of this study is to find the critical Reynolds numbers at various flow conditions, and it is possible that the flow undergoes instabilities at a certain level of inertial forces without using any perturbations as will be explained in the turbulence chapter.

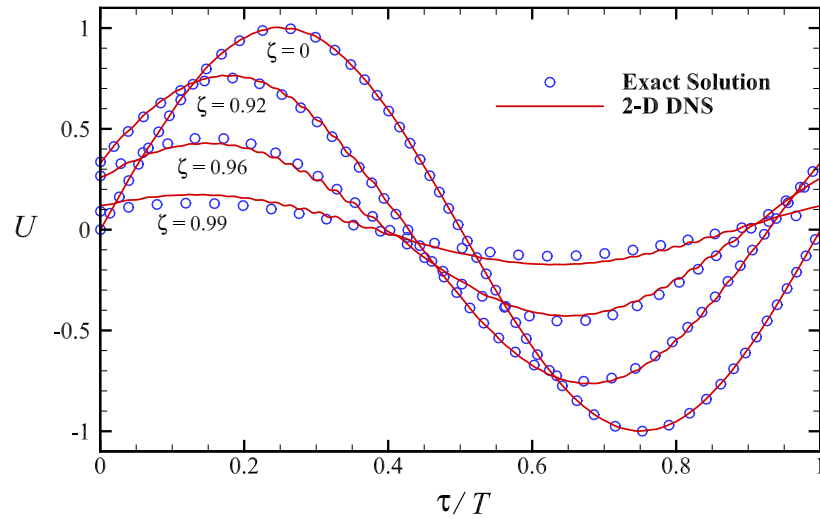


**Figure 3.6:** Time-dependent axial velocity obtained by the two-dimensional axisymmetric DNS at the center plane between the two ends of the pipe and the exact laminar flow solution for the critical condition of  $Re_\delta = 213$  and  $\lambda = 10$  (see Tab. 3.1).

At flow conditions somewhat above the critical levels, the behaviors of the flow in the 2-D axisymmetric and 3-D domains are plotted and shown in Figure 3.7 (a) and (b) for two consecutive cycles. The initial conditions were treated in the same manner as those employed for Fig. 3.6, where the random perturbations are superimposed on the exact solution. Although the waviness in the velocity profiles is different in Fig. 3.7 (a) from those of the 3-D simulations in Fig. 3.7 (b), they can still be found at all the radial positions and mostly during the deceleration phases in both figures. The other components of the velocity were noticed to be very small compared with the axial velocity. The velocity curves are shown for four radial positions, the same as those in Fig. 3.6 and at the same  $\lambda$ . While the near-wall flow is highly disturbed during parts of the oscillation cycle as shown in Fig. 3.7 (b), the flow appears to be stable at the center of the pipe with an exception at the time when the velocity is at its maximum. It should be noted that this type of flow behavior presented in Fig. 3.6 and Fig. 3.7 is not predictable by the Floquet theory since the flow is considered transiently unstable. This means that the instability develops only

during portions of the cycle, and the Floquet exponent will indicate stability or neutral stability as explained for Fig. 2.1.

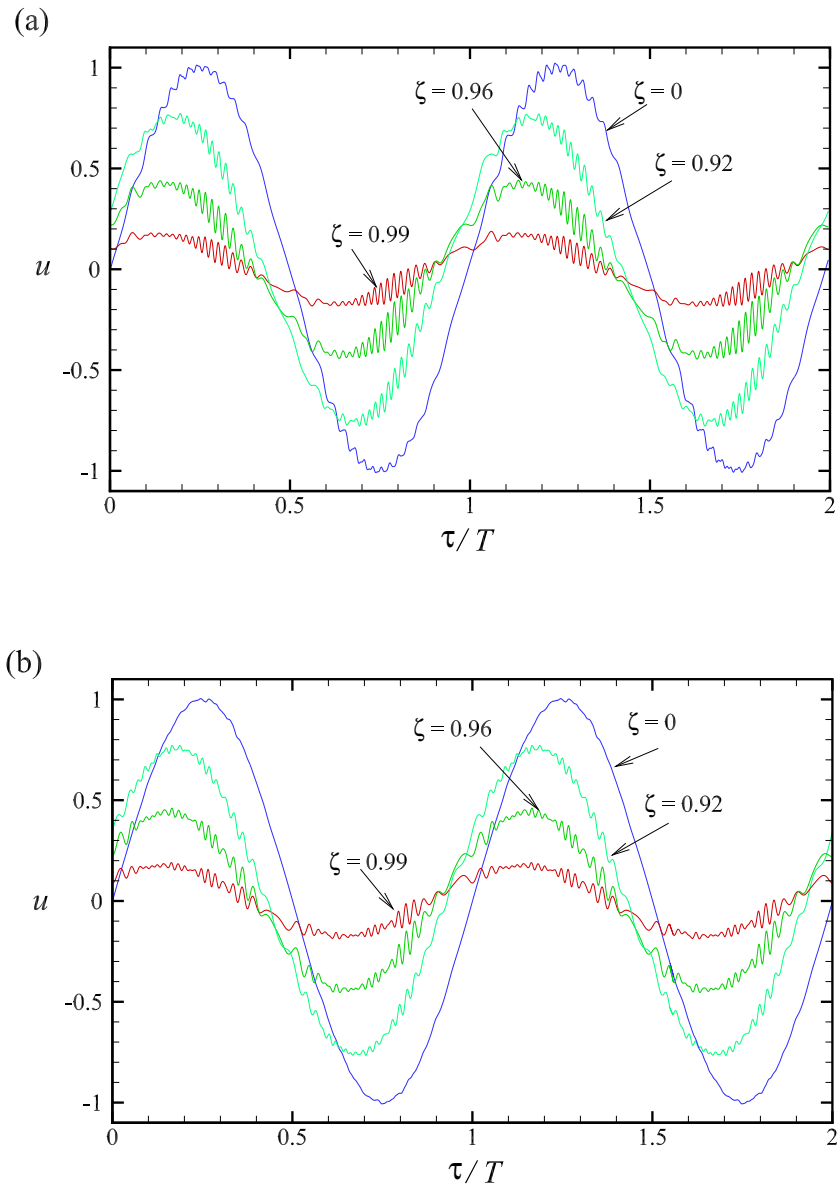


**Figure 3.7:** Time-dependent axial velocities at the center plane between the two ends of the pipe for an unstable flow condition of  $Re_\delta = 250$  and  $\lambda = 10$  by: (a) the two-dimensional axisymmetric DNS and (b) the three-dimensional DNS.

The contour plots of the three-dimensional flow domain, associated with the velocity

curves in Fig. 3.7 (b), are depicted in Fig. 3.8. The sections on the left are the longitudinal planes while those on the right are the cross-sectional views at the middle of the pipe. Figure 3.8 (a) and (b) display the axial velocities captured during the accelerating and decelerating phases at  $\tau/T = 1/8$  and at  $\tau/T = 3/8$ , respectively. As presented in Fig. 3.7 (b), the flow seems to be almost laminar at  $\tau/T = 1/8$ , but the flow structure becomes more complicated, especially near the wall, due to the very weak turbulence at  $\tau/T = 3/8$ . It can be seen that the axial velocity component is positive in the entire domain at both instants of time, meaning that the flow direction is to the right of the longitudinal plane, whereas the other velocity components behave randomly during the whole cycle. Note that the radial and azimuthal components of the velocity illustrated in Fig. 3.8 (c) and (d) at  $\tau/T = 3/8$  have small magnitudes indicating the size of the disturbances, since the base velocities are zero in these directions. The periodic boundary conditions applied to the two ends of the pipe were checked throughout the cycle.

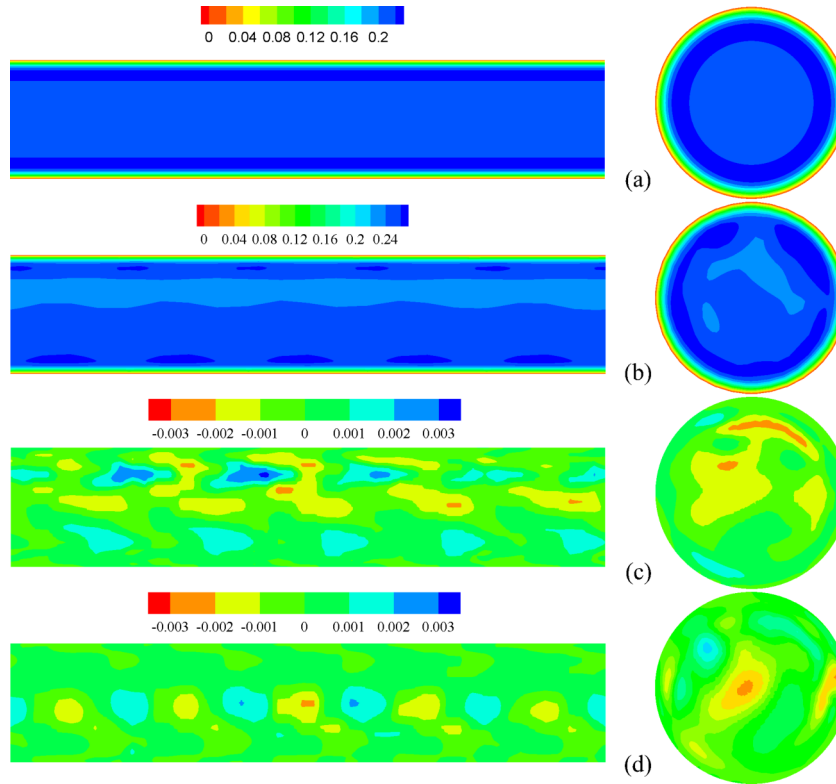


**Figure 3.8:** Longitudinal and cross-sectional contour plots of the three components of velocity (m/s): (a) the axial velocity at  $\tau/T = 1/8$ , (b) the axial velocity at  $\tau/T = 3/8$ , (c) the radial velocity at  $\tau/T = 3/8$ , and (d) the azimuthal velocity at  $\tau/T = 3/8$ . The flow conditions are  $Re_\delta = 250$  and  $\lambda = 10$ .

# Chapter 4

## Turbulence in Purely Oscillating Pipe Flow

### 4.1 Overview

Turbulence generated by an oscillating pressure gradient has a significant role in many engineering fields. For example, one of the coastal engineering problems is the erosion caused by strong waves of turbulent flow hitting the shores. In the reciprocating engines, the mechanism of turbulence production is crucial for the combustion characteristics, chamber design, and intake/exhaust systems. The transitional and turbulent blood flows in some stenosed areas or small branches increase the risk of cardiovascular diseases, as shown by many of the bioengineering studies. The effects of the inertial shear force in oscillating-flow heat exchangers exhibiting high turbulence energy are usually accompanied by a rise in the pressure loss and the heat transfer.

In the literature, there are some difficulties that experiments encounter to accurately predict the initial occurrence of turbulence in the oscillating pipe flows. First, the base ve-



locity distribution in space may not be equally represented in different experiments. For instance, [Hino \*et al.\* \(1976\)](#) attributed most of the discrepancies between different flows experiencing turbulence bursts to the effect of the base flow profile. Second, the onset of turbulence in the radial profiles of flow velocity can be not easily identified by experiments, which require a sustaining turbulence through several oscillation cycles. In this regard, the study of [Lodahl \*et al.\* \(1998\)](#) investigated the initiation of turbulence through the wall shear stress profiles after sampling 50 cycles in the turbulent flow regime. In addition, the experimental devices used to measure the velocity or the pressure can sometimes destabilize the flow via producing finite amplitude perturbations, especially at high Stokes numbers, where the flow is very sensitive to disturbances. Therefore, performing direct numerical simulation (DNS) by means of high-order numerical algorithms is recommended for accurate representations of the base velocity and its derivatives in space and time.

In the DNS community, the numerical schemes that have been extensively employed for the transition and turbulence studies are the spectral and finite volume methods, since the spatial variations of dependent variables are well represented by those techniques in various geometries. The total number of grid points needed for mesh refinement using the finite volume method is 8 times larger than that of the spectral method for the same flow. More importantly, the global basis function of the spectral discretization is based on exponential or orthogonal polynomial eigensolutions; thus, the solution convergence is faster and more reliable than that of the finite volume method. The spectral analysis with a high accuracy is enhanced by incorporating the finite element method in order to reduce the limitations of the mesh modeling.

In this chapter, computations were performed by using Nek5000 at two Reynolds numbers which are  $R_\delta = 400$  and  $800$  with  $\lambda = 10$ . The flow undergoes periodic turbulence and relaminarization (disturbed laminar flows) with different intensities during a cycle

of the long-time oscillations. The profiles of the velocity, wall shear stress, and pressure were produced for two consecutive periods, and the flow was examined considering the amplitudes and frequencies of the fluctuations. Based on the present results, the flow condition of  $Re_\delta = 400$  is found to be somewhat close to the transition stage where the turbulence bursts first appear. The initiation of these bursts was found to vary at relatively high Stokes numbers, in contrast to other studies such as [Lodahl \*et al.\* \(1998\)](#).

## 4.2 Mesh modeling

The accuracy of DNS results is affected by three main factors: the domain size, the maximum grid space, and the time step. First, the size, shape and speed of the largest eddies are determined by the Reynolds number and flow configuration, giving a challenge for DNS to include all the large structures while using a fine mesh for the smaller scales (see, for example, [Coleman & Sandberg \(2010\)](#)). Second, the distance between any two grid nodes should be equal or less than the smallest dissipative scale. Finally, beside that the different length scales of the turbulence are accompanied by a wide range of the time scales, the temporal stability of the spectral method requires the time step to be very small. All these restrictions lead to expensive computations. Therefore, the number of grid points is a central issue for the DNS studies even at low Reynolds numbers, where the optimal number of grid points can be estimated from  $Re_\tau^{9/4}$ , where  $Re_\tau$  is the friction Reynolds number based on the pipe diameter ([Coleman & Sandberg \(2010\)](#)).

Nevertheless, various numbers of grid point denoted by GP in [Tab. 4.1](#) were examined to represent the flow at the conditions of  $Re_\delta = 400$  and 800 with  $\lambda = 10$ . The computational time was reduced since the resolutions listed in [Tab. 4.1](#) were obtained either by increasing  $N$  as for the GP1, GP2, and GP3 meshes or by interpolating the coarse mesh to the finer GP4 mesh. Note that the total numbers shown in [Tab. 4.1](#) were calculated from  $EN^3$

for the three-dimensional domain. In contrast to the disturbed laminar flows, where the exact solution was utilized, the zero value of the velocity was used as an initial condition at the stage where the turbulence bursts are expected to grow. All the mesh independence tests were performed at the same time during computation when the turbulence was developed, and the RMS velocities were examined for the purpose of grid convergence. In addition, because the simulations were performed for several oscillation cycles to investigate the occurrence of turbulence, the post-processing data were exported once the desired resolution was achieved.

**Table 4.1:** The total number of grid points (GP) utilized for the pipe simulations at the flow conditions of  $Re_\delta = 400$  and  $800$  with  $\lambda = 10$ .

Domain ( $L^* = 5 \cdot D^*$ )	$Re_\delta = 400$	$Re_\delta = 800$
GP1	$2.29 \times 10^6$	$4.32 \times 10^6$
GP2	$3.95 \times 10^6$	$7.46 \times 10^6$
GP3	$6.28 \times 10^6$	$11.85 \times 10^6$
GP4	$22.12 \times 10^6$	$43.20 \times 10^6$

A spectral element mesh generator which is the Fortran 90 preprocessing program was used to model the current meshes. The number of elements,  $E$ , was customized with a constant mesh-size increment in both the axial and azimuthal directions, whereas the radial elements were made to be clustered toward the wall. The collocation points of order  $N$  are distributed by the mesh generator inside each element of a domain  $(-1,1)$  in all directions. Figure 4.1 displays a half cylinder of the GP3 computational mesh employed for the flow condition of  $R_\delta = 400$  and  $\lambda = 10$  from two different view angles. Note that the interior penalties of the pipe curvature are located in the place close to the center of the pipe, at  $0 < \zeta < 0.5$ , as shown in Fig. 4.1.

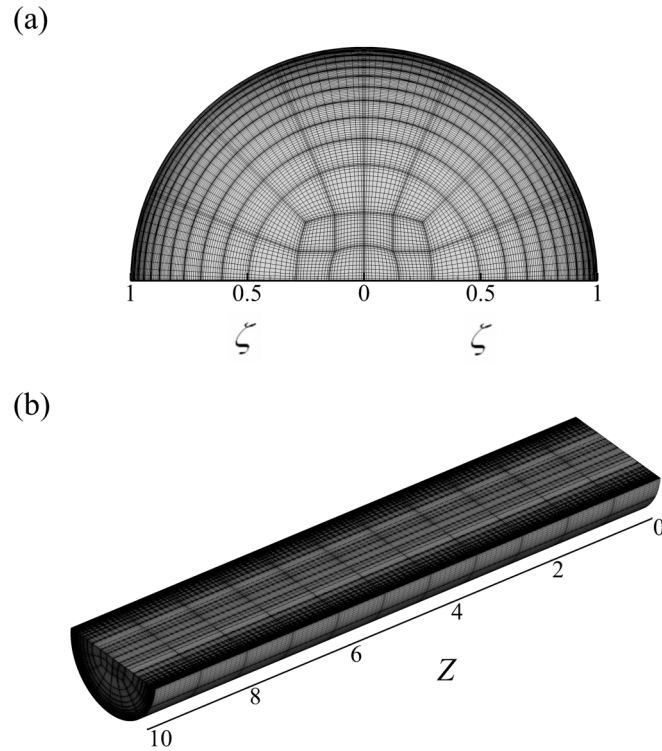


**Figure 4.1:** Computational mesh with the GP3 resolution utilized for the flow condition of  $R_\delta = 400$  and  $\lambda = 10$ : (a) a half of the cross-sectional view and (b) a half of the longitudinal view.

### 4.3 Implementation process

One of the customary methods to perform DNS at a turbulent flow condition is to impose a fully developed turbulence at the inlet of the pipe. In this case, the simulation usually begins at a defined initial condition such as statistically steady turbulent flow, and then the turbulence advances with time accordingly. Another common way is to initiate the simulation with a very high Reynolds number until the flow becomes fully turbulent, and then the flow velocity is reduced to the desired levels. Thus, the turbulence does not evolve from zero initial velocity in the strategies described above in contrast to the current simulations, where the computations start from the rest, since a driving force was applied to create oscillating flows, and the exact solution was not used as an initial condition.

Overall, the onset of turbulence was investigated via two groups of simulation in this thesis. The first is that small random perturbations with an amplitude of  $10^{-4} \times \hat{u}^*$  superimposed on the exact solution of [Sexl \(1930\)](#) were introduced to the flow at  $100 \leq Re_\delta < 400$  and  $\lambda = 10$ . The second group is for  $Re_\delta = 400$  and  $800$ , when the flow evolves from zero initial velocity. For those starting from the laminar solution, simulations of five and a half cycles were sufficient in analyzing the results. For others with  $Re_\delta = 400$  and  $800$ , the number of oscillation cycles was increased to more than 16 to achieve the long-time oscillation of the flow driven by a body force and to produce a solution equivalent to that reported by [Sexl \(1930\)](#). Turbulence associated with sudden bursts took place within the cycles between 20 and 25. Overall, the simulations had to be implemented for more than 25 cycles to obtain the final results, and the data were collected after passing through all those cycles. All levels of grid resolution shown in [Tab. 4.1](#) were investigated after the twenty oscillation regarding the smallest turbulence scales, turbulence statistics, and pipe lengths.

### 4.3.1 Kolmogorov length scale

For the flow being studied herein, the smallest eddies exist during certain phases of the oscillation cycle due to the turbulence and relaminarization phenomenon. Therefore, to satisfy the mesh requirement on the Kolmogorov length scale ( $\Lambda^*$ ) for the present DNS, the maximum grid spaces were compared with the smallest flow scales that appear during the deceleration phase. The rate of dissipation of the turbulent energy per unit mass was obtained for the 25-27th cycles by using the available Nek5000 tools, and the smallest length scale, Kolmogorov ( $\Lambda^*$ ), was calculated from  $(\nu^3/\epsilon_d^*)^{1/4}$ , where  $\epsilon_d^*$  is a time-dependent dissipation rate.

The time variation of Kolmogorov length scale was computed using the GP4 mesh and plotted in [Fig. 4.2](#) for one oscillation cycle. Note that the meshes with the highest reso-

lution for the flow conditions of  $Re_\delta = 400$  and  $800$  were constructed based on the minimum values of  $\Lambda^*$  produced with the GP3 meshes. The smallest Kolmogorov length scale was found to be nearly fixed at  $187 \mu\text{m}$  when the mesh resolution changes for  $Re_\delta = 400$ . However, the results showed a small change, roughly from  $112$  to  $110 \mu\text{m}$ , in the minimum value of Kolmogorov length scale when the mesh was refined for the  $Re_\delta = 800$  flow condition.

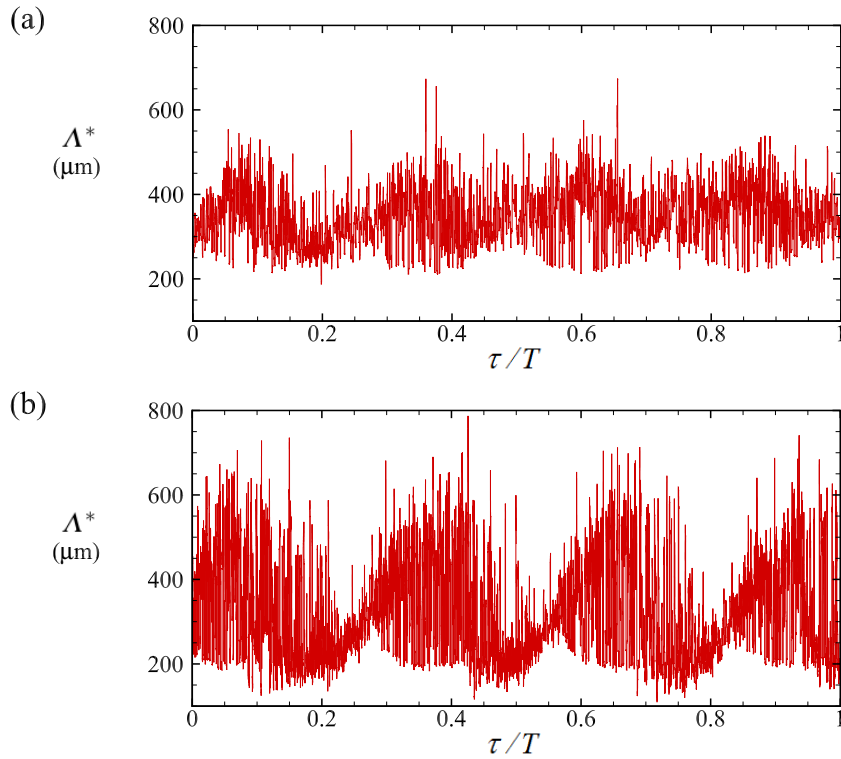


**Figure 4.2:** Kolmogorov length scales in  $\mu\text{m}$  from the simulations with the GP4 mesh resolution at  $\lambda = 10$  and: (a)  $Re_\delta = 400$  and (b)  $Re_\delta = 800$ .

Based on the obtaining values of  $\Lambda^*$ , the maximum grid spaces in the three directions presented in Tab. 4.2 are small enough for the flow condition of  $Re_\delta = 400$ . Although the number of grid points, GP4, for the flow condition of  $Re_\delta = 800$  is almost as twice as that of  $Re_\delta = 400$ , the mesh sizes in both azimuthal and axial directions shown in Tab. 4.2 are slightly larger than the minimum  $\Lambda^*$ . Due to the limited resources such as the number of the available processors, the number of grid points was not increased beyond the GP4

level for the  $Re_\delta = 800$  flow condition. However, the spatial discretizations are considered sufficient regarding the resolution issue compared with other studies, such as [Khoury et al. \(2013\)](#) that utilized the spectral element method for the DNS of statistically steady pipe flow. Moreover, the distance to the nearest wall is the smallest grid spacing in the  $r$ -direction, which is shown for the highest resolution in Tab. 4.2. The time step was chosen to be variable at these two stages of flow condition with an initial value starting with  $10^{-5}$ . The amplitudes of the friction velocity were taken in turbulent regime, and the friction Reynolds numbers were calculated from  $Re_\tau = (\hat{u}_\tau^* D^*) / \nu^*$ .

**Table 4.2:** DNS-database of the flow conditions at  $Re_\delta = 400$  and  $800$  for  $\lambda=10$ .

Domain ( $L^* = 5 \cdot D^*$ )	$Re_\delta = 400$	$Re_\delta = 800$
Total grid points	GP4	GP4
$\Delta r^*, \Delta R^* \theta, \Delta z^*$ (min, max) in $\mu\text{m}$	(4.2, 140), (40, 177), (43, 167)	(3.3, 112), (28, 160), (31, 135)
Kolmogorov length scale ( $\Lambda^*$ ) in $\mu\text{m}$	187	110
Initial time step ( $\Delta t^*$ ) in sec	$10^{-5}$	$10^{-5}$
Maximum friction velocity ( $\hat{u}_\tau^*$ ) in cm/s	1.9	2.5
Friction Reynolds number ( $Re_\tau$ )	385.9	501.2

### 4.3.2 Grid convergence for turbulent flows

Turbulent velocity fluctuations were calculated for one complete cycle between the actual velocity component in the  $z$ -direction ( $u$ ) and its cycle-averaged velocity ( $\bar{u}$ ). Thus, the turbulence statistics in terms of root-mean-square fluctuation velocity ( $u_{\text{rms}}$ ), normalized by  $\hat{u}^*$ , were averaged for a cycle at the turbulent flow condition, and the  $u_{\text{rms}}$  was obtained

from

$$u_{\text{rms}} = \sqrt{\overline{u^2} - \bar{u}^2}. \quad (4.1)$$

Different tests such as the grid convergence, the sufficiency of the domain length, and the time step quantification were implemented depending on the profiles of  $u_{\text{rms}}$ . The results show a good convergence regarding the RMS velocities at the GP3 and GP4 resolutions and the flow condition of  $Re_\delta = 400$  as shown in Fig. 4.3 (a), where the relative errors are negligible. A similar convergence was also noticed for  $u_{\text{rms}}$  at selected locations along the pipe for one complete cycle, i.e., the flow statistics are invariant along the  $z$ -direction, confirming that the turbulent flow is fully developed, or statistically unstationary homogeneous. The turbulence is also checked statistically axisymmetric with quantities exhibiting changes only along the radial direction, although their RMS figures are not shown herein. Furthermore, the mesh with GP3 resolution used for a flow at  $\lambda = 10$  was increased by some percentages to implement computations for flows at  $\lambda = 20$  and 25. The number of elements was rearranged to comply with the flow behaviors near the wall at those high oscillation frequencies, leading also to a good grid refinement.



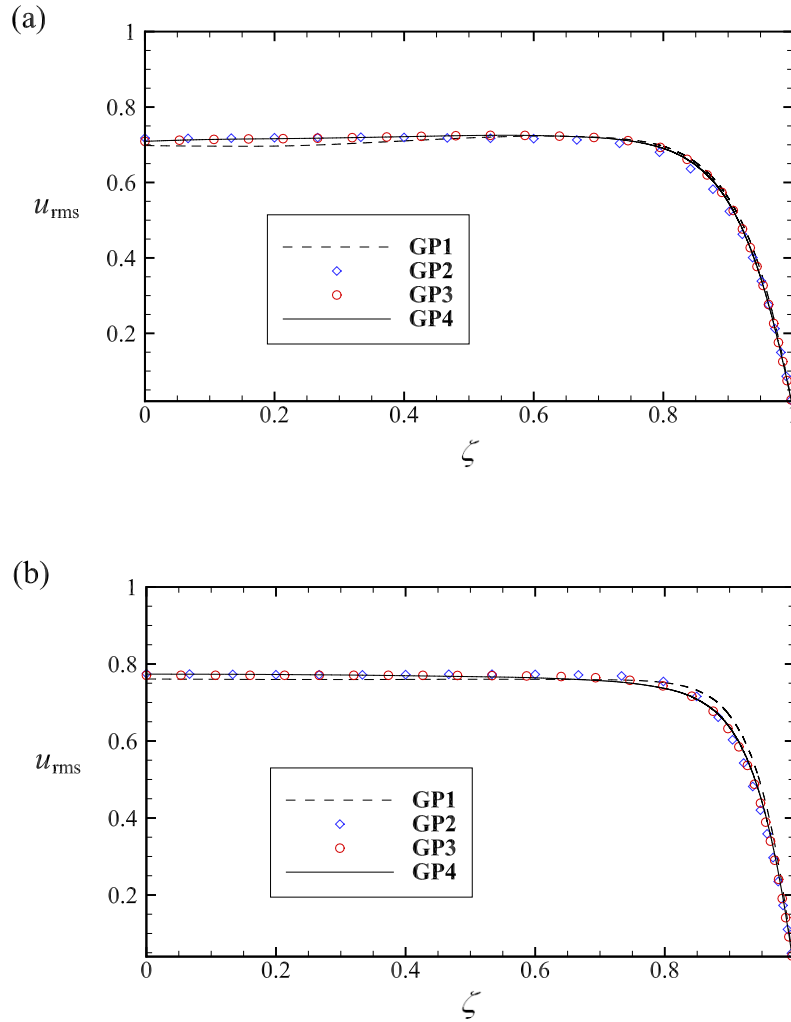


**Figure 4.3:** RMS fluctuation velocities with respect to  $\zeta$ , showing the grid convergence for the simulations performed with the four resolutions at  $\lambda = 10$  and: (a)  $Re_\delta = 400$  and (b)  $Re_\delta = 800$ .

There are small discrepancies between all RMS velocities at  $Re_\delta = 800$  as shown in Fig. 4.3 (b). Increasing the number of grid points improved the convergence of RMS velocities, and the relative errors became very small among them using the GP3 mesh and others with grid points above  $10 \times 10^6$ . Note that the duration at which the RMS velocities are shown in Fig. 4.3 (b) is also for the 25th cycle. The turbulence at several locations of the pipe was examined at this level and found to be statistically homogeneous, and their RMS

values are equivalent to those presented in Fig. 4.3 (b) for the GP3 mesh. The turbulence started impulsively from the rest at  $Re_\delta = 800$  in contrast to that at the lower Reynolds number, where the flow behaved as a disturbed laminar flow at the early oscillations before the turbulence developed. For both flow conditions, the curves of  $u_{\text{rms}}$  were invariant at each flow cycle in the turbulent regime of the long-time oscillation.

### 4.3.3 Grid Resolution in terms of wall units

The sufficiency of the grid resolution for the wall-bounded flows can be verified in terms of the kinematic viscosity and the friction velocity only (see, for example, [Khoury \*et al.\* \(2013\)](#), [Kim \*et al.\* \(1987\)](#), [Spalart \(1988\)](#), [Spalart & Baldwin \(1989\)](#)). Regarding the spectral element method, the recommended limits are  $\Delta r^+ \approx \Delta R\theta^+ \leq 5$  and  $\Delta z^+ \leq 10$ , as reported according to the DNS performed for the steady Poiseuille flows. Nevertheless, for this study, the maximum distance of the mesh is normalized by the friction velocity amplitude,  $(\hat{\tau}_w^*/\rho^*)^{1/2}$  where  $\hat{\tau}_w^*$  is the wall shear stress amplitude. Table 4.3 shows the mesh distances at the GP4 resolution normalized by the viscous lengths for the two cases of turbulence with  $Re_\delta = 400$  and  $800$  at  $\lambda = 10$ . The first grid point from the wall is less than 1, and the first ten points are within  $r^+ \leq 10$ .

**Table 4.3:** 3-D mesh (GP4 resolution) information in terms of wall units for the flow conditions of  $Re_\delta = 400$  and  $800$  with  $\lambda = 10$ .

Reynolds number	$r^+$	$\Delta r^+$ (max)	$\Delta R\theta^+$ (max)	$\Delta z^+$ (max)
$Re_\delta = 400$	0.092	3.08	3.894	3.674
$Re_\delta = 800$	0.105	3.584	5.12	4.32

#### 4.3.4 The length of the computational domain

The driving force was applied to obtain an oscillating flow with periodic conditions at the ends. It is known that this type of periodicity ( $u(0, \tau) = u(L, \tau)$ ) creates unrealistic physical correlations at the ends of the pipe since the conditions are artificial, meaning that they can be interpreted as a Fourier representation of the velocity field. Therefore, a sufficient pipe length, larger at least a few times than the largest structure of turbulent eddies, should be employed. To check the validity of these boundaries, the simulations were performed in different computational domains. Three different lengths,  $3.5 \cdot D^*$ ,  $5 \cdot D^*$ , and  $7 \cdot D^*$  were examined at  $Re_\delta = 800$  and  $\lambda = 10$  only, since the turbulence appears to be well pronounced at this stage. The middle length, which is  $5 \cdot D^*$ , was modeled at the GP3 resolution, and the two other lengths were changed in the number of grid points along the axial direction by some percentages. The RMS velocities of the three lengths were fairly invariant for one complete cycle, and they are similar to that shown in Fig. 4.3 (b) at the GP3 resolution. The pipe with length  $5 \cdot D^*$  is chosen for this study incorporating different flow conditions. On the other hand, the periodicity of the boundaries at the cross-sectional areas was tested in terms of instantaneous velocities as shown in Fig. 4.4 and found to be exactly equivalent.

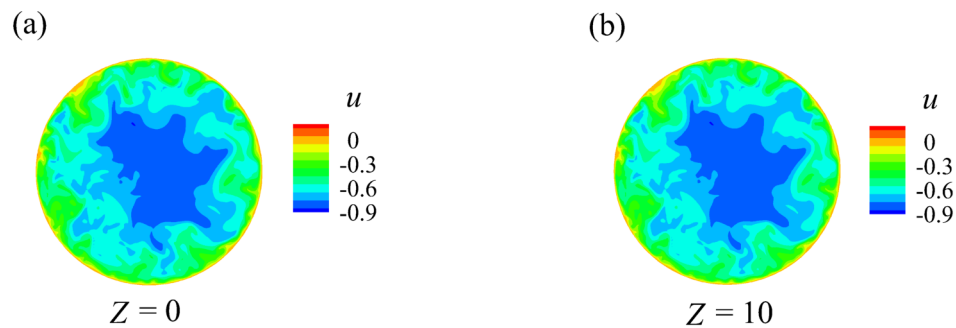


**Figure 4.4:** Instantaneous axial velocities with  $Re_\delta = 800$  and  $\lambda = 10$  at two locations: (a)  $Z = 0$  and (b)  $Z = 10$ , where  $Z = z^*/R^*$ .

#### 4.4 Parallel computing

The high performance scaling properties that Nek5000 offers were utilized for every job assigned to this study. The hardware used for the parallel computing is the Cray CS400 supercomputer cluster running CentOS Linux 7. It is infiniband and connected with 21TB RAM, and it consists of 84 nodes encompassing 36 cores for each node. The computational domain is partitioned linearly over the available cores. To give an example for one simulation performed herein, the number of cores provided for one job was 360 for simulations with  $Re_\delta = 800$  and  $\lambda = 10$ . The wall time per one time step was estimated to be 3.2 sec for simulations with the GP3 mesh resolution, whereas the process consumed 9.5 sec per one time step for the simulations with the highest number of grid points. Regarding the computations with the fine mesh, the number of days was approximately 35 to complete one oscillation cycle in the turbulent regime. Note that the wall time is referred to the actual time spent to execute one job, including the communication time between the parallel CPU's, and it does not account the queue, I/O, and post-processing times.

#### 4.5 Results and discussions

##### 4.5.1 Flow behavior at $Re_\delta = 400$

There are several studies attempting to determine the first appearance of turbulence bursts for the purely oscillating flows. The majority agrees that the turbulence grows in the late time of the acceleration phase and diminishes at the beginning of the flow reversal. The reason why the turbulent structures disappear during the reversal times within the cycle is because of the adverse pressure. In this study, before determining the initial stage of the turbulence bursts, the flow was found to experience periodic waviness during the deceleration phase with relatively low-frequency fluctuations, for flow conditions at  $250 <$

$Re_\delta \leq 400$  and  $\lambda = 10$ . Note that the flow needs an external excitation such as a small random perturbation (or wall roughness as will be explored latter in Chapter 5) to be disturbed when  $Re_\delta \leq 400$ , and after that the turbulence breaks down once the inertial forces become relatively high.

With respect to time, there were no significant variations resembling the turbulence bursts in the profiles of the axial velocity when  $Re_\delta \leq 400$  at all radial positions. However, sudden increases in velocity originating from the near-wall region were noticed during some parts of the two consecutive cycles at the flow conditions of  $Re_\delta = 400$  and  $\lambda = 10$  with  $\zeta = 0.99$  as shown in Figure 4.5. It can be noticed that these structures are not coherent, and they exhibit low-frequency and high-amplitude fluctuations. Note that occurrence of turbulence was tested at this stage for several oscillation cycles, which showed randomly recurrent bursts at the same low intensities.

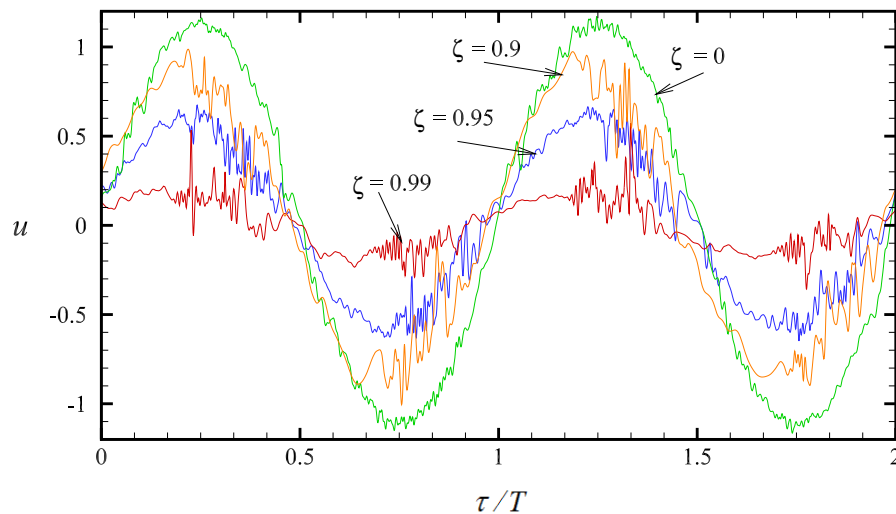


**Figure 4.5:** The temporal evolutions of the axial velocity at different radial positions ( $\zeta = 0, 0.9, 0.95$  and  $0.99$ ) viewed at a cross section midway along the pipe with  $Re_\delta = 400$  and  $\lambda = 10$  and computed using the GP4 mesh.

The total number of grid points at the GP3 resolution was found to be sufficient to simulate a flow with conditions of  $Re_\delta = 400$  and  $\lambda = 10$ , where the turbulence statistics were

approximately constant between the results of GP3 and GP4 meshes. The refinement was increased to make the mesh-size increment less or on order of  $\Lambda^*$ , although fewer grid points could be used at the same RMS velocity. The simulations performed using the fine mesh (GP4) are believed to resolve all relevant turbulence scales, since the maximum grid sizes in any direction are less than  $\Lambda^*$ , as demonstrated in Tab. 4.2.

The computations were implemented for 25 cycles using the GP3 mesh, and the produced data were interpolated to the GP4 mesh as an initial condition. However, the flows experienced a fully developed turbulence between the 25th and 27th cycles in the two domains with those different resolutions by obtaining the time-varying quantities in addition to the averages. The intermittent appearance of turbulence emerges with high amplitudes during the two cycles at  $\zeta = 0.99$  as shown in Fig. 4.5. It can be noticed that the second stage of transition when the turbulence bursts occur appears to be around the flow condition of  $Re_\delta = 400$  as the current DNS data revealed. Due to the various criteria and approaches used by others, the above claim may disagree with previous findings, which considered the  $Re_\delta \geq 500$  flow condition at Stokes numbers from 10 to infinity is the stage of turbulence bursts (see, for example, [Lodahl \*et al.\* \(1998\)](#)).

The critical  $Re_\delta$  at this initial stage of turbulence was not pursued as the way implemented for the disturbed laminar flows. However, the degree of turbulence at three different values of  $\lambda$  which are 10, 20, and 25 was examined with the same  $Re_\delta$ , and the axial velocities at  $\zeta = 0.99$  were produced only. These velocities are shown for two cycles at  $Re_\delta = 400$  in Fig. 4.6. The figure reveals that the turbulence intensity varies with  $\lambda$ , indicating that the turbulence bursts may appear at a lower flow condition than  $Re_\delta = 400$  at high oscillation frequencies, i.e., this stage is not at a constant  $Re_\delta$  as some have declared. Note that the total number of grid points was also increased in order to comply with the new flow conditions.

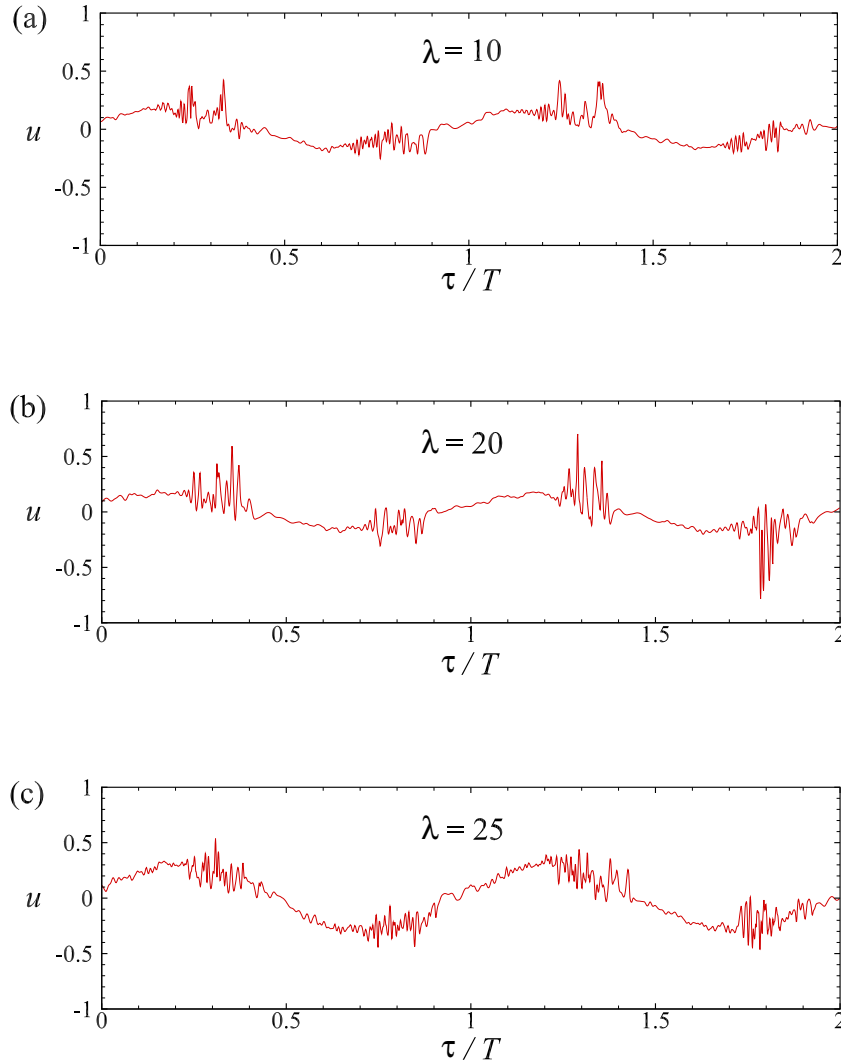


**Figure 4.6:** The temporal evolutions of the axial velocities at one radial position ( $\zeta = 0.99$ ) viewed at a cross section midway along the pipe for three different values of  $\lambda$ : (a) 10, (b) 20 and (c) 25.

The velocity contour plots are presented in Fig. 4.7 (a) and (b) captured during the acceleration and deceleration phases, respectively. In Fig. 4.7 (a), the low-amplitude waviness of the velocity can barely be observed, and the flow appears to be completely laminar. In contrast, turbulent slugs can be identified near the wall as displayed in the Fig. 4.7 (b) with some turbulence amplitudes and frequencies along the pipe. Note that the contour plots are from the simulations employing the GP4 mesh, which produced the time-varying velocities in the middle of the pipe as presented in Fig. 4.5.

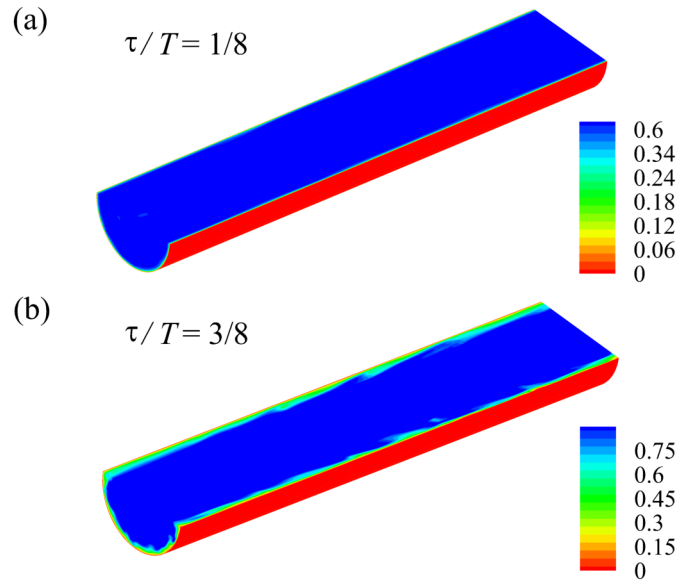


**Figure 4.7:** The contour plots of the axial velocity at  $Re_\delta = 400$  and  $\lambda = 10$  using the GP4 mesh during: (a) the acceleration phase and (b) the deceleration phase.

#### 4.5.2 Flow behavior at $Re_\delta = 800$

Other simulations were performed for the flow condition of  $Re_\delta = 800$  to examine the inertial effects on the flow behavior at one Stokes number ( $\lambda = 10$ ). The initial time step and Courant number were the same as those of  $Re_\delta = 400$ , whereas the total number of grid points was doubled by some ratio, as provided in Tab. 4.2. The maximum mesh distances were reduced in size to be close to the value of  $\Lambda^*$  in all directions. By comparing the two stages of turbulence, the dissimilarities between the two velocity profiles of Fig. 4.8 and Fig. 4.5 are significant, especially in the Stokes boundary layer thickness. The amplitudes and frequencies of the turbulence bursts are more prominent at  $Re_\delta = 800$  than those at  $Re_\delta = 400$ .



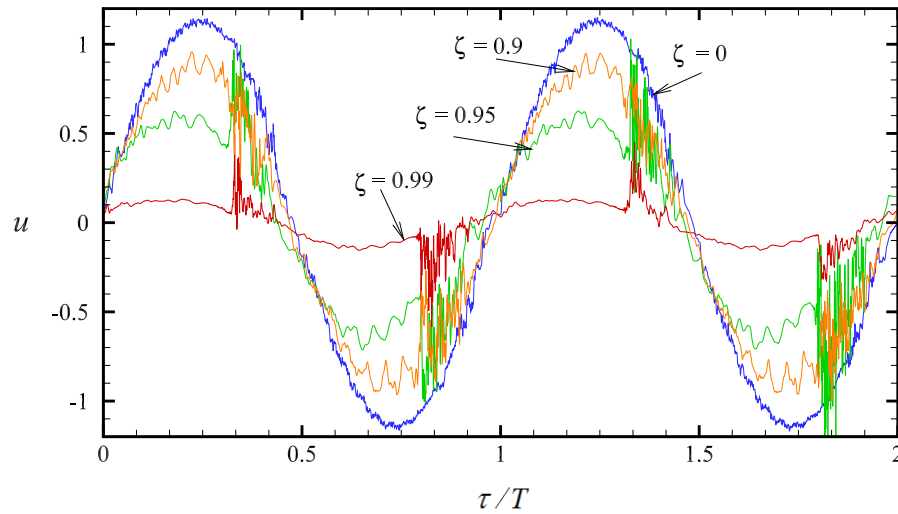


**Figure 4.8:** The temporal evolutions of the axial velocity at different radial positions ( $\zeta = 0, 0.9, 0.95$  and  $0.99$ ) viewed at a cross section midway along the pipe with  $Re_\delta = 800$  and  $\lambda = 10$  and computed using the GP4 mesh..

In addition, the time when the turbulence occurs within the cycle is approximately similar in both cases of the flow conditions. The flow starts with low-frequency fluctuations during the acceleration phase, and then the turbulence bursts grow during the deceleration phase as presented in Fig. 4.5 and Fig. 4.8. The biggest effect of turbulence is noticed at  $\zeta = 0.95$  and  $0.99$  near the wall. The kinetic energy is high in that region, and its maximum value exists approximately in the middle of the deceleration phase. The flow relaminarizes once the flow reversal phase begins, and then the turbulence develops later again until the end of the cycle.

The contour plots along the  $z$ -direction are presented in Fig. 4.9 at two times of an oscillation cycle. The flow is relaminarized at  $\tau/T = 1/8$ , although there are some very small disturbances adjacent to the wall exhibited in Fig. 4.8 at that time. Thus, the visual observations may not reveal the instability of the flow during this phase, and the flow is considered laminar compared with that of the other phases. At  $\tau/T = 3/8$ , the turbulence is more pronounced than that of the corresponding Fig. 4.7, and this degree of turbulence is

expected to be even higher at the same Reynolds number if  $\lambda$  increases.

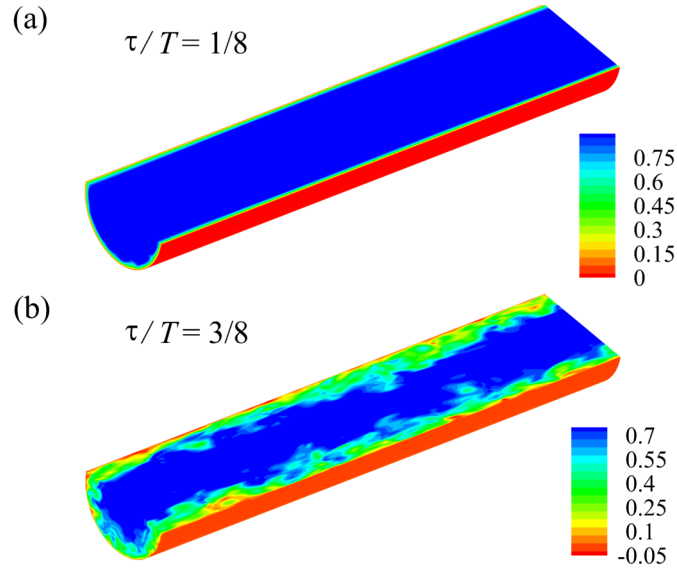


**Figure 4.9:** The contour plots of the axial velocity at  $Re_\delta = 800$  and  $\lambda = 10$  using the GP4 mesh during: (a) the acceleration phase and (b) the deceleration phase.

### 4.5.3 Wall shear stress (WSS)

The fluctuations of the velocity derivative can be detected in the profiles of the wall shear stress. This time-varying quantity was calculated by means of the built-in routines of Nek5000. The accuracy of the computation was believed to be achieved near the wall since the refinements are sufficient in that region for almost all the different numbers of grid point. The analytical solution of the wall shear stress for a viscous laminar flow was calculated from

$$\frac{\tau_w^*}{\rho^*} = \nu^* \frac{du^*}{dr^*}, \quad (4.2)$$

where  $u^*$  is the axial velocity of the exact solution (Sexl (1930)), and its phase was taken according to the phase of the pressure gradient. The DNS results of WSS, which were ex-

tracted for each 100 time steps, are shown for the flows at  $Re_\delta = 400$  and 800 in Fig. 4.10 (a) and (b), respectively. Note that the time periods of the two oscillation cycles shown in Fig. 4.10 are normalized by the time period of the laminar flow.

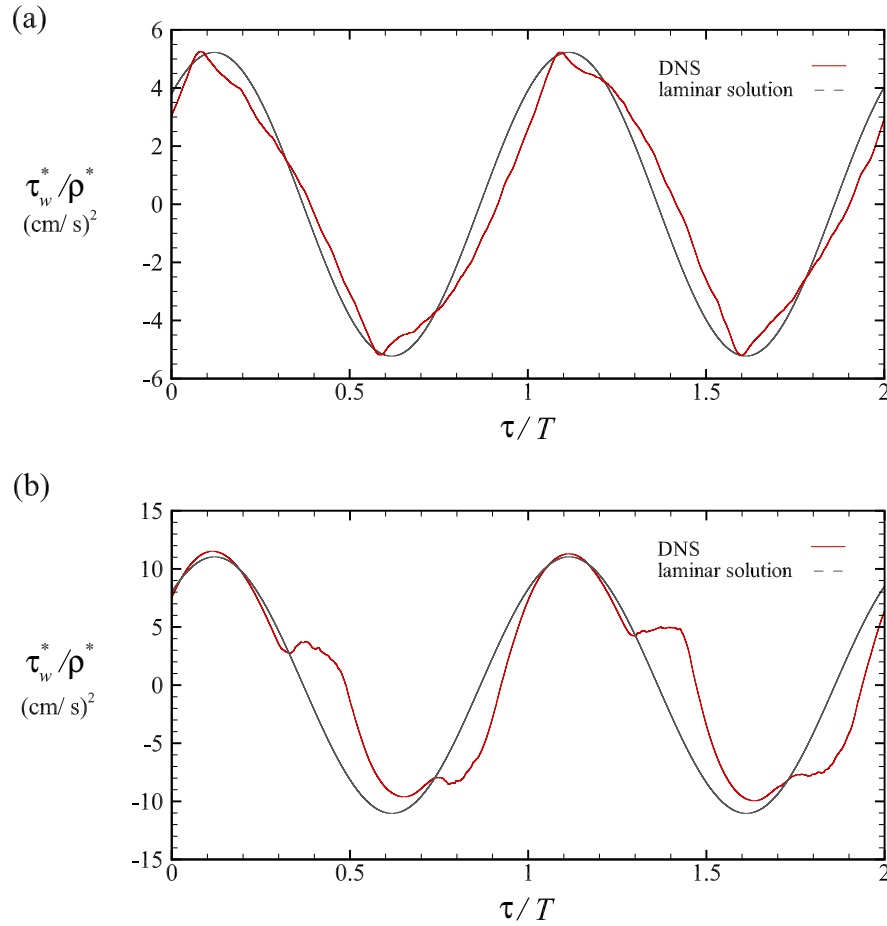


**Figure 4.10:** The time-dependent wall shear stresses at  $\lambda = 10$  and: (a)  $Re_\delta = 400$  and (b)  $Re_\delta = 800$ ; the DNS result (red curve) and the laminar solution (black curve).

Although the flow is periodic with time, an asymmetry may appear in the profiles of the velocity, pressure, and wall shear stress at relatively high flow conditions (see, for example, [Feldmann & Wagner \(2016\)](#)). As can be seen in Fig. 4.10, the signal of the wall shear stress is influenced by this asymmetry making a phase shift or an amplitude change. In this regard, the driving force which is a sinusoidal function leads to periodic oscillations in the pressure gradient. Thus, the temporal periodicity can be identified clearly in the

profiles of the axial velocity as presented in Chapter 3 for the laminar flow. However, the turbulent flow may not necessarily follow this scenario since it is considered as a result of that driving force, being affected by the flow random fluctuations and behaving aperiodically. When the intensity of turbulence increases, the asymmetry becomes more visible; therefore, the influence of this behavior was noticed to be weak at the low flow condition compared with that at the high flow condition.

In addition, the instabilities and chaos are more reflected in the derivatives of the velocity than the velocity itself as explained in the stability analysis. For example, the velocity curve shows slightly asymmetrical waviness during the two cycles presented in Fig. 4.5, leading to small deviations in that of the wall shear stress shown in Fig. 4.10 (a). However, the asymmetry is more ascribed to the velocity curve at  $Re_\delta = 800$  as appeared in Fig. 4.8, especially near the wall ( $\zeta = 0.95$ , and  $0.99$ ), which yields to significant imperfections in the profile of the wall shear stress as noticed in Fig. 4.10 (b), where the turbulent shear stress is apparently aperiodic based on the present DNS results.

Regarding the indication of the initial stage of turbulence, the wall shear stress shows some changes in the magnitudes and phases with respect to those of the laminar solution within the oscillation cycles, particularly during the phases when the turbulence was recorded, and that can be observed in both WSS profiles at  $Re_\delta = 400$  and  $800$ . The WSS differences between the laminar and turbulent flows are clearly shown in Fig. 4.10 (b), where all WSS values of the turbulent flow increase significantly producing strong deflections compared with those of the laminar flow. Additionally, the amplitudes of  $\tau_w^*$  within the two cycles are not equivalent in the case of  $Re_\delta = 800$  in contrast to those of  $Re_\delta = 400$ . Thus, these discrepancies can be attributed to the nature of turbulence since the flow behavior is unpredictable and subjected to the change of the time history of velocity derivative, where each cycle of the oscillation in the turbulent regime is affected by the previous cycle.

At high oscillation frequencies, a comparison was made between the profiles of WSS with three different Stokes numbers for two oscillation cycles as shown in Fig. 4.11. The GP3 mesh was employed for the shear stress computations at  $\lambda = 10$ . Other fine meshes with good refinements near the wall were used for the other flow simulations at  $\lambda = 20$  and 25. The statement claimed for the velocity profiles is confirmed herein, where the intensity of turbulence increases with the oscillation frequency as the wall shear stress profiles reveal. The amplitudes of  $\tau_w^*$  rise significantly with the Stokes numbers at the fixed Reynolds number. The deflection curves of  $\tau_w^*$  are different in shape as shown in Fig. 4.11 (a), (b), and (c) during the phases of deceleration. This is because that the waviness of the velocity derivative increases with  $\lambda$ , and the high turbulence intensity causes a high asymmetry.

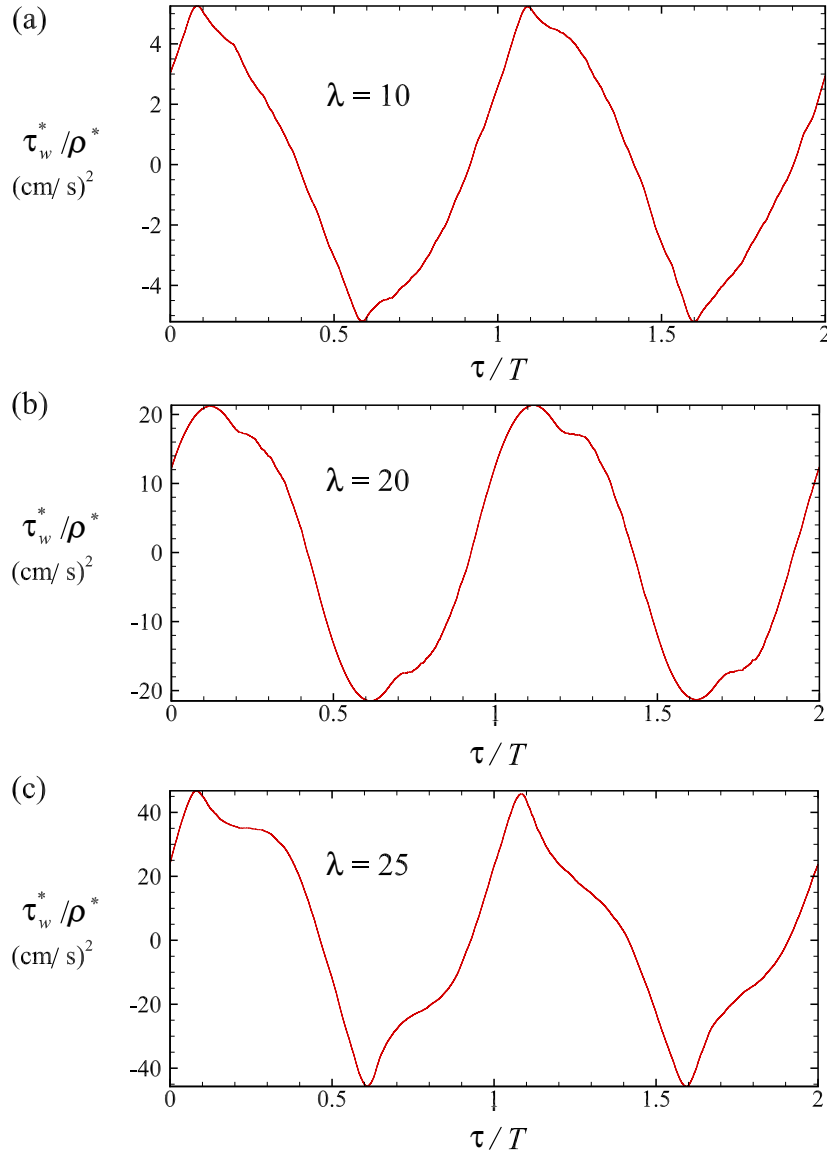


**Figure 4.11:** The profiles of the wall shear stress at flow conditions of  $Re_\delta = 400$  and three Stokes numbers: (a)  $\lambda = 10$ , (b)  $\lambda = 20$ , and (c)  $\lambda = 25$ .

As explained earlier that the oscillating wall shear stress in the turbulent flow regime differs significantly from that of the laminar flow, especially when the flow experiences intense turbulence bursts at high  $\lambda$  such as 53, as that conducted by [Lodahl \*et al.\* \(1998\)](#) in their experimental investigation. For the sake of comparison, the current  $\tau_w^*$  of the smooth pipe flow (blue curve) at  $Re_\delta = 600$  and  $\lambda = 53$  is compared with that of [Lodahl \*et al.\* \(1998\)](#) (red curve) as shown in Fig. 4.12. It appears that the turbulent fluctuations

and their phases are not equivalent between the two curves, but the friction coefficients have shown excellent agreement between them throughout the oscillation cycles as those shown in Fig. 4.12, with more results presented in Chapter 5. Note that, the DNS data were scaled by a factor of 0.0165 since different geometry and flow characteristics were used in the two approaches of analysis at the same Reynolds and Stokes numbers. Also, the time series of the two curves is not simultaneous, where around 25 cycles were implemented in the numerical computations relative to at least 50 cycles sampled in the study of [Lodahl \*et al.\* \(1998\)](#).

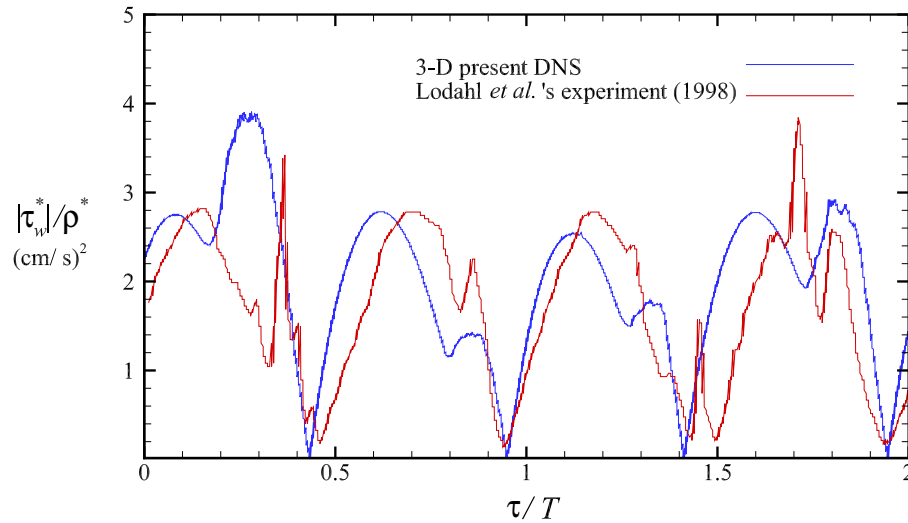


**Figure 4.12:** Experimental validation for the present DNS result in terms of the wall shear stress utilizing [Lodahl \*et al.\* \(1998\)](#)'s data at flow conditions of  $Re_\delta = 600$  and  $\lambda = 53$  (red); the wall shear stress of the present DNS (blue) is scaled by a factor of 0.0165.

#### 4.5.4 Turbulence intensity

The degree of turbulence increases with the flow condition from  $Re_\delta = 400$  to 800 as shown in the previous figures, and it also varies among the radial positions of the pipe. In this regard, the velocity fluctuations can be calculated with respect to the laminar solution,

so that the level of turbulence for any flow condition can be estimated from

$$TI = \frac{\sqrt{(u-U)^2}}{|U|}, \quad (4.3)$$

where the fluctuation of the axial velocity is  $u' = u - U$  in a non-dimensional form, and  $U$  is considered the velocity of the exact solution in Eqn. (2.22).

**Table 4.4:** Turbulence intensity ( $TI$ ) appearing in Eqn. (4.3) at four radial positions for two Reynolds numbers and  $\lambda = 10$ .

$\zeta$	$Re_\delta = 400$	$Re_\delta = 800$
0	0.237	0.249
0.90	0.275	0.350
0.95	0.444	0.665
0.99	0.944	0.967

Table 4.4 demonstrates the values of  $TI$  for flows experience turbulence variously among the probed points. Since the disturbances in the center of the pipe are almost the same for the two flow regimes, the difference between the turbulence intensity at  $Re_\delta = 400$  and that at  $Re_\delta = 800$  in Tab. 4.4 is small at  $\zeta = 0$ . A relatively slight increase occurs in the turbulence intensities at  $\zeta = 0.9$  for both flows with  $Re_\delta = 400$  and  $800$ , respectively. The significant change in the turbulence is at  $\zeta = 0.99$  compared with that at  $\zeta = 0.95$  in the case of  $Re_\delta = 400$  flow condition, with a small difference from that at the condition of  $Re_\delta = 800$ . The turbulence intensity at the two stages of turbulence becomes higher within the very close region from the wall,  $\zeta = 0.99$ , than those at other locations.



#### 4.5.5 Turbulence kinetic energy (TKE)

In the wall-bounded shear flows, the process of transferring energy from the large to small eddies at the Kolmogorov scales plays the main role in sustaining turbulence. This energy was calculated for the oscillating turbulent flows at the two Reynolds numbers and  $\lambda = 10$ . The RMS fluctuation velocities of the three velocity components were calculated for one oscillation cycle using Equ. 4.1. The TKE per unit mass is defined to be half the sum of the square of RMS velocities of the velocity components as follows:

$$\text{TKE} = \frac{1}{2}(u_{\text{rms}}^2 + v_{\text{rms}}^2 + w_{\text{rms}}^2), \quad (4.4)$$

where  $u_{\text{rms}}$ ,  $v_{\text{rms}}$  and  $w_{\text{rms}}$  are RMS velocities in the axial, radial and azimuthal directions, respectively. Figure 4.13 demonstrates the profiles of TKE with respect to the radial coordinate during the 25th oscillation cycle. The turbulence energy at  $Re_\delta = 800$  is clearly higher than that at  $Re_\delta = 400$ , especially in the center of the pipe. Through the profiles of TKE in Fig. 4.13, the mechanism at which the flow transfers most of its energy from the core ( $\zeta = 0$ ) with large flow scales to the boundary layer region ( $\zeta = 0.99$ ) can be described.

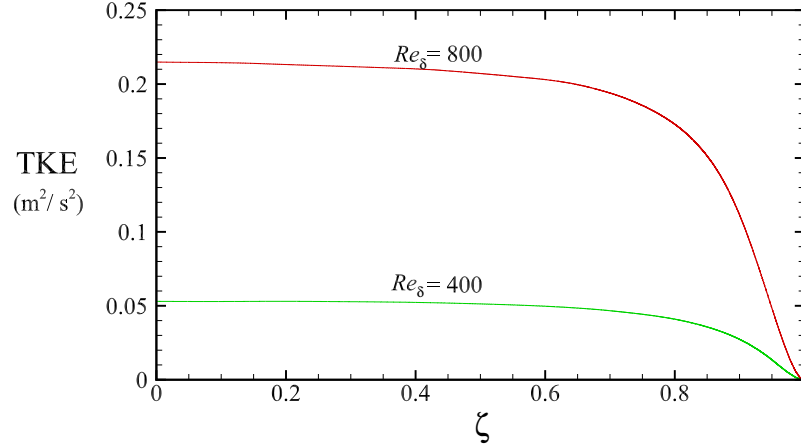


**Figure 4.13:** Turbulence kinetic energy per unit mass computed at the two flow conditions of  $Re_\delta = 400$  and  $800$  for  $\lambda = 10$ .

#### 4.5.6 Spatial autocorrelation function

Spatial correlations between the random fluctuations of any turbulent signal can reveal some important features of the homogeneous turbulent flow. Mathematically, these functions if found are not linked to the Navier-Stokes equations, instead they can be computed from the provided turbulence information, herein the 3-D DNS data at  $Re_\delta = 800$  and  $\lambda = 10$ . Thus, the time-averaged longitudinal autocorrelation function can be written as

$$\bar{R}_{zz}(l, \zeta) = \frac{\overline{u'(Z_0 + l, \zeta, \tau) \cdot u'(Z_0, \zeta, \tau)}}{(\overline{u'(Z_0, \zeta, \tau)})^2}, \quad (4.5)$$

where  $Z_0$  is the reference point for any axial distance in the flow field such as  $l$ . This point was taken in the middle of the pipe,  $Z = 5$ , where  $Z = z^*/R^*$ , and for two radial positions,  $\zeta = 0$  and  $0.9$ . The discrete data of the specified distance, represented under the overbar in Eqn. (4.5), are averaged in time for three intervals at the AP (acceleration phase), DP (deceleration phase), and LD (late deceleration phase). Note that the sampling duration for time averages is from  $\pi/6$  to  $2\pi/6$  during the acceleration phase,  $4\pi/6$  to  $5\pi/6$  during

the deceleration phase, and  $5\pi/6$  to  $\pi$  during the late deceleration phase of the oscillation cycle with length  $2\pi$ .

The eddies with relatively large spatial scales are correlated to that at the reference point during the acceleration phase, when the flow is relaminarized, more than other phases as shown in Fig. 4.14. In contrast, the eddies of the turbulent flow differ in sizes so that those at the smallest scales with respect to the larger eddies are not well correlated to the eddy at the reference point. However, this behavior may not be seen clearly in Fig. 4.14 (a) since the flow experiences low-amplitude fluctuations at  $\zeta = 0$  during the deceleration phase, which are not different from those in the acceleration phase. Moreover, the turbulence scales before the flow reversal at  $\zeta = 0$  with different sizes, are slightly more decorrelated to the eddy at the reference point than those during AP and DP phases.

Since the turbulence intensity increases at  $\zeta = 0.9$  with more random fluctuations, low values of the spatial correlation function were obtained from the various flow eddies near the wall, as shown in Fig. 4.14 (b) and (c), where the last figure is for magnifying the behaviors of  $\bar{R}_{zz}$  near the reference point. The values of  $\bar{R}_{zz}$  in Fig. 4.14 for the flow field during the acceleration phase at  $\zeta = 0$  and 0.9 are approximately the same, due to the nature of disturbances in that phase, where the flow patterns tend to be quite correlated to each other within the half pipe. In contrast to the deceleration phase where turbulence bursts emerge, the flow exhibits eddies of different length scales in the late deceleration phase, so that the profiles of  $\bar{R}_{zz}$  are different along the radial direction, showing a big discrepancy of  $\bar{R}_{zz}$  at  $\zeta = 0.9$  than that at  $\zeta = 0$ .

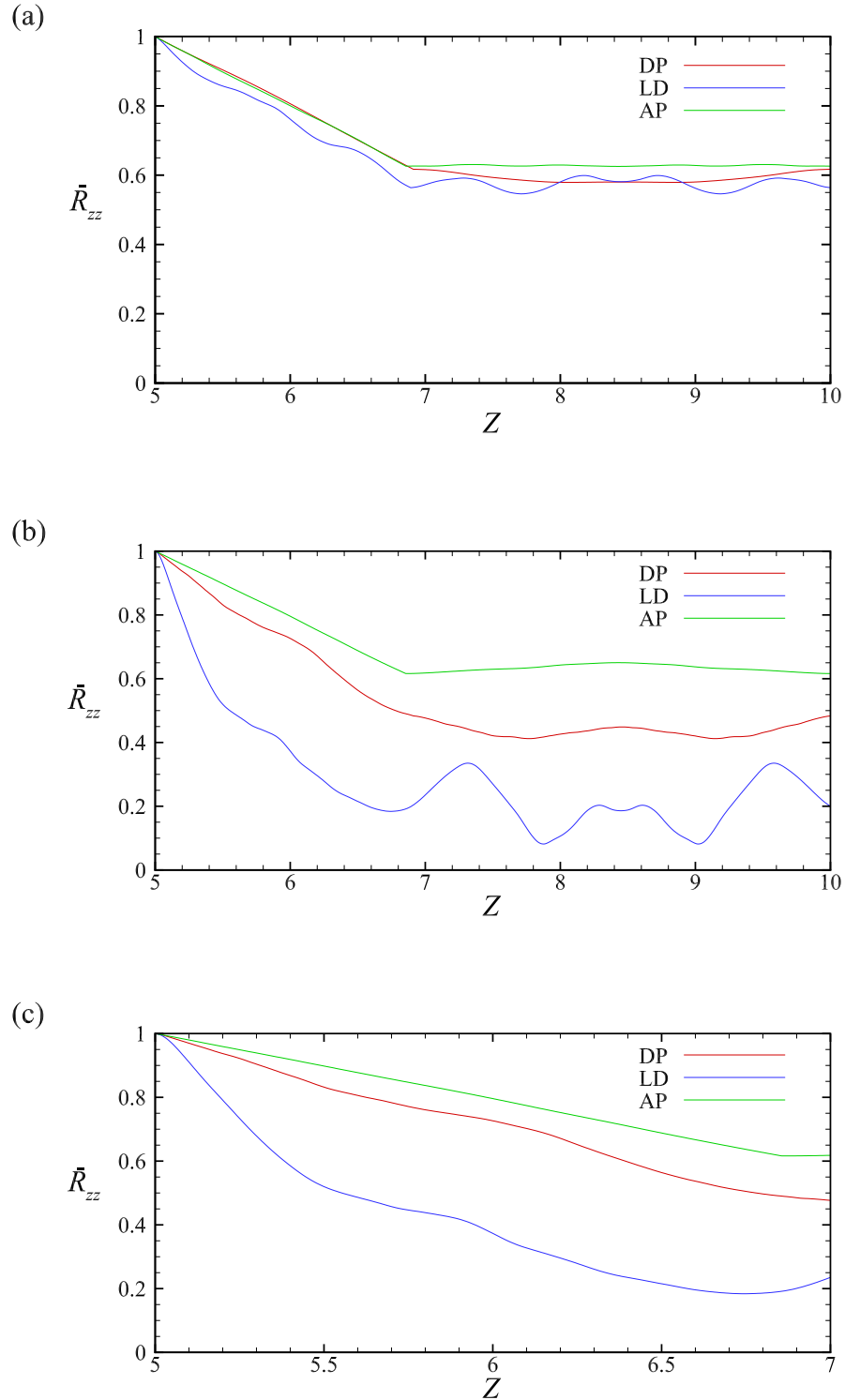


**Figure 4.14:** Spatial autocorrelation functions for a turbulent signal taken along the  $z$ -direction from  $Z = 5$  to 10 at: (a)  $\zeta = 0$ , (b)  $\zeta = 0.9$  and (c)  $\zeta = 0.9$ ; the flow conditions are  $Re_\delta = 800$  and  $\lambda = 10$  for the time-averaged quantities of three intervals at: acceleration phase (AP), deceleration phase (DP) and late deceleration phase (LD).

It is known that  $\bar{R}_{zz}$  does not change with the cross-stream direction, due to the azimuthal periodicity inside the pipe, so that the values shown in Fig. 4.14 are considered sufficient to find the two-point correlations for different values of  $l$ . However, for the unsteady flow, the fluctuation velocity is calculated after subtracting the velocity  $u$  from the that of the laminar flow,  $U$ , meaning that most of the fluctuations are not about zero. Hence, the three curves shown in Fig. 4.14 are not reaching zero in any case, although the turbulence may contain all the relevant motion scales including the integral length scales. Note that if the assumptions of Fig. 4.14 are considered, the integral length scale representing the area under each curve in Fig. 4.14 is  $\int_0^\infty \bar{R}_{zz}(l, 0) dl$ .

#### 4.5.7 One-dimensional energy spectra

The distribution of the kinetic energy among eddies of different sizes can be studied through the behavior of the energy spectrum, which is defined to be the twice of the one-dimensional Fourier transform of the velocity fluctuations as follows:

$$\bar{E}_{zz}^*(k^*, r^*) = \frac{1}{\pi} \int_{-\infty}^{\infty} \overline{u^{*l}(z_0^* + l^*, r^*, t^*) \cdot u^{*l}(z_0^*, r^*, t^*)} \cdot e^{-ik^*l^*} dl^*. \quad (4.6)$$

The discrete Fourier transform (DFT) for a vector  $u_n^{*l}$  of an order of  $N_e$  and a wavenumber of  $k^*$  is defined as

$$\hat{u}_n^{*l}(k^*, r^*) = \frac{1}{N_e} \sum_{n=0}^{N_e-1} \overline{u_n^{*l}(z_n^*, r^*, t^*)} \cdot e^{-\frac{2\pi i}{N_e} k^* n} \quad \text{for } n = 0, \dots, N_e - 1, \quad (4.7)$$

where  $i$  is the imaginary unit. The time-averaged energy spectrum function in terms of  $k^*$

and a radial distance ( $r^*$ ) is

$$\bar{E}_{zz}^*(k^*, r^*) = |\hat{u}_n^*(k^*, r^*)|^2 \quad \text{for } k^* = 0, \dots, \frac{N_e}{2}. \quad (4.8)$$

Following the second hypothesis of Kolmogorov, the energy spectrum of  $-5/3$  slop can be used as a criterion for the DNS data of  $\bar{E}_{zz}^*(k^*)$ , particularly in the inertial subrange of the flow length scales. Figure 4.15 shows nondimensionalized quantities of  $\bar{E}_{zz}^*$  which are scaled by  $(\bar{\epsilon}_d^*(\nu^*)^5)^{1/4}$ , where  $\bar{\epsilon}_d^*$  is the time-averaged dissipation rate, and  $\nu^*$  is the kinematic viscosity. Likewise, the wavenumber  $k^*$  is scaled by the inverse of the time-averaged Kolmogorov length scale ( $\bar{\Lambda}^*$ ). Note that the DNS data were interpolated on the equispaced grid along the axial direction parallel to the axis of symmetry. Also, the three time intervals were taken in the same way implemented for  $\bar{R}_{zz}$ , where the half cycle was divided into six time divisions.

The turbulent signals of the in-line velocities along the  $z$ -direction at two radial positions were considered, and the time-averaged values of  $\bar{E}_{zz}$  were calculated and are plotted in Fig. 4.15 for the three phases of oscillation. It can be seen that the maximum energy spectrum of turbulence occurs during the deceleration phase at both  $\zeta = 0$  and  $0.9$ . The eddies move with relatively low turbulence energies inside the pipe during the acceleration phase at the two probed locations according to the plots of Fig. 4.15. Note that the energy distribution occurring among the largest eddies or those at the Kolmogorov microscales can not be seen clearly in Fig. 4.15. However, the slop in the energy profiles of the inertial subrange eddies is almost equal to  $-5/3$ , especially for the flows with the high turbulence intensities.

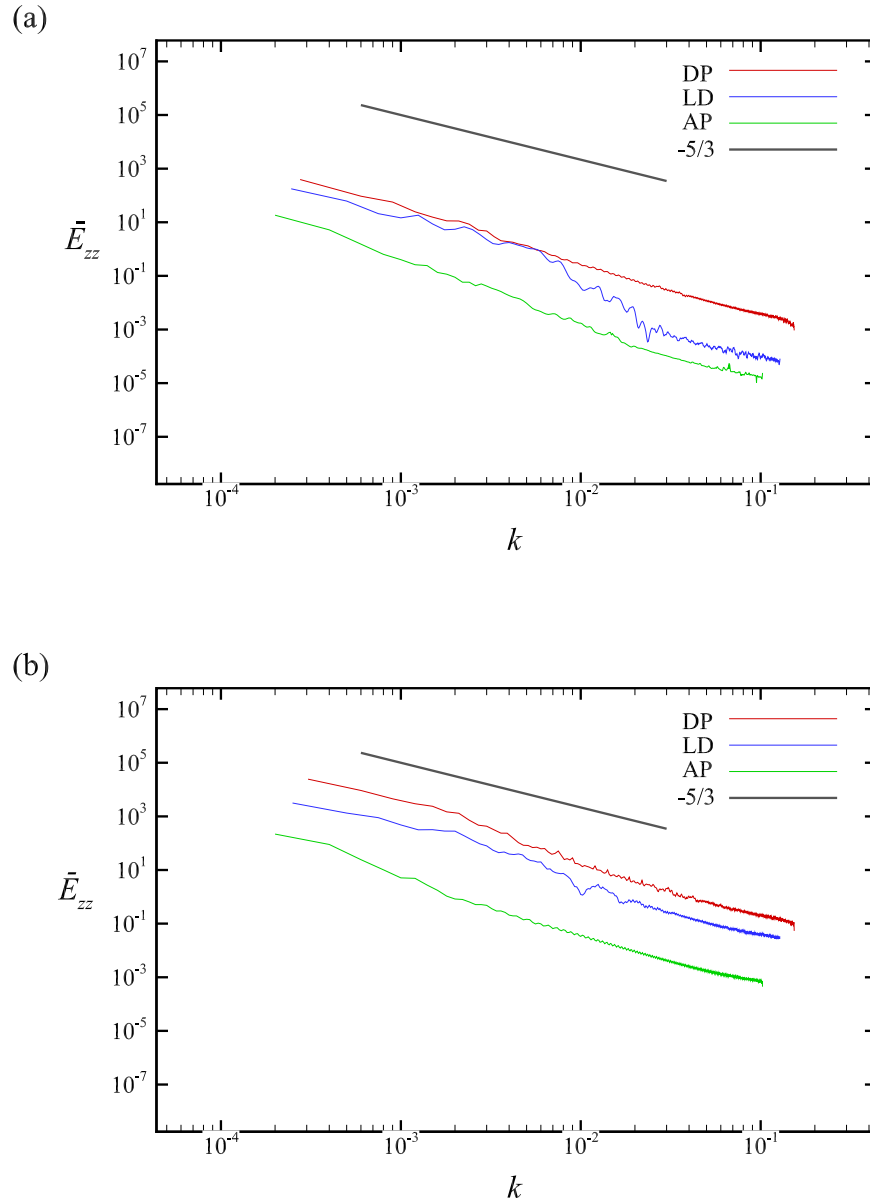


**Figure 4.15:** Energy spectrum of a turbulent signal along the  $z$ -direction from  $Z = 5$  to  $10$  at: (a)  $\zeta = 0$  and (b)  $\zeta = 0.9$ ; the flow conditions are  $Re_\delta = 800$  and  $\lambda = 10$  for the time-averaged quantities of three intervals at: acceleration phase (AP), deceleration phase (DP) and late deceleration phase (LD).

The coherent structure of turbulence cannot be easily sustained during the late deceleration phase since the relaminarization starts to take place. As a result, the trends of  $\bar{E}_{zz}$  in the late deceleration phase are a little different from those of other shown phases at both

radial positions, where the amount of  $\bar{E}_{zz}$  changes significantly at the middle wave numbers as demonstrated in Fig. 4.15 (a). However, the presented values are still higher than the those of the acceleration phase in the two figures. In comparison with those at  $\zeta = 0$ , it is clear that the amounts of energy are increased by some percentages since the level of turbulence is high in the Stokes layer during almost all the oscillation phases. The mechanism for transferring energy at  $\zeta = 0.9$  tends to be similar to that at  $\zeta = 0$  with respect to their slopes.

#### 4.5.8 Vortices in the turbulent flow

The effect of the vortical structures on the oscillating flows was found to be significant since the successively increasing and decreasing magnitudes of the velocity can enhance such vortexes. Figure 4.16 (a) and (b) show the time-averaged vortices during short intervals of the acceleration and deceleration phases, respectively. There are some swirls with small magnitudes when the flow accelerates, which indicate that the turbulence activity is low throughout this part of oscillation in contrast to that of the deceleration phase.

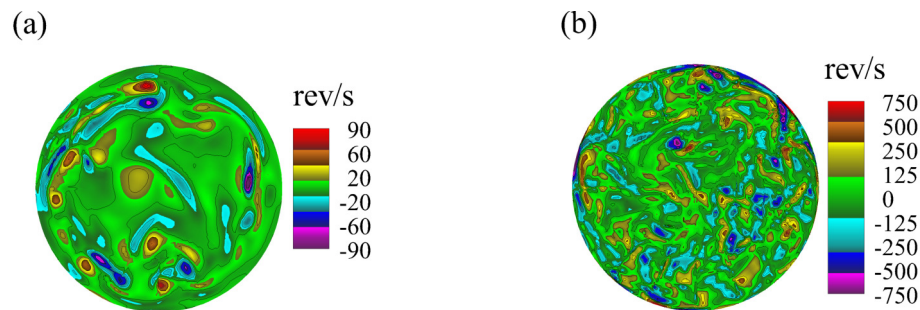


**Figure 4.16:** The time-averaged axial vortices (rev/s) at the flow conditions of  $Re_\delta = 800$  and  $\lambda = 10$  for two intervals of the: (a) the acceleration phase (AP) and (b) the deceleration phase (DP).



#### 4.5.9 Velocity profiles in terms of wall units

In the inner layer, the time-averaged velocities for short intervals of the acceleration, deceleration, and flow reversal phases were obtained and are displayed in Fig. 4.17. The vertical values represent

$$\bar{u}^+ = \frac{\bar{u}^*}{\hat{u}_\tau^*}, \quad (4.9)$$

and the horizontal variable is

$$r_w^+ = (R^* - r^*) \left( \frac{\hat{u}_\tau^*}{v^*} \right), \quad (4.10)$$

where  $\hat{u}_\tau^*$  is the amplitude of the friction velocity. The viscous sublayer at  $r_w^+ < 5$  is the same for all the flows with different phases, although that averaged during the reversal time has a negative sign. These behaviors at the high flow conditions of  $Re_\delta = 800$  and  $\lambda = 10$  are consistent with the  $\bar{u}^+ = r_w^+$  prediction. The divergences among the velocity curves start to increase within the buffer layer at  $5 < r_w^+ < 30$ , especially for the flow which is in the laminar regime. The discrepancy during the acceleration and flow reversal phases between the velocity profiles and that of the logarithmic law of the wall,  $(1/0.41)\ln(r_w^+) + 5$ , is more manifested at  $r_w^+ > 30$  in comparison to that of the deceleration phase, where an excellent agreement is achieved. This gives an indication that the flow during the deceleration phase or at a turbulence condition has the same tendency as that of the steady base flow in the near-wall region due to the high viscous effects.

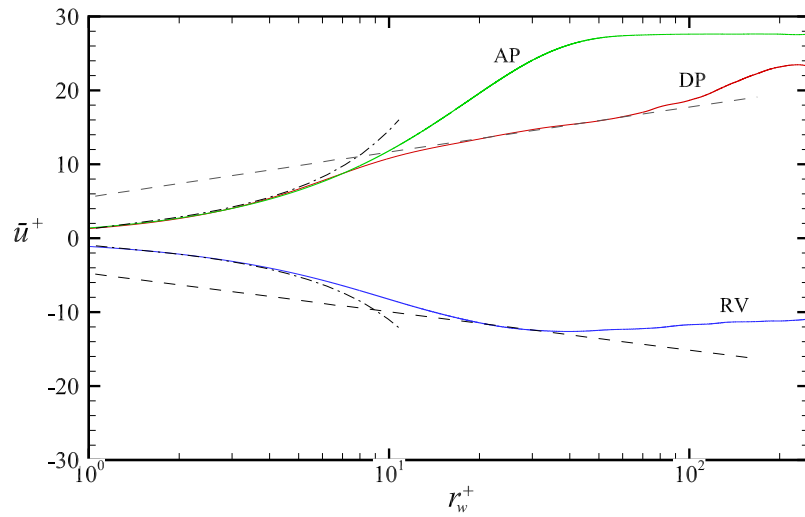


**Figure 4.17:** The time-averaged axial velocities in the near-wall region nondimensionalized by the amplitude of the friction velocity for three intervals of the: acceleration phase (AP) (Green), deceleration phase (DP) (red), flow reversal phase (RV) (blue),  $\bar{u}^+ = r_w^+$  (black dot-dashed curve) and log law (black dashed curve).

#### 4.5.10 Oscillating pressure field

The time-dependent pressure is produced at two radial positions to show the turbulence fluctuations through the pressure. Figure 4.18 (a) and (b) show the axial velocities and their corresponding pressures, non-dimensionalized by  $(\rho^* \hat{u}^{*2})$ , for two consecutive oscillation cycles with  $Re_\delta = 400$  and  $\lambda = 10$  at  $\zeta = 0.95$  and  $0.99$ , respectively. It can be noticed in Fig. 4.18 that there is a phase change between the pressure and the velocity with a phase lead of approximately  $\pi/2$  for the pressure.

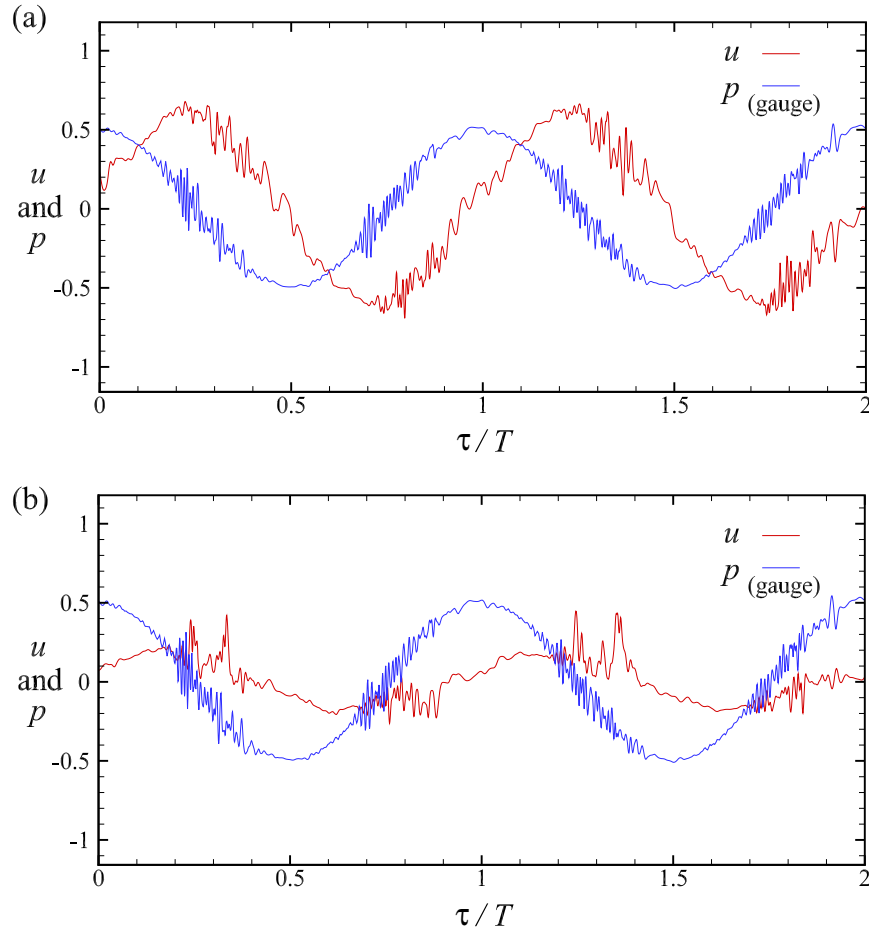


**Figure 4.18:** Axial velocity ( $u$ ) and gauge pressure ( $p$ ) for the flow conditions of  $Re_\delta = 400$  and  $\lambda = 10$  at: (a)  $\zeta = 0.95$  and (b)  $\zeta = 0.99$ .

The profiles of the pressure appear to be close to those of the velocity regarding the degree of turbulence during the deceleration phases. However, the frequencies of the flow fluctuations are low around the velocity curves compared with those of the pressure as shown in Fig. 4.18. Also, the pressure does not show significant changes as same as the velocity at  $\zeta = 0.99$ , where the disturbances exhibit some sudden high amplitudes. In addition, the figure reveals that the maximum values of the pressure fluctuations are seemingly constant with respect to the radial positions. The turbulence activity of the pressure at  $Re_\delta = 400$  and  $\lambda = 10$  gives an additional proof that the second stage of the transition happens at about these flow conditions.

# Chapter 5

## Roughness-induced Transition and Turbulence

### 5.1 Overview

There have been several studies to assess the influence of wall imperfections on fluid flows, more specifically about disturbances initiated by small asperities distributed on the wall. In some cases, where the flow is driven sinusoidally inside the pipe as observed in heat exchangers, combustion chambers, thermoacoustic devices, etc., the wall effect is important due to a few reasons. In particular, since the velocity overshoot of an oscillatory flow shifts toward the wall, especially at high frequencies, the surface roughness is an important factor causing or even delaying the transition. Many investigations have been conducted to examine the stability of the oscillatory flow on smooth and rough walls in the literature. For example, the ratio of  $a/k_s$ , where  $a$  is referred to as the amplitude of the oscillatory free-stream flow and  $k_s$  is the Nikuradse's equivalent sand roughness, has a significant role of intensifying turbulence and raising shear stresses as noticed by the experiment of [Jensen \*et al.\* \(1989\)](#). More importantly, [Sleath \(1987\)](#) has related the defect

velocity near the wall to  $a/k_s$  values as he observed different flow behaviors with various roughness heights. Studies of Zhou *et al.* (2018), Ghodke & Apte (2016) that employed numerical methods for an oscillating flow to explore the effects of small spherical particles dispersed over a plate declared two important points. Firstly, Zhou *et al.* (2018) noticed that the arrangements of the solid particles which represent the wall roughness have no impacts on the friction factor in the numerical simulations, and secondly, Ghodke & Apte (2016) reported that the roughness grants a spatial heterogeneity inducing turbulent kinetic energy increment.

A typical method to incorporate the surface roughness in direct numerical simulations (DNS's) is to modify the locations of the cells near the wall or to introduce immersed boundary layers as the case of Forooghi *et al.* (2018). The use of unstructured grids cannot always model the surface roughness effectively and thus they need to be adapted to capture the most significant features of the flow characteristics. Although turbulence simulations necessitate extra attention near the wall, the pipe wall roughness of the oscillating flow requires even finer mesh adding more numerical challenges. Technically, one strategy to overcome these difficulties is to apply overset mesh (also known as “Chimera”) which has been used for a few different purposes. For instance, Merrill *et al.* (2016) assessed the applicability, effectiveness, and even defects of this technique for pipe simulations at different flow conditions providing acceptable results. In the light of surface roughness, Fischer & Choudhari (2004) supplied some guidances on the accuracy of the overlapped solution of the spectral element method for an array of roughness elements mounted above a flat plate.

The aim of this chapter is to perform numerical simulations exploiting the high accuracy of the spectral element method for overlapping meshes to represent the surface roughness and also to reduce the computational cost required in the near-wall zone. Transition to turbulence triggered by the wall roughness in purely oscillating flows in pipes has not been

investigated, to the best of our knowledge. Therefore, the wall roughness will be introduced as perturbations to examine the stability of the flow at different Reynolds numbers, and the transient behavior of the velocity will be traced in more details up to turbulence conditions. Finally, the analyses of the friction losses with and without roughness are pursued in comparisons with available experimental data.

## 5.2 Overset grid

In pipe flow simulations where the curvature issue is present, the difficulty of producing a mesh with wavy layers near the wall and formal distributions elsewhere arises. The overset mesh with interpolation capability can maintain the accuracy of the spectral element method for the main flow with an appropriate wall treatment. The computational domain is decomposed into two partitions in which grids may be easily constructed. The outer subdomain ( $\Omega_o$ ) transfers the data to the inner one ( $\Omega_i$ ) where the major data of the simulations are collocated. The internal boundary conditions (*int*) are specified at the beginning of the computations for each mesh as follows:

$$u(\zeta, \tau)^{\Omega_i} = u(\zeta, \tau)_{int}^{\Omega_o}, \quad (5.1)$$

$$u(\zeta, \tau)^{\Omega_o} = u(\zeta, \tau)_{int}^{\Omega_i}, \quad (5.2)$$

where  $u(\zeta, \tau)_{int}$  acts as a Dirichlet-type velocity at a specific radial position ( $\zeta$ ) at the end of each time-step for the inner and outer subdomains. Both the inner and the outer subdomains extend for a specified distance through the interpolated zone, and the shared cells of outer mesh are non-conforming. Consequently, the local solution is not as accurate as that of the non-decomposed zone, and numerical errors in both spatial and temporal dis-

cretizations occur most likely. A local iteration process is implemented to minimize these errors and to achieve fast convergence in all the simulations presented in this study.

### 5.2.1 Surface roughness parametrization

The receptivity phase, disturbance growth, and vortex breakdown are the basic stages of the typical transition to turbulence. The first stage is considered linear and it can be predicted in the two-dimensional domain. The transition process begins by inducing disturbances to evolve with time and propagate in the space, and then the effect of the three-dimensionality starts dominating. Despite the roughness effect is usually confined in the viscous region where the change of the velocity gradient ( $\partial u/\partial r$ ) is significant, the core region may be also affected at some flow conditions. We consider 2-D surface roughness for which the height and the length of each roughness element vary owing to the nature of the spectral element configuration.

Figure 5.1 (a), (b) and (c) display the the entire mesh for the pipe geometry investigated herein. One should consider a certain number of finite elements ( $E$ ) and the GLL grid points within each element to model a rough pipe in the spectral element method. Figure 5.1 (d), (e) and (f) magnify these elements in a portion of the pipe to highlight where the inner mesh ends (e.g.  $\zeta = 0.95$ ) and the outer mesh begins (e.g.  $\zeta = 0.89$ ). Note that the grid points of an  $N$ -degree polynomial inside each finite element are not shown in Fig. 5.1 (d), (e), and (f) for graphical simplicity. The main flow region away from the wall does not have any distorted mesh, and it preserves its numerical accuracy with the interpolation boundary condition (*int*) at the top ( $\zeta = 0.95$ ). The outer subdomain ( $\Omega_o$ ) contains the mesh waviness taking into account the grid points of the spectral element method from the finite elements and GLL points.

The main objective of this study is not featuring the roughness elements according to their

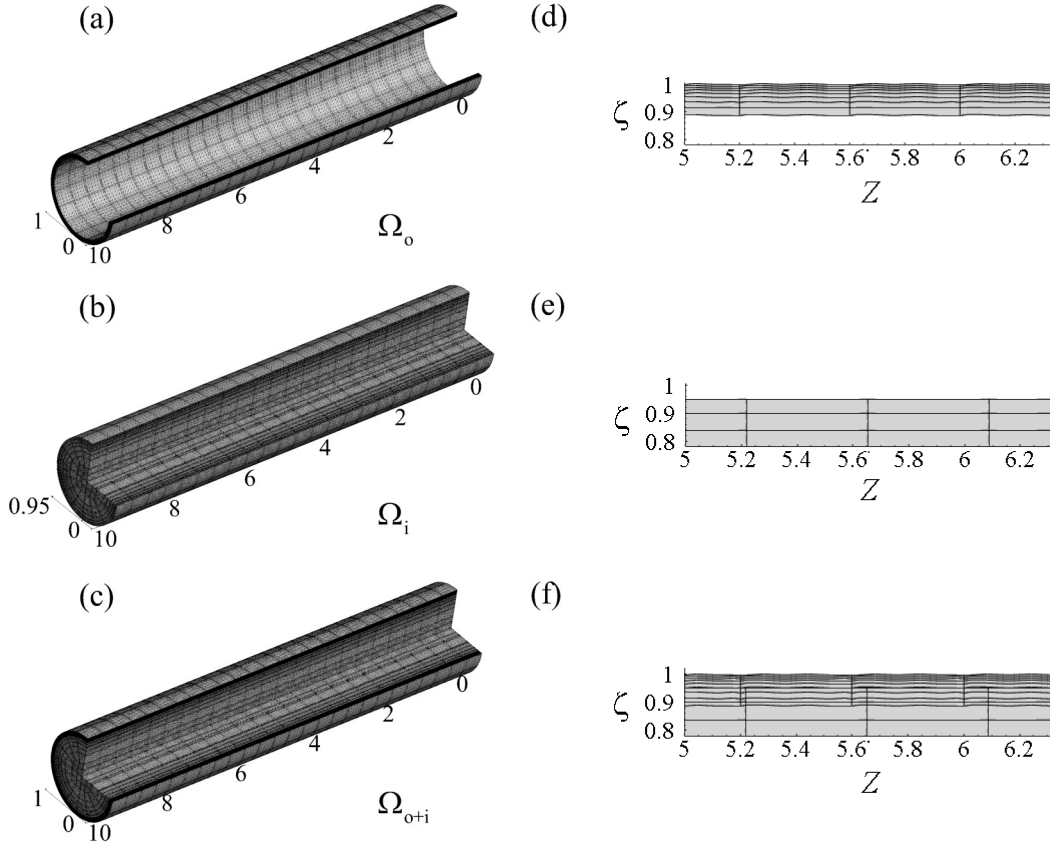


**Figure 5.1:** Computational meshes including the frames of finite elements and Gauss-Lobatto-Legendre ( GLL) points: (a) outer mesh for  $\Omega_o$ , (b) inner mesh for  $\Omega_i$ , and (c) combined mesh for  $\Omega_{o+i}$ . finite elements near the wall: (d) outer elements, (e) inner elements, and (f) combined elements.

size, density, and height. Instead, it focuses on the outcomes of wall irregularity on transition and how instabilities can be generated by small roughness elements only. A corrugated surface along the  $z$ -direction parallel to the wall is constructed by using the following equation:

$$f(Z) = 1 - \varepsilon_{sr} \left[ \cos^{-1} \left( \cos \left( \frac{\alpha Z}{l} \right) \right) \right], \quad (5.3)$$

where  $Z$  is equivalent to  $z/\lambda$  or  $z^*/R^*$ . Equation (5.3) is executed in a user-defined routine provided by NEK5000 modifying the shape of the outer mesh as a wavy wall, which has smooth peaks and variable lengths depending on GLL point distributions along the



$z$ -coordinate. The values of  $\alpha$  and  $\iota$  selected in the present analysis are  $2\pi$  and 0.02 respectively, yielding a roughness density of 500 along the pipe which has the maximum inner radius of 0.01 m and the length of 0.1 m. Three values of dimensional roughness ( $\epsilon_{sr}^*$ ) equivalent to the corrugation amplitudes are used in this study, and the effect of roughness is characterized by  $\epsilon_{sr}$  which is the ratio of the roughness height ( $\epsilon_{sr}^*$ ) to the pipe radius ( $R^*$ ) for the given geometry.

### 5.2.2 Grid convergence study and implementation

The driving force ( $F$ ) with zero initial velocity condition at  $\tau = 0$  is imposed for each simulation, and after several cycles of oscillations (15 to 16), the flow reaches a long-time oscillation state. The accuracy of Nek5000 and the overset approach are validated with the laminar flow against the exact solution of [Sexl \(1930\)](#). In the numerical simulations, the grid resolution was controlled by changing the number of elements ( $E$ ) and the polynomial degree ( $N$ ). The convergence was achieved by  $E = 576$  and  $N = 8$  in the laminar flow, whereas the numbers had to be increased to  $E = 6400$  and  $N = 12$  at the highest  $Re_\delta$  presented in this work. Despite the fact that the turbulent eddies at the Kolmogorov length scale occur at certain times during the oscillation cycle, the total grid points ( $EN^3$ ) we used is believed to be sufficient to capture all relevant scales, since the viscous sub-layer is well resolved in line with other studies, see [Liberto & Ciofalo \(2009\)](#). The spectral element method was able to simulate turbulence at relatively high Reynolds numbers we attempted, ranging from 547.72 to 800 and the Stokes numbers between 9.19 to 25. Three different computational lengths,  $3.5 \cdot D^*$ ,  $5 \cdot D^*$ , and  $7 \cdot D^*$ , were tested, and  $5 \cdot D^*$  was found to be sufficient to ensure fully-developed flows and to reveal all the turbulence structures with periodic boundary conditions at the ends.

### 5.3 Laminar flows with rough wall

Three different roughness heights ( $\epsilon_{sr} = 0, 0.0075,$  and  $0.0125$ ) are implemented in a fully developed laminar flow at  $Re_\delta = 100$  and  $\lambda = 10$ . Figure 5.2 presents the velocity profile at  $\tau/T = 1/16$  for one Stokes number ( $\lambda = 10$ ) in the midsection of the pipe ( $Z = 5$ ), where  $\tau/T$  is the phase time in a cycle after the long-time oscillatory solution is attained, not the actual time starting from  $t^* = 0$ . The exact solution of Sexl (1930) in Eqn. (2.22) is plotted as a solid line in Fig. 5.2, and the symbols denote the numerical results calculated by the two combined meshes. For the smooth pipe in Fig. 5.2 (a), the numerical solution is not distinguishable from the analytical solution even in the overlapped zone of  $0.89 \leq \zeta \leq 0.95$ . The rough pipe in Fig. 5.2 (b), however, generates a slight velocity deviation mostly near the wall in comparison with the smooth pipe solution. Because of the computing limitations, only two cases of  $\epsilon_{sr} = 0$  and  $0.0075$  will be considered for further investigations in transition and turbulence.

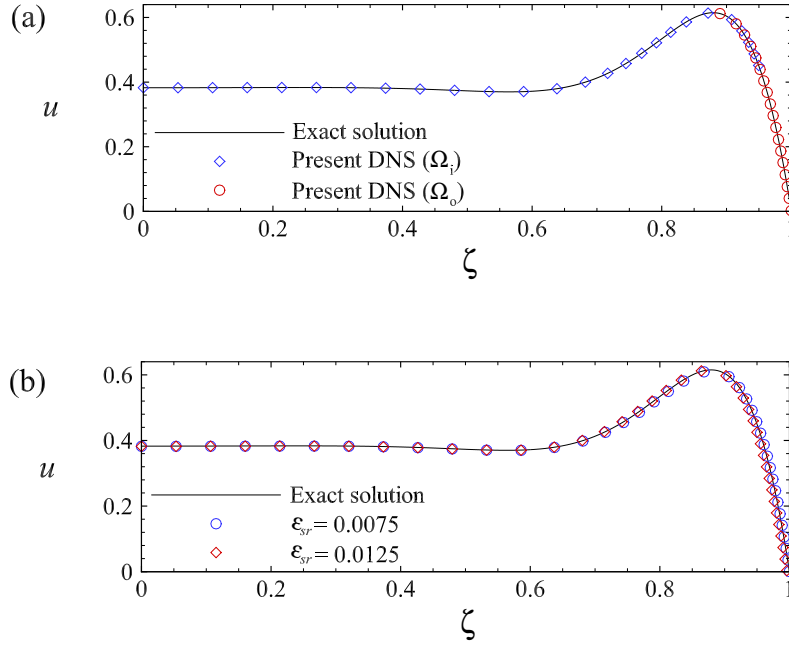


**Figure 5.2:** The axial laminar velocity profile of the combined domain ( $\Omega_{o+i}$ ) at  $Re_\delta = 100$ ,  $\lambda = 10$ , and  $\tau/T = 1/16$  compared with the exact solution of [Sexl \(1930\)](#) for the smooth pipe: (a)  $\varepsilon_{sr} = 0$  and (b)  $\varepsilon_{sr} = 0.0075$  and  $\varepsilon_{sr} = 0.0125$ .

Based on the results shown above, the differences in flow stability between experiments and theories found in the literature may be attributed to the precision of the laminar flow representation in the laboratory compared with the theoretical exact solution. One possible explanation is that any disparity between the measured velocity and the exact solution can make a significant difference in the stability results owing to the fact that the second derivative of the velocity, especially near the wall, directly impacts the flow stability [Lee & Abdulrasool \(2018\)](#). In the pipes that are not smooth, the height of the roughness element ( $\varepsilon_{sr}$ ) may also play important roles. If this height is much less than the Stokes thickness ( $\delta^*$ ), it has a small amount of effect on the flow since the viscosity dominates and dampens out the growth of disturbances generated by the wall. Small vortices were formed near the relatively smooth wall, and no flow separation was found with the specified roughness parameters. However, for  $\varepsilon_{sr} > 0.0125$ , the flow will undergo adverse pres-

sure gradient leading to flow separation and recirculation. In addition, the mesh density in the  $z$ -direction has to be increased for a high  $\varepsilon_{sr}$  in order to avoid a mesh distortion.

#### 5.4 Transitional flows with rough wall

This section closely follows the paradigm of [Blondeaux & Vittori \(1994\)](#) where the wavy wall initiates disturbances. There are two stages of transition in the oscillatory flow, considering that the process begins from a disturbed laminar flow and proceeds to a weakly turbulent flow. The surface roughness plays the main role of originating the transition in this study, and the sensitivity to its influence exists in both laminar and non-laminar flows with different degrees of freedom as other dynamic systems do at certain frequencies. Two different roughness heights ( $\varepsilon_{sr} = 0$  and  $0.0075$ ) were examined during the transitional period, although  $\varepsilon_{sr} = 0$  did not promote disturbed flows at  $\lambda = 10$  and  $Re_{\delta} \leq 250$ . Figure 5.3 is plotted during one oscillation cycle at different Reynolds numbers and  $\varepsilon_{sr} = 0.0075$ . Small disturbances began to develop in the near-wall zone first and then they propagated away from the wall. The waiting time after passing the start-up periods was 25 oscillation cycles before the collection of the data. The effect of surface roughness was to trigger the very first stage of transition at somewhat different times within the cycle, depending on the flow conditions and the radial positions probed.

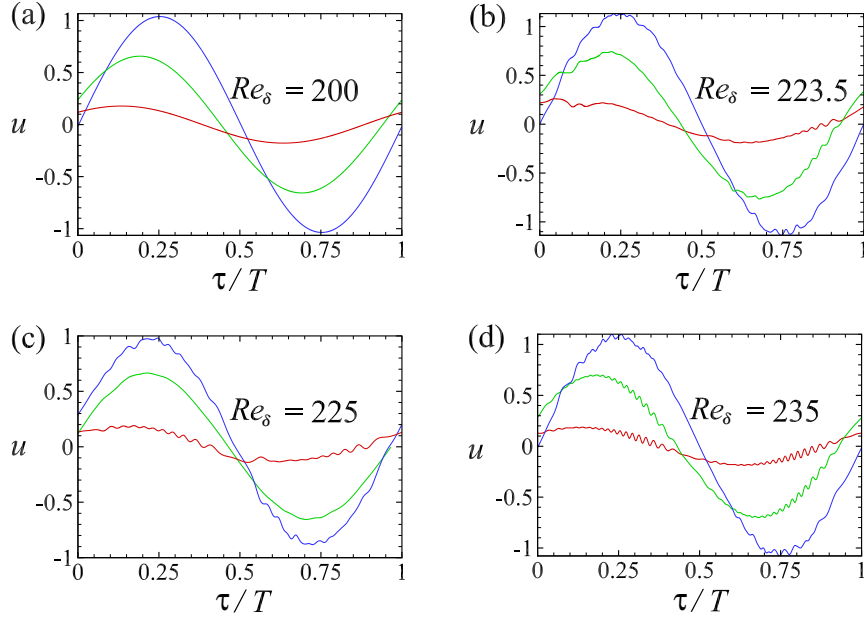


**Figure 5.3:** The temporal evolution of the axial velocity at three radial positions ( $\zeta = 0$  (blue), 0.9 (green), and 0.99 (red)), the transition induced by surface roughness only at different  $Re_\delta$ 's ranging from 200 to 235 for  $\lambda = 10$  and  $\varepsilon_{sr} = 0.0075$ .

It is observed in Fig. 5.3 that the wavy curves appear mostly in the decelerating phases with different strengths across the radial positions ( $\zeta = 0, 0.9$ , and  $0.99$ ), whereas the rest of the cycle shows relatively more smooth curves. The time history of computational results affirms that the flow is completely laminar across the whole cross section at  $Re_\delta = 200$ , as shown in Fig. 5.3 (a). When the Reynolds number was increased to 223.5, the irregular flow patterns were developed and followed by relaminarization as exhibited in Fig. 5.3 (b), indicating the effect of surface roughness and the inertial force of fluid. A similar trend is noticed at  $Re_\delta = 225$  for the disturbances with slightly greater amplitudes in Fig. 5.3 (c). At  $Re_\delta = 235$ , the flow experiences more fluctuations continuing their appearance, albeit only one cycle is plotted in Fig. 5.3 (d). This behavior can be described as a disturbed laminar flow declaring the onset of transition.

The first stage of the transition in Fig. 5.3 indicates that a flow sustained by low-frequency

fluctuations appearing in specific zones and phases during the oscillation cycle is transiently unstable. The disturbed laminar flow affected by the wall interactions only may have an inconsiderably different behavior from the flows disturbed by other types of perturbations. The critical Reynolds number ( $Re_\delta = 223.5$ ) found here is attributed to the roughness height, and our analysis of rough-wall representation is assumed to model the physics reasonably well. In addition, the results were monitored for many oscillations since the disturbances may decay after some cycles.

### 5.5 Turbulent flows with rough wall

The receptivity to small perturbations increases due to the nonlinearity of turbulent flow. Physically, the flow can be disturbed by a variety of sources such as the vibrations of the pipelines or the imperfect finishing on the internal pipe surface. In the numerical simulations, a small change in the time-step, mesh resolution, or initial condition leads to somewhat different fluctuations of turbulence. Therefore, all results presented herein are obtained after the time-averaged ( $\bar{u}$ ) and root-mean-square ( $u_{\text{rms}}$ ) velocities become invariant to any changes made to the computational parameters. High-resolution DNS's are performed for the two cases of roughness ( $\varepsilon_{sr} = 0$  and  $\varepsilon_{sr} = 0.0075$ ) with all the other input parameters remaining the same. The data were collected after passing the initial transient period.

Table 4 presents some DNS parameters for the flow condition of  $Re_\delta = 800$  and  $\lambda = 10$  in the smooth and rough pipes. The grid sizes are determined in compliance with the wall status, and in the table the maximum values of  $\Delta r^*$ ,  $\Delta R^* \theta$ , and  $\Delta z^*$  are nondimensionalized by  $\hat{u}_\tau^*/\nu^*$  in the radial, azimuthal, and axial directions, respectively, for the so-called inner variables with the superscript  $+$ , while  $\Delta t^*$  is scaled with  $\hat{u}_\tau^{*2}/\nu^*$ . The rough surface needs a high resolution near the wall to include all the roughness details influencing

**Table 5.1:** DNS parameters used for a flow condition at  $Re_\delta = 800$  and  $\lambda = 10$ .

Domain ( $L^* = 5 \cdot D^*$ )	Smooth Wall ( $\varepsilon_{sr} = 0$ )	Rough Wall ( $\varepsilon_{sr} = 0.0075$ )
Total grid points	$10.2 \times 10^6$	$11.1 \times 10^6$
Maximum grid space ( $\Delta r^+, \Delta R\theta^+, \Delta z^+$ )	5.76, 9.6, 6.4	6.3, 10.5, 7.0
Initial time step ( $\Delta t^+$ )	0.01	0.012
Time interval for acquired samples (time steps)	100	100
Duration of samples stored ( $\tau/T$ )	[0, 2]	[0, 2]

the flow. Splitting the computational domain into two parts can increase the efficiency in the treatment of the surface roughness. For example, the DNS data were produced separately for the outer domain, which reduces the time and effort for the post-processing procedures. In addition, the outer mesh of the combined domain has 24 extra grid points than the inner one in the axial direction at the flow conditions presented in Table 4. However, the mesh resolution in the radial direction was increased by more than 40 percent to sufficiently cover the roughness details in that direction. The time step was chosen to be variable and was initialized at  $10^{-5}$  sec, while the CFL number was fixed at 0.05. DNS results were recorded at every 100 time steps for two consecutive oscillation cycles.

In Fig. 5.4 plotting turbulent flow results, one of the three flow conditions of [Feldmann & Wagner \(2012\)](#)'s DNS showing turbulence bursts is taken and compared with the current results at  $Re_\delta = 713.87$  and  $\lambda = 9.19$  for the smooth pipe to corroborate the accuracy of our work. The numerical simulation of [Feldmann & Wagner \(2012\)](#) validated using the experimental LDA data was initiated by a fully developed turbulent flow that is statistically stationary ( $\lambda = 0$ ). The time-varying axial velocities of our and [Feldmann & Wagner \(2012\)](#)'s DNS results are shown for a half cycle in Fig. 5.4 (a) and (b) respectively. Somewhat different velocity fluctuations appear between the two DNS's, but the turbulence

statistics show small variances among the three oscillation phases (ED, LD, and RV) as illustrated in Fig. 5.4 (c) and (d). The phase-averaged velocity ( $\bar{u}^p$ ) and the associated RMS fluctuation velocity,

$$u_{\text{rms}}^p = \sqrt{(\overline{u^2})^p - (\bar{u}^p)^2}, \quad (5.4)$$

are plotted in terms of the wall distance,

$$r_w^+ = (R^* - r^*) \left( \frac{u_\tau^{*p}}{v^*} \right), \quad (5.5)$$

with phase-averaged friction velocity ( $u_\tau^{*p}$ ). The phase averages involve the time from the beginning of the cycle to ED, LD, and RV phases, after the long-time oscillation is attained. The discrepancies in Fig. 5.4 (c) and (d) can be attributed to the role of the initial conditions which are imposed differently between the two DNS's.



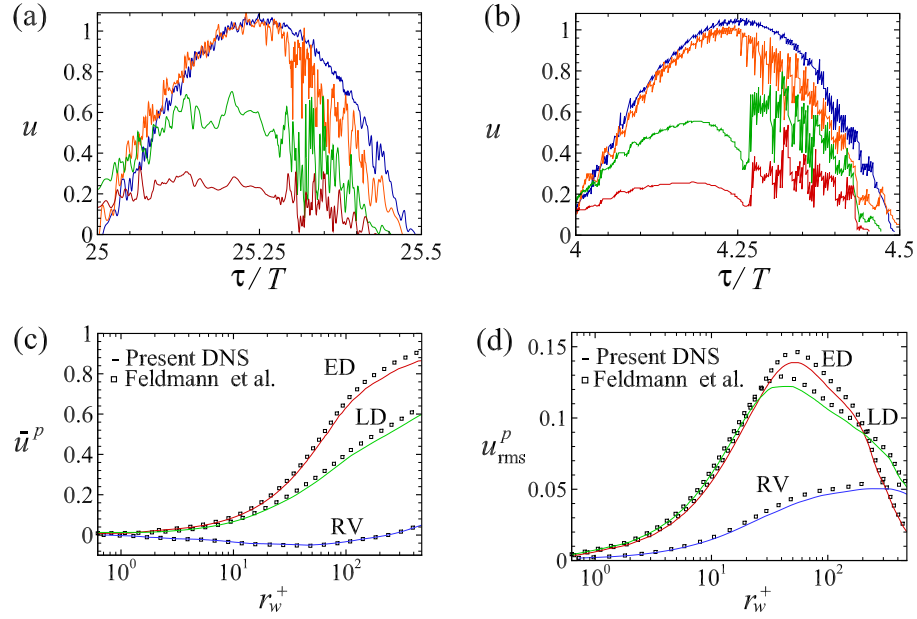


**Figure 5.4:** DNS comparisons for the smooth pipe: (a) instantaneous axial velocity of the present dns, (b) instantaneous axial velocity of [Feldmann & Wagner \(2012\)](#)s’ DNS, (c) phase-averaged velocity ( $\bar{u}^p$ ), and (d) RMS fluctuation velocity ( $u_{rms}^p$ ). the curves in (a) and (b) are at four radial positions:  $\zeta = 0.02$  (blue),  $0.74$  (orange),  $0.94$  (green), and  $0.98$  (red). mean statistics are at the early deceleration (ED), late deceleration (LD), and flow reversal (RV) phases.

Contour plots of turbulent flow at  $Re_\delta = 800$ ,  $\lambda = 10$  are depicted in Fig. 5.5 for the two combined meshes. The results were taken at  $\tau/T = 0.32$  during an oscillation period. The interpolated velocities are consistent between the two subdomains as shown in Fig. 5.5 (a), (b), and (c), and the coherent structures are also observed in the vorticity which will be shown later for the combined mesh. Overall, the results indicate that the overset mesh can be used to study laminar, transitional, and turbulent regimes in an oscillating pipe flow even with high oscillation frequencies. Notice that the roughness height investigated herein is small compared with the corrugation element’s length which is approximately 2% of that of [Blackburn et al. \(2007\)](#). The instantaneous velocities at three radial locations ( $\zeta = 0$ ,  $\zeta = 0.9$ , and  $\zeta = 0.99$ ) for two consecutive cycles are presented in Fig. 5.6 (a) and (b) to demonstrate the effects of  $\varepsilon_{sr} = 0$  and  $\varepsilon_{sr} = 0.0075$  on the flow behavior.

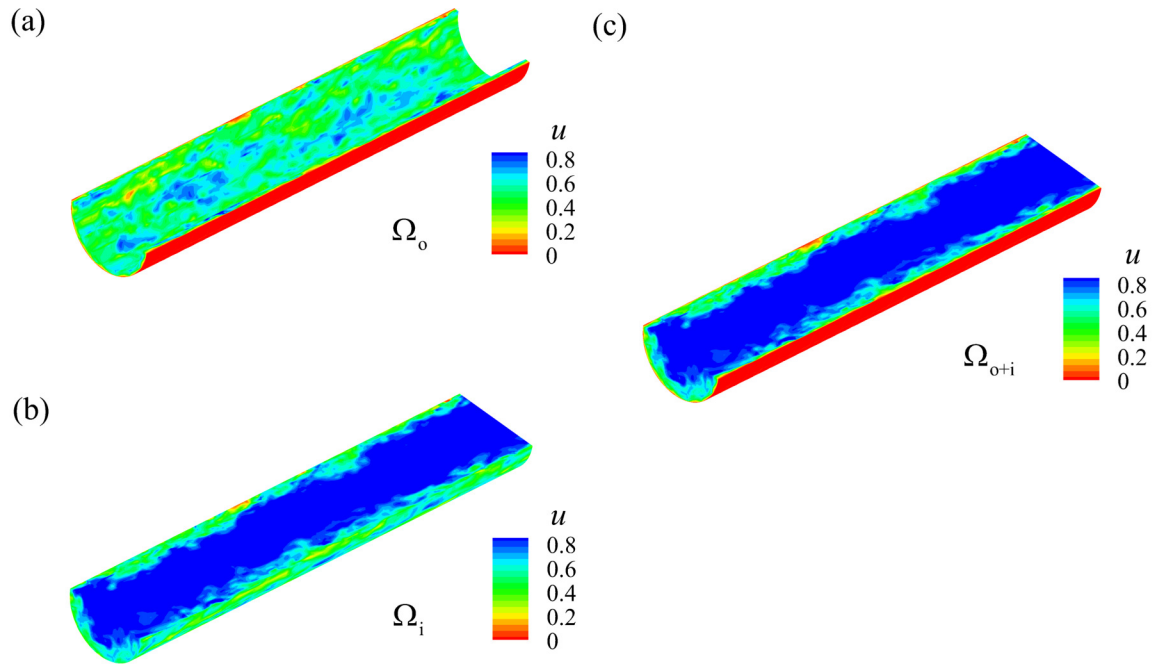


**Figure 5.5:** Contour plots of the axial velocity: (a) outer subdomain ( $\Omega_o$ ), (b) inner subdomain ( $\Omega_i$ ), and (c) combined domain ( $\Omega_{o+i}$ ) at  $Re_\delta = 800$ ,  $\lambda = 10$  and  $\tau/T = 0.32$  for  $\varepsilon_{sr} = 0.0075$ .

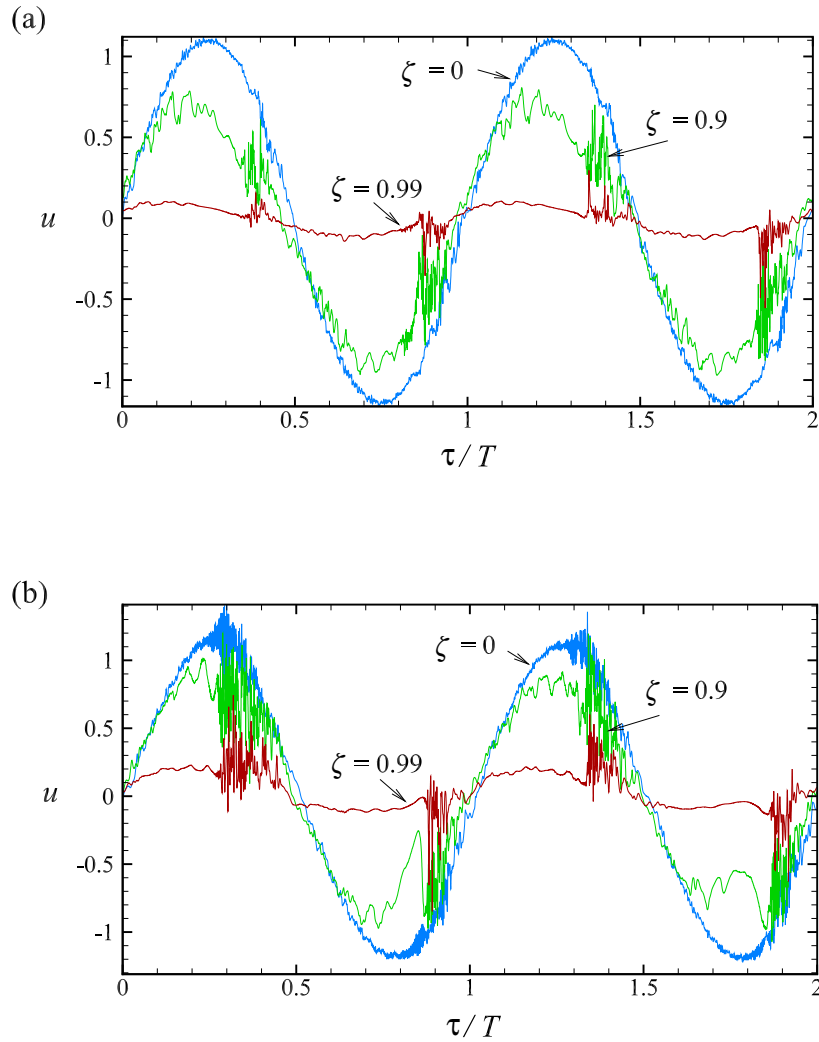


**Figure 5.6:** The time-varying axial velocities at  $Re_\delta = 800$  and  $\lambda = 10$  for two roughness heights: (a)  $\epsilon_{sr} = 0$  and (b)  $\epsilon_{sr} = 0.0075$ .

The turbulence induced by surface roughness of  $\epsilon_{sr} = 0.0075$  has greater intensity not only near the wall but also at the center of the pipe, although turbulence bursts still appear in the decelerating phases similarly to the  $\epsilon_{sr} = 0$  case. Note that the flow was initialized by a zero velocity condition in both cases of roughness. The turbulence bursts are not symmetrical in the time history of random fluctuations. This phenomenon becomes even more obvious in the case of rough wall. The reason is that the events of each oscillation

cycle are affected by those of the previous one. The spatial homogeneity of turbulence in the axial and azimuthal directions was verified by calculating the RMS velocity ( $u_{rms}$ ) at various positions along the two coordinates. The cycle-averaged RMS fluctuations velocities are compared at different positions of the pipe, and the results showed a good agreement as illustrated in Fig. 5.7.

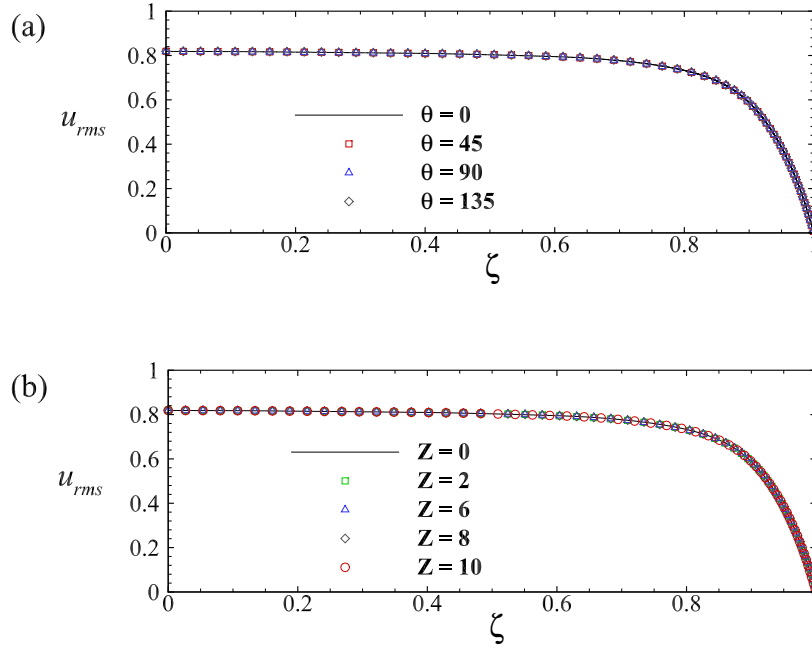


**Figure 5.7:** Root-mean-square (RMS) velocity with respect to the radial direction at  $Re_\delta = 800$  and  $\lambda = 10$  for  $\epsilon_{sr} = 0.0075$ : (a) azimuth direction and (b) axial direction.

## 5.6 Time-dependent wall shear stress ( $\tau_w^*$ )

The effect of wall roughness can be seen through not only the velocity curves but also the wall shear stress profiles. The disturbance of the latter in the case of the rough wall is due to the high gradient fluctuations of the velocity and pressure. The wall shear stress ( $\tau_w^*$ ) can be obtained from the solution of Eqn. (3.2) directly, and due to the special treatment of using two meshes near the wall in this study, the wall velocity derivatives are be-

lieved to be sufficiently accurate. The results of wall shear stresses shown in Fig. 5.8 were computed in accordance with the velocity values of Fig. 5.6 for one cycle only. The solution accuracy of wall shear stress results has been confirmed with the exact solution of the laminar flow, and an excellent agreement was achieved.

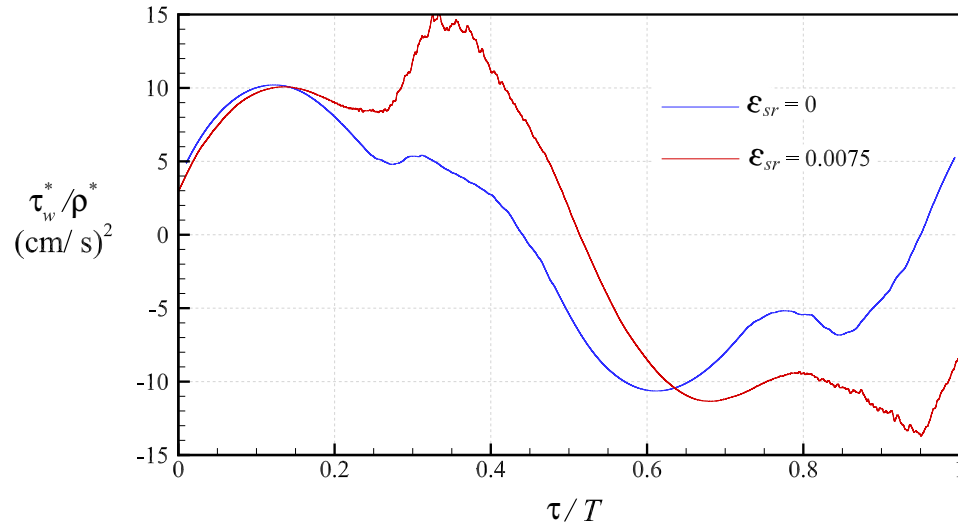


**Figure 5.8:** The time-dependent wall shear stresses,  $\tau_w^*/\rho^*$  (cm/s)<sup>2</sup>, at  $Re_\delta = 800$  and  $\lambda = 10$  for  $\epsilon_{sr} = 0$  (blue) and 0.0075 (red).

The turbulence may be predicted near the wall if there is a wall shear stress excitation, and some investigators such as [Lodahl \*et al.\* \(1998\)](#) declared the second stage of transition to turbulence based on those measurements. The flow conditions of Fig. 5.6 are used to calculate the wall shear stresses for the rough and smooth pipes in Fig. 5.8. The wall shear stress profile encounters a significant change in the case of  $\epsilon_{sr} = 0.0075$  more than in the smooth pipe, showing that the phases, fluctuations, and peaks are different between the two cases of roughness. The wall shear stress is higher and more fluctuating when the flow reaches its maximum turbulence level, comparing Fig. 5.8 with the results of Fig. 5.6. The figures also reveal that there is a phase difference between the velocity

and the wall shear stress. In the first stage of the transition, we analyzed samples of wall shear stresses and the corresponding velocities taken at different  $Re_\delta$ 's and  $\lambda$ 's, albeit not shown in this paper. The data showed that the flow disturbances of the velocity appear during the deceleration phases, although the profiles of the wall shear stress are relatively smooth because the velocity fluctuations have much smaller effect than the viscosity in the vicinity of the wall. Therefore, it is uncertain whether the onset of transition can be determined precisely by tracing the wall shear stress profiles only.

### 5.7 Friction coefficient ( $C_f$ )

Friction associated with time-varying quantities is not uniquely defined in the literature. For example, [Pedocchi & Garcia \(2009\)](#) established a new dimensionless relation to accurately estimate the friction factor of the oscillatory flow since the existing friction factor correlations may not be appropriate, especially in the second stage of transition to turbulence. The influence of the pipe curvature is negligible in the near-wall region at high oscillation frequencies ( $\lambda \rightarrow \infty$ ). Therefore, in the present study, the friction losses in the pipe flows are collated with the existing experimental data of the planer oscillatory flows. The friction coefficient is represented by using the wall shear stress amplitude ( $\hat{\tau}_w^*$ ), not necessarily associated with the maximum turbulence energy. At three turbulent flow conditions ( $Re_\delta = 800, 600, \text{ and } 547.72$  with  $\lambda = 10, 20, \text{ and } 25$ , respectively), the friction coefficients of the two roughness cases ( $\varepsilon_{sr} = 0$  and  $\varepsilon_{sr} = 0.0075$ ) are shown in Fig. 5.9. The friction coefficient ( $C_f$ ) was calculated according to the following equation:

$$C_f = \frac{\hat{\tau}_w^*}{\frac{1}{2}\rho^* \hat{u}^{*2}}. \quad (5.6)$$

One value of [Lodahl et al. \(1998\)](#)'s friction coefficients for a smooth pipe and the exper-

imental data of [Jensen \*et al.\* \(1989\)](#), [Sleath \(1987\)](#) which studied a flat-plate boundary layer of a purely oscillating flow, are compared in Fig. 5.9.

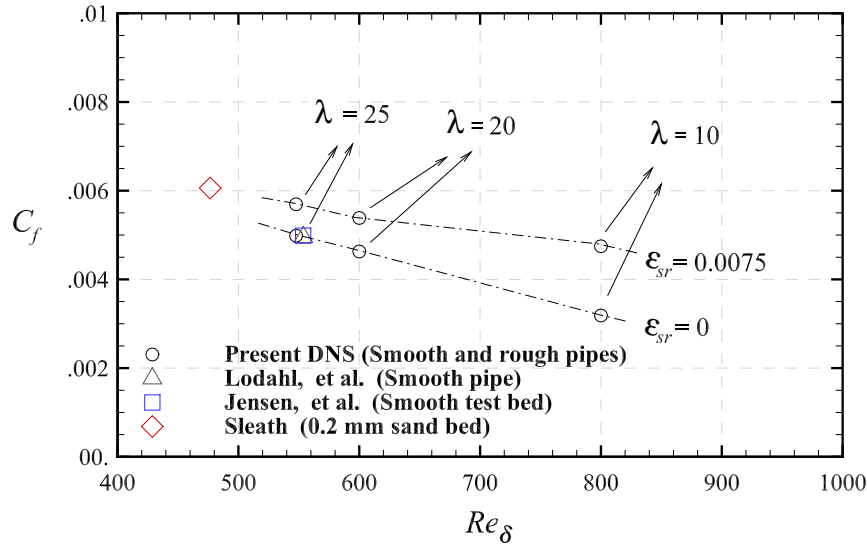


**Figure 5.9:** The friction coefficients at different  $Re_\delta$ 's,  $\lambda$ 's, and  $\epsilon_{sr}$ 's, presenting a comparison between the present dns for the smooth and rough pipes and the results of [Jensen \*et al.\* \(1989\)](#), [Lodahl \*et al.\* \(1998\)](#), [Sleath \(1987\)](#).

The three experimental data are chosen in the turbulent regime where turbulence bursts occur during parts of the oscillation cycle. The friction coefficient for the smooth wall of [Jensen \*et al.\* \(1989\)](#) which apparently has a similar value to that of [Lodahl \*et al.\* \(1998\)](#) as shown in Fig. 5.9 agrees well with the present DNS result of the smooth pipe at  $\lambda = 25$ . It turns out that the result of [Sleath \(1987\)](#) with the roughness height of 0.2 mm has a similar trend to that of the present DNS results with the roughness height of 0.075 mm. Since the peak velocity tends to be close to the wall with a smaller Stokes thickness ( $\delta^*$ ), the friction coefficient increases with the Stokes number ( $\lambda$ ), indicating that the level of shear stress is elevated at high frequencies. The viscous contribution begins to lessen everywhere at relatively high Reynolds numbers, and the friction coefficient reduces to small values. Figure 5.9 clearly demonstrates the dependence of friction coefficient on the sur-

face roughness and the Reynolds number.

### 5.8 Vorticity in the presence of surface roughness

The wall imperfections produce an intense turbulence and an additional formation of vortices. These structures have been observed in experiments and characterized according to their appearance during the oscillation cycle. For instance, [Mujal-Colilles \*et al.\* \(2016\)](#) described the instantaneous vortices of a rough-wall oscillatory flow as coherent structures similar to turbulence bursts which emerge during a near-wall flow reversal and disappear periodically. In this study, the bursting behavior is correlated with the vortex structures, particularly near the wall where the first turbulence bursts appear. Our simulation at the critical Reynolds number also exhibited small vortices in the near-wall region. It was noticed that these vortices propagated in the next step of transition toward the central axis of the pipe ( $\zeta = 0$ ), and their strengths were enhanced by the appearance of turbulence bursts at relatively higher Reynolds numbers. The vortices at  $Re_\delta = 800$  and  $\lambda = 10$  for the smooth and rough pipes are calculated and presented in Fig. 5.10. The results of Fig. 5.10 (a) and (c) are taken at the early acceleration phase (near the beginning of the flow reversal) when the vortices are firstly created according to [Mujal-Colilles \*et al.\* \(2016\)](#). Turbulence bursts begin to evolve near the beginning of the deceleration phase at which the vortices are shown in Fig. 5.10 (b) and (d) for the two cases with different walls. The instantaneous vorticity shows that the surface roughness causes an increase in disturbances owing to the velocity gradients which are smaller in the case of  $\varepsilon_{sr} = 0$  than those of  $\varepsilon_{sr} = 0.0075$  in all phases.



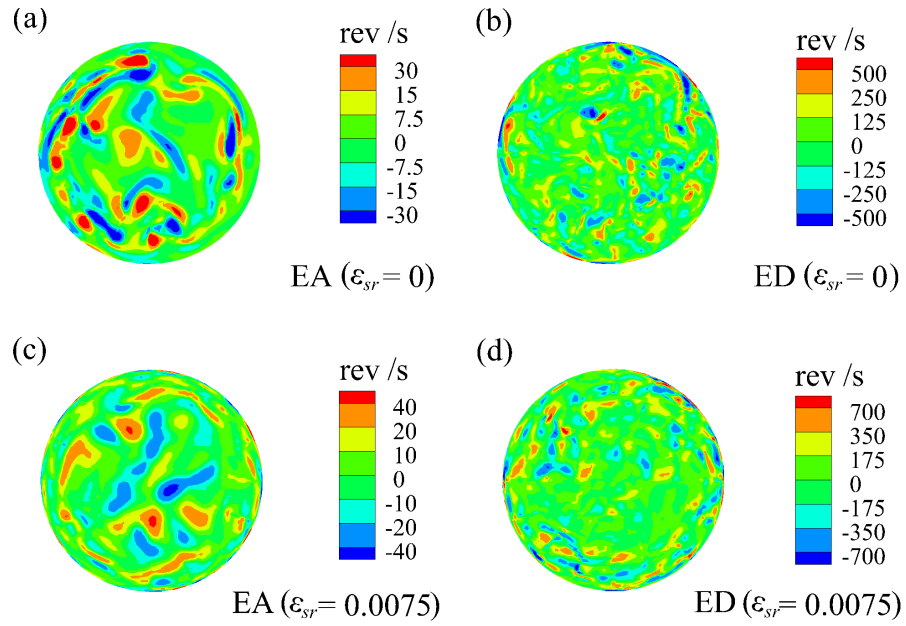


**Figure 5.10:** Cross-section contours of the instantaneous axial vorticity (rev/s) of the early acceleration (EA) and early deceleration (ED) phases at  $Re_\delta = 800$ ,  $\lambda = 10$ , and  $z = 5$  for the two roughness heights: (a) and (b) for  $\epsilon_{sr} = 0$ , (c) and (d) for  $\epsilon_{sr} = 0.0075$ .

# Chapter 6

## Conclusions and Recommendations

### 6.1 Conclusions

This thesis is devoted to finding the critical Reynolds numbers both theoretically and computationally using the quasi-steady method and the existing DNS code. The theory is based on the frozen profiles to the temporal changes of the laminar base flow velocity transforming the Navier-Stokes equations for the axisymmetric domain into an Orr-Sommerfeld equation with time-dependent coefficients. The presented results demonstrated that the flow is unstable when the growth rate of disturbance is positive for a sufficient time period as assessed by the current theory, whereas the instability was detected from the waviness in the profile of the axial velocity and/or wall shear stress as determined from the computations.

By introducing a simple model equation, the solution of the quasi-steady method indicated that there is a dominated transient growth within an oscillation cycle that cannot be predicted by the Floquet theory, which is known as a rigorous tool for stability analysis. The proposed model equation, resembling the first-order ordinary differential equation,

revealed that the cycle-averaged growth rate of the quasi-steady analysis is analogous to the Floquet exponent; however, the same equality was not confirmed in this study for the hydrodynamic stability problem, which is a partial differential equation in time and space. Also, it turns out that both theories of the quasi-steady method and the special variation of the multiple scales method can reach the same solution with equivalent eigenvalues and similar predictions.

The simplicity of the quasi-steady method was reflected into the neutral stability curves of the linear stability problem, among which the critical Reynolds number varied significantly at the low Stokes numbers and remained approximately the same for others. By increasing the Stokes number, the instability regions extend to a wide range of wave numbers, indicating the sensitivity of the flow stability to small disturbances when the Stokes thickness becomes very thin. More importantly, considering the same criterion, the critical values were compared with other available data, and the predictions of the quasi-steady method qualitatively agreed with those of the experiments. However, the literature shows discrepancies in the transition thresholds between theories and experiments, where the accuracy of representing the base flow is believed to be the main reason. In this regard, a comparison made between the laminar velocity and its derivatives demonstrated that a small difference in the amount of the second spatial derivative dominating the stability problem causes the experimental results to deviate enormously from those of the theories.

Since the stability analysis by the quasi-steady method deals with the laminar base flow through acquiring the cycle-averaged growth rate of disturbance, it is not certain if this theory can predict the turbulence and relaminarization happening within parts of an oscillation cycle at some flow conditions. However, the present assumption was employed to compute the growth rates at certain Reynolds numbers, where the flow is expected to experience turbulence, and the results showed positive values during the entire cycle. In

contrast, at very low Stokes numbers and wave numbers corresponding to the most unstable modes, negative values of the growth rate were obtained even for high Reynolds numbers.

The new mathematical relation formulated from the two terms related to the quasi-steady method in the stability equation confirmed the approximate accuracy of the theoretical results. This inequality based on the order-of-magnitude analysis implies that the Reynolds number needs not to be very high to validate the current theory for stability prediction. Although the imaginary parts of the eigenvalues were interpreted as the growth rates of disturbance, the real eigenvalues are still important in the quasi-steady assumption since they represent the change rate of the laminar flow. After implementing the proposed assessment at two Stokes numbers, the amounts of error estimated from the two terms of the inequality changed with these conditions.

Nevertheless, Direct numerical simulations (DNS) were performed for a wide range of flow conditions where a possible transition process may take place. The flow instabilities were triggered by small random perturbations introduced as initial conditions at the first stage of transition. This onset of transition from the laminar to disturbed laminar flow was determined at various Stokes numbers prior to the stage where the turbulence bursts first appear. It was confirmed that the results of the 2-D simulations are adequate to predict the transient instability of the oscillating flow since they were approximately equivalent to those of the 3-D simulations, in agreement with the Squire's theorem. The numerical predictions were more contiguous to those of the quasi-steady assumption than the reported data of the Floquet method. In addition, turbulence statistics of the first moment at different computational lengths were tested and the 5-D pipe was found sufficient to include all the relevant turbulence scales with periodic boundary conditions at the ends of the pipe.

A corrugated inner surface was constructed in the combination of the outer mesh modeling the vicinity of wavy wall and the uniform regular mesh of the main flow region. Tran-

sition to turbulence initiated by these wall irregularities was studied by means of direct numerical simulations incorporating the high-order spectral element method (SEM). Two roughness heights were used in the laminar regime, and the transient growth of disturbance led to a disturbed laminar flow was identified at one Reynolds number, which is defined here as the onset of transition for the rough pipe flow. At the highest Reynolds number, the axial velocities exhibited turbulence bursts with high intensities, higher than those of the smooth pipe. Although the shared grid points of the outer mesh are non-conforming, turbulence structures were consistent across the interface boundaries. The resulting wall friction coefficients are in agreement with the experimental results found in the literature, and the amount of their increase due to the surface roughness diminishes with the Stokes number of the flow.

## 6.2 Future work

There are growing interests in the oscillating flows exposed to a magnetic field to suppress or generate some forces in the flow. For example, the study of magnetohydrodynamics (MHD) flows involved in many engineering applications, such as the cooling systems of nuclear reactors, MHD generators, blood flow measurements, pumps, and accelerators, is usually associated with the oscillating flows. For a brief description, the magnetic field, which can be homogeneous and steady, can be applied on the flow field inducing two forces: Lorentz force and electric force, different from the original one which creates the magnetic field. If the flow of the electrically conducting fluid is unidirectional, the current will be a direct current type (DC); otherwise like the case of oscillatory flow, the resulting current will be alternative (see, for example, [Domínguez-Lozoyaa \*et al.\* \(2019\)](#)).

In this regard, the magnetic field itself can be used to control the stability of the flows (see, for example, [Anisur \*et al.\* \(2019\)](#), [Krasnov \*et al.\* \(2004\)](#)) or to convert the unsteady

to steady motions by vanishing the frequencies of the base flow. Therefore, the onset of transition of the purely oscillating flows under the influence of a transverse-steady magnetic field with some intensity ( $H$ ) can be investigated utilizing the results of the present study. Usually, when a sufficient  $H$  is imposed, the viscosity of the fluid increases, leading to the flow stability. As  $Re_m$  increases, the critical  $Re$  becomes high, where the magnetic Reynolds number ( $Re_m$ ) is the ratio of the inertial forces to the resistivity. However, the strong magnetic field can alter the flow from the oscillating to steady current. Note that there are numerical investigations on the pulsating flows enduring a magnetic field in the literature as those in the study of Flores *et al.* (2019), but a few studies were conducted on the purely oscillating flows. Thus, the effect of this external force on the flow stability will be investigated in the future by means of direct numerical simulations.

# References

- AKHAVAN, R., KAMM, R., & SHAPIRO, A. 1991. An investigation of transition to turbulence in bounded oscillatory Stokes flows. Part 2. numerical simulations. *Journal of Fluid Mechanics*, **225**, 423–444.
- ANDERSON, E., BAI, Z., BISCHOF, C., DEMMEL, J., DONGARRA, J., DU-CROZ, J., GREENBAUM, A., HAMMARLING, S., MCKENNEY, A., OSTROUCHOV, S., & SORENSEN, D. 1994. *LAPACK User's Guide*. Release 2.0, The Society for Industrial and Applied Mathematics, Philadelphia.
- ANISUR, R., XU, W., LI, K., DOU, H., KHOO, B., & MAO, J. 2019. Influence of magnetic force on the flow stability in a rectangular duct. *Advances In Appl. Math. and Mech.*, **11**, 24–37.
- BENNEY, D., & ROSENBLAT, S. 1964. Stability of spatially varying and time-dependent flows. *Physics of Fluids*, **7**, 1385–1386.
- BLACKBURN, H., OOI, A., & CHONG, M. 2007. The effect of corrugation height on flow in a wavy-walled pipe. *Proceedings of the 16th Australasian Fluid Mechanics Conference*.
- BLENNERHASSETT, P., & BASSOM, A. 2006. The linear stability of high-frequency oscillatory flow in a channel. *Journal of Fluid Mechanics*, **556**, 1–25.
- BLONDEAUX, P., & VITTORI, G. 1994. Wall imperfections as a triggering mechanism for Stokes-layer transition. *Journal of Fluid Mechanics*, **264**, 107–135.

- ÇARPINLIOĞLU, M., & GÜNDOĞDU, M. 2001. A critical review on pulsatile pipe flow studies directing towards future research topics. *Flow Measurement and Instrumentation*, **12**(3), 163–174.
- CHE, Y., & JIN, L. PEI. 2017. Analysis of the oscillatory Taylor-Culick flow using the multiple time scale method. *Aeronautics and Aerospace Open Access Journal*, **1**(3), 108–114.
- COLEMAN, G., & SANDBERG, R. 2010. A primer on direct numerical simulation of turbulence methods, procedures and guidelines. *Technical Report, Aerodynamics and Flight Mechanics Research Group*, 1–21.
- COLLINS, J. 1963. Inception of turbulence at the bed under periodic gravity waves. *Journal of Geophysical Research Atmospheres*, **68**(21), 6007–6014.
- COOPER, W., YANG, K., & NEE, V. 1993. Fluid mechanics of oscillatory and modulated flows and associated applications in heat and mass transfer—a review. *Journal of Energy, Heat and Mass Transfer*, **15**, 1–19.
- COSGROVE, J., BUICK, J., & TONGE, S. 2003. Evolution of turbulence in an oscillatory flow in a smooth-walled channel: A viscous secondary instability mechanism. *Physical Review E*, **68**.
- COWLEY, S. 1987. In stability of time dependent and spatially varying flows. *Edited by Dwoyer D.L., Hussaini M.Y. (Springer, New York, NY)*, 261–275.
- DAS, D., & ARAKERI, H. 1998. Transition of unsteady velocity profiles with reverse flow. *Journal of Fluid Mechanics*, **374**, 251–283.
- DAVIS, S. 1976. The stability of time-periodic flows. *Annual Review of Fluid Mechanics*, **8**, 57–74.
- DEVILLE, M., FISCHER, P., & MUND, E. 2002. *High-order methods for incompressible fluid flow*. Cambridge University Press.
- DOMÍNGUEZ-LOZOYAA, J., PERALESB, H., & CUEVASA, S. 2019. Analysis of the oscillatory liquid metal flow in an alternate MHD generator. *Revista Mexicana De Física*, **65**, 239–250.



- DRAZIN, P., & REID, W. 1981. *Hydrodynamic stability*. Cambridge University Press.
- ECKMANN, D., & GROTBORG, J. 1991. Experiments on transition to turbulence in oscillatory pipe flow. *Journal of Fluid Mechanics*, **222**(1), 329–350.
- FELDMANN, D., & WAGNER, C. 2012. Direct numerical simulation of fully developed turbulent and oscillatory pipe flows at  $Re_\tau=1440$ . *Journal of Fluid Mechanics*, **13**(32), 1–28.
- FELDMANN, D., & WAGNER, C. 2016. On phase asymmetries in oscillatory pipe flow. *New Results In Numerical and Experimental Fluid Mechanics X*, **132**, 113–122.
- FISCHER, P., & CHOUDHARI, M. 2004. Numerical simulation of roughness-induced transient growth in a laminar boundary layer. *Proceedings of the 34th AIAA Fluid Dynamics Conference*. AIAA 2004-2539, Portland, Oregon, U.S.
- FISCHER, P., KRUSE, G., & LOTH, F. 2002. Spectral element methods for transitional flows in complex geometries. *Journal of Scientific Computing*, **17**, 87–106.
- FISHLER, L., & BRODKEY, R. 1991. Transition, turbulence and oscillating flow in a pipe a visual study. *Experiments In Fluids*, **11**, 388–398.
- FLETCHER, C. 1991. *Computational techniques for fluid dynamics*. 2 edn. Springer-Verlag, New York. Chap. 5.
- FLORES, D., JR, H. WATERS, & DAS, A. 2019. *Magnetic Hydro-Dynamic Propulsion of Blood*. Embry Riddle Aeronautical University. <https://commons.erau.edu/discovery-day/db-discovery-day-2019/poster-session/38/>.
- FOROOGHI, P., STROH, A., SCHLATTER, P., & FROHNAPFEL, B. 2018. Direct numerical simulation of flow over dissimilar, randomly distributed roughness elements: a systematic study on the effect of surface morphology on turbulence. *Physical Review Fluids*, **3**(4), 1–27.
- GHIDAOU, M., & KOLYSHKIN, A. 2002. A quasi-steady approach to the instability of time-dependent flows in pipes. *Journal of Fluid Mechanics*, **465**, 301–330.

- GHODKE, C., & APTE, S. 2016. DNS study of particle-bed-turbulence interactions in an oscillatory wall-bounded flow. *Journal of Fluid Mechanics*, **792**, 232–251.
- GRACE, S. 1928. Oscillatory motion of a viscous liquid in a long straight tube. *The London, Edinburgh, and Dublin Philosophical Magazine and Journal of Science*, **5**(31), 933–939.
- HALL, P. 1978. The linear stability of flat Stokes layers. *Proceedings of the Royal Society*, vol. 359, no. 1697.
- HARRIS, J., PEEVT, G., & WILKINSON, W. 1969. Velocity profiles in laminar oscillatory flow in tubes. *Journal of Scientific Instruments (Journal of Physics E)*, **2**, 913–916.
- HINO, M., SAWAMOTO, M., & TAKASU, S. 1976. Experiments on transition to turbulence in an oscillatory pipe flow. *Journal of Fluid Mechanics*, **75**, 193–207.
- IGUCHI, M., & OHMI, M. 1982. Transition to turbulence in a pulsatile pipe flow-Part 2 characteristics of reversing flow accompanied by relaminarization. *Bulletin of the JSME*, **25**, 1529–1536.
- IGUCHI, M., URAHATA, I., & OHMI, M. 1987. Turbulent slug and velocity field in the inlet region from pulsatile pipe flow. *JSME International Journal*, **30**(261), 414–422.
- IOOSS, G., & JOSEPH, D. 1990. *Elementary stability and bifurcation theory*. 2 edn. Springer-Verlag, New York. Chap. 7.
- JAN, D., SHAPIRO, A., & KAMM, R. 1989. Some features of oscillatory flow in a model bifurcation. *Chemical Engineering Science*, **67**(1), 147–59.
- JENSEN, B., SUMER, B., & FREDSOE, J. 1989. Turbulent oscillatory boundary layers at high Reynolds numbers. *Journal of Fluid Mechanics*, **206**, 265–297.
- JUÁREZ, L., & RAMOS, E. 2003. Direct numerical simulation of transition to turbulence in an oscillatory channel flow. *Comptes Rendus Mécanique*, **331**, 55–60.
- KHOURY, G., SCHLATTER, P., NOORANI, A., FISCHER, P., BRETHOUWER, G., & JOHANSSON, A. 2013. Direct numerical simulation of turbulent pipe flow at moderately high Reynolds numbers. *Journal of Flow, Turbulence and Combustion*, **91**, 475–495.

- KIM, J., MOIN, P., & MOSER, R. 1987. Turbulence statistics in fully developed channel flow at low Reynolds number. *Journal of Fluid Mechanics*, **177**, 133–166.
- KRASNOV, DS., ZIENICKE, E., ZIKANOV, O., BOECK, T., & TRESS, A. 2004. Numerical study of the instability of the Hartmann layer. *Journal of Fluid Mechanics*, **504**, 183–211.
- KURZWEG, U., LINDGREN, E., & LORTHROP, B. 1989. Onset of turbulence in oscillating flow at low womersley Number. *Physics of Fluids*, **A(1)**, 1972–1975.
- LEE, Y. 2002. *Instability of oscillatory flow in ducts and application to solid propellant rocket aeroacoustics*. Ph.D. thesis, University of Illinois at Urbana-Champaign.
- LEE, Y., & ABDULRASOOL, A. 2018. Comparison between theories and experiments in transition of purely oscillating pipe flow. *Proceedings of the 2018 Fluid Dynamics Conference*. AIAA 2018-3390, Atlanta, Georgia, U.S.
- LEE, Y., & BEDDINI, R. 1999. Acoustically-induced turbulent transition in solid propellant rocket chamber flowfields. *Proceedings of the 35th Joint Propulsion Conference and Exhibit*. AIAA-99-2508, Los Angeles, California, U.S.
- LIBERTO, M., & CIOFALO, M. 2009. Numerical simulation of reciprocating turbulent flow in a plane channel. *Physics of Fluids*, **21(9)**, 1–15.
- LODAHL, C., SUMER, B., & FREDSOE, J. 1998. Turbulent combined oscillatory flow and current in a pipe. *Journal of Fluid Mechanics*, **373**, 313–348.
- LUO, J., & WU, X. 2010. On the linear instability of a finite Stokes layer: Instantaneous versus floquet modes. *Physics of Fluids*, **22**.
- MACKLEY, M., & STONESTREET, P. 1995. Heat transfer and associated energy dissipation for oscillatory flow in baffled tubes. *Chemical Engineering Science*, **50(14)**, 2211–2224.
- MERKLI, P., & THOMANN, H. 1975. Transition to turbulence in oscillating pipe flow. *Journal of Fluid Mechanics*, **68**, 567–575.

- MERRILL, B., PEET, Y., FISCHER, P., & LOTTES, J. 2016. A spectrally accurate method for overlapping grid solution of incompressible Navier–Stokes equations. *Journal of Computational Physics*, **307**, 60–93.
- MILLER, J., & FEJER, A. 1964. Transition phenomena in oscillating boundary-layer flows. *Journal of Fluid Mechanics*, **18**(3), 438–484.
- MONKEWITZ, P., & BUNSTER, A. 1987. The stability of the Stokes layer: Visual observations and some theoretical considerations. In: *Dwoyer D.L., Hussaini M.Y. (eds) Stability of Time Dependent and Spatially Varying Flows. ICASE NASA LaRC Series. Springer, New York, NY*, 244–260.
- MUJAL-COLILLES, A., CHRISTENSEN, K., BATEMAN, A., & GARCIA, M. 2016. Coherent structures in oscillatory flows within the laminar-to-turbulent transition regime for smooth and rough walls. *Journal of Hydraulic Research*, **54**(5), 502–515.
- OBREMSKI, H., & MORKOVIN, M. 1969. Application of a quasi-steady stability model to periodic boundary-layer flows. *1298 AIAA Journal*, **7**(7).
- OHMI, M., & IGUCHI, M. 1982. Critical Reynolds number in an oscillating pipe flow. *Bulletin of the JSME*, **25**(200), 165–172.
- OHMI, M., IGUCHI, M., & USUI, T. 1981. Flow pattern and frictional losses in pulsating pipe flow: Part 5, wall shear stress and flow pattern in a laminar flow. *Bulletin of JSME*, **24**(187), 75–81.
- OHMI, M., IGUCHI, M., KAKEHASHI, K., & MASUDA, T. 1982. Transition to turbulence and velocity distribution in an oscillating pipe flow. *Bulletin of the JSME*, **25**(201), 365–371.
- PEDOCCHI, F., & GARCIA, M. 2009. Friction coefficient for oscillatory flow: the rough-smooth turbulent transition. *Journal of Hydraulic Research*, **47**(4), 438–444.
- PEYRET, R. 1986. *Introduction to spectral methods with application to fluid mechanics*. Von Karman Institute Lecture Series 1986-04. Rhode-Saint Genese, Belgium.

- PEYRET, R. 2002. *Spectral methods for incompressible viscous flow*. Springer, New York. Chap. 3.
- RAMAPRIAN, B., & MULLER, A. 1980. Transitional periodic boundary layer study. *Journal of the Hydraulics Division*, **106**, 1956–2071.
- ROBICHAUX, J., BALACHANDAR, S., & VANKA, S. 1999. Three-dimensional floquet instability of the wake of square cylinder. *Physics of Fluids*, **11**, 560–578.
- SALWEN, H., & GROSCH, C. 1972. The stability of poiseuille flow in a pipe of circular cross-section. *Journal of Fluid Mechanics*, **54**, 93–112.
- SARIC, W., & NAYFEH, A. 1975. Nonparallel stability of boundary-layer flows. *Physics of Fluids*, **18**, 945–950.
- SERGEEV, S. 1966. Fluid oscillations in pipes at moderate Reynolds numbers. *Fluid Dynamics*, **1**, 21–22.
- SEXL, T. 1930. Über den von E. G. Richardson entdeckten „Annulareffekt“. *Zeitschrift Für Physik*, **61**, 349–362.
- SHEN, S. 1961. Some considerations on the laminar stability of time-dependent basic flows. *Journal of the Aerospace Sciences*, **28**, 397–404.
- SINGER, B., FERZIGER, J., & REED, H. 1989. Numerical simulations of transition in oscillatory plane channel flow. *Journal of Fluid Mechanics*, **208**, 45–66.
- SLEATH, J. 1987. Turbulent oscillatory flow over rough beds. *Journal of Fluid Mechanics*, **182**, 369–409.
- SPALART, P. 1988. Direct simulation of a turbulent boundary layer up to  $R_\theta = 1410$ . *Journal of Fluid Mechanics*, **187**, 61–98.
- SPALART, P., & BALDWIN, B. 1989. Direct simulation of a turbulent oscillating boundary layer. *Turbulent Shear Flows* **6**, 417–440.

- STUART, J. 1987. Instability, three-dimensional effects, and transition in shear flows. *In perspectives in turbulence studies* (ed. H. U. Meier & P. Bradshaw), Springer, Berlin, 1–25.
- THOMAS, C., BASSOM, A., & BLENNERHASSETT, P. 2012. The linear stability of oscillating pipe flow. *Physics of Fluids*, 1–25.
- TOZZI, J., & VON KERCZEK, C. 1986. The stability of oscillatory hagen-poiseuille flow. *Journal of Applied Mechanics*, **53**(1), 187–192.
- TREFETHEN, L. 2000. *Spectral methods in matlab*. Society for Industrial and Applied Mathematics.
- TROMANS, P. 1978. *Stability and transition of periodic pipe flows*. Ph.D. thesis, Cambridge University.
- TRUKENMÜLLER, K. 2006. *Stabilitätstheorie für die oszillierende rohrströmung*. Ph.D. thesis, Helmut-Schmidt Universität, Hamburg.
- VILAINA, C., PELORSON, X., FRAYSSEB, C., DEVERGEB, M., HIRSCHBERGB, A., & WILLEMSB, J. 1989. Experimental validation of a quasi-steady theory for the flow through the glottis. *Journal of Sound and Vibration*, **276**(3), 475–490.
- VON KERCZEK, C., & DAVIS, S. 1974. Linear stability theory of oscillatory Stokes layers. *Journal of Fluid Mechanics*, **62**, 753–773.
- WHITE, F. 1991. *Viscous fluid flow*. New York: McGraw-Hill.
- WOMERSLEY, J. 1955. Method for the calculation of velocity, rate of flow and viscous drag in arteries when the pressure gradient is known. *Journal of Scientific Instruments (Journal of Physics E)*, **127**(3), 553–563.
- WU, X., LEE, S., & COWLEY, S. 1993. On the weakly nonlinear three-dimensional instability of shear layers to pairs of oblique waves: the Stokes layer as a paradigm. *Journal of Fluid Mechanics*, **253**, 681–721.

- YANG, W., & YIH, C. 1977. Stability of time-periodic flows in a circular pipe. *Journal of Fluid Mechanics*, **82**, 497–505.
- YOUNG, D., & TSAI, F. 1973. Flow characteristics in models of arterial stenoses-II. unsteady flow. *Journal of Biomechanics*, **6**(5), 547–559.
- ZHAO, M., GHIDAOU, M., KOLYSHKIN, A., & VAILLANCOURT, R. 2004. On the stability of oscillatory pipe flows. *Technische Mechanik*, **24**, 289–296.
- ZHAO, T., & CHENG, P. 1996. Experimental studies on the onset of turbulence and frictional losses in an oscillatory turbulent pipe flow. *International Journal of Heat and Fluid Flow*, **17**, 356–362.
- ZHOU, Z., ZHANG, J., ZHANG, Q., & LIU, R. 2018. Numerical modeling investigation on turbulent oscillatory flow over a plane rough bed composed by randomly arrayed particles. *Acta Oceanologica Sinica*, **37**(7), 62–68.

### Chebyshev Derivatives (CPSM)

A fourth-order partial differential equation written as

$$\begin{aligned} \frac{\partial}{\partial \tau} \left( \frac{\partial^2 H}{\partial \zeta^2} \right) + U \frac{\partial^3 H}{\partial \zeta^3} - \frac{1}{\zeta} \frac{\partial H}{\partial \zeta} - \frac{\partial^4 H}{\partial \zeta^4} \\ = e^{-3\tau} \left[ 360.028 \cos(2\pi\zeta) + \left\{ \frac{-1.5708}{\zeta} + 62.0126(\zeta^2 - 1) \cos(\tau) \right\} \sin(2\pi\zeta) \right], \end{aligned} \quad (1)$$

was solved, where  $U = \cos(\tau)(1 - \zeta^2)$ , and the function  $H$  satisfies the initial condition with four homogeneous boundary conditions shown below:

$$H(0, \tau) = H(1, \tau) = 0, \quad \frac{\partial H(0, \tau)}{\partial \zeta} = \frac{\partial H(1, \tau)}{\partial \zeta} = 0,$$

$$H(\zeta, 0) = 0.25(1 - \cos(2\pi\zeta)).$$

Chebyshev matrices for the spatial discretization are compared with the theoretical derivatives of function  $H$ , given by  $0.25(1 - \cos(2\pi\zeta))$ . An excellent agreement is obtained between the exact and numerical solutions as shown in Figure. 1 for the four derivatives ( $D_N$ ,  $D_N^2$ ,  $D_N^3$ , and  $D_N^4$ ).



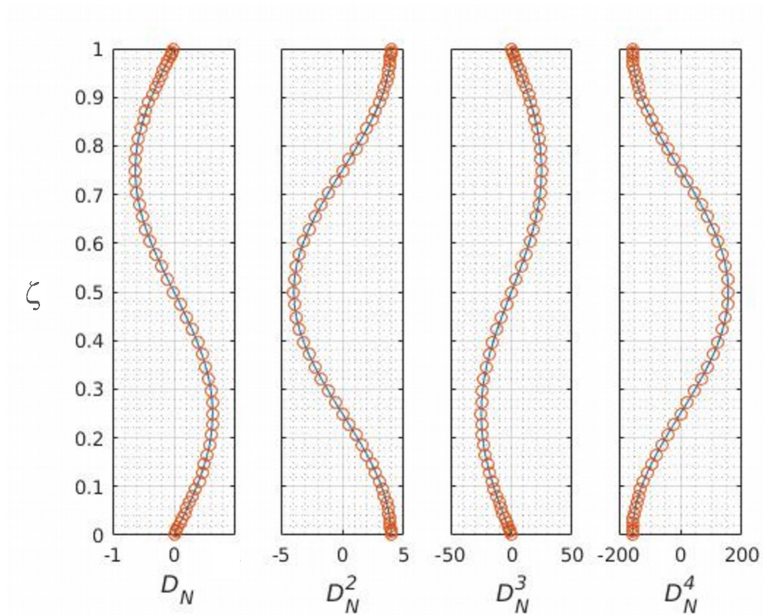


**Figure 1:** Chebyshev derivatives of the time-dependent function  $H$  appearing in Eqn. (1) along the radial direction: the exact solution obtained from  $0.25(1 - \cos(2\pi\zeta))$ , solid curves, and the numerical representations, circles.

The results of  $H$  and  $GR$  are found to be equivalent to the exact solutions. Figures 2 and 3 show the numerical solutions of Eqn. (1).

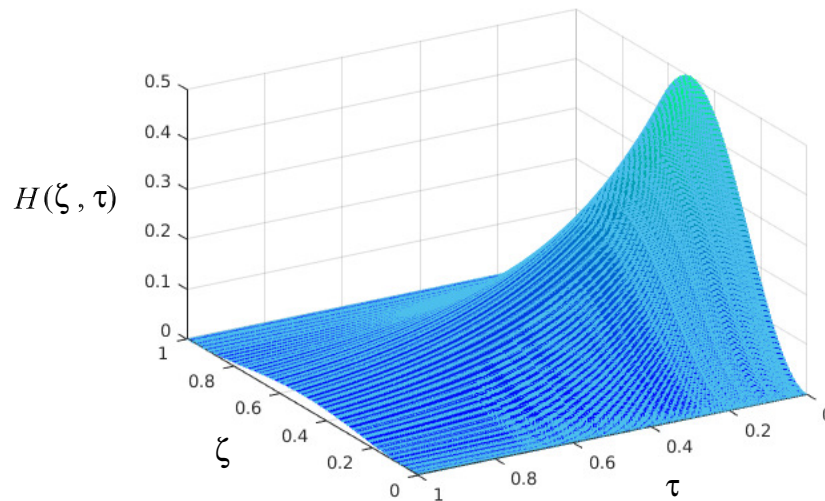


**Figure 2:** The instantaneous solution ( $H(\zeta, \tau)$ ) of Eqn. (1) utilized CPSM.

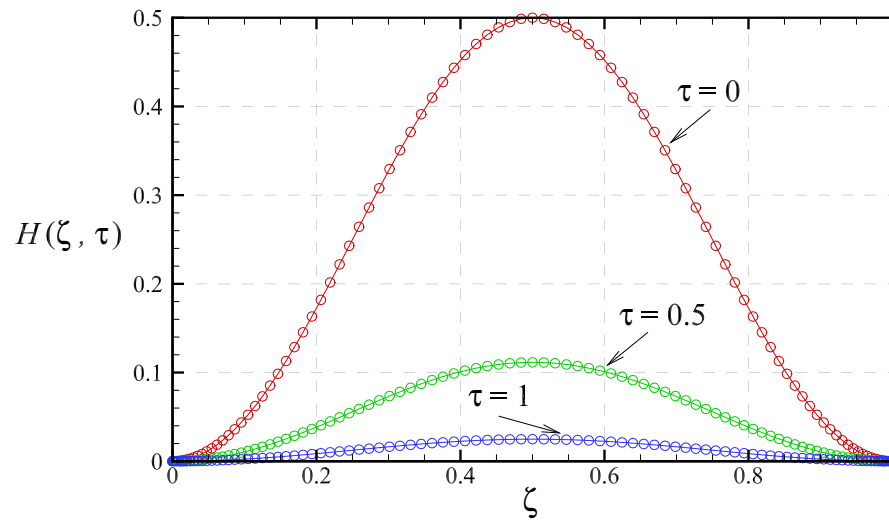


**Figure 3:** The instantaneous solution ( $H(\zeta, \tau)$ ) of Eqn. (1), circles, compared with the exact solution of  $0.25e^{-3\tau}(1 - \cos(2\pi\zeta))$ , solid curves, at three different times.

## Turbulence DNS data

**Table 1:** The friction Reynolds numbers, three-dimensional components of the velocity, gauge pressure fluctuations, Wall shear stresses, and Kolmogorov length scales at  $Re_\delta = 800$ ,  $\lambda = 10$ ,  $0 < E_z < 25$  and  $\tau/T = 3/8$ .

$Re_\tau$	$u^*$ (m/s)	$v^*$ (m/s)	$w^*$ (m/s)	$p^{*'} (Pa)$	$\tau_w^*$ ( $m^2/s^2$ )	$\Lambda^*$ (m)
501.169891	0.720685	-0.005313	0.00132	0.002875	0.000627928	0.000151407
501.16922	0.721063	-0.005245	0.001411	0.00287	0.000627926	0.000537784
501.168579	0.721949	-0.005084	0.001595	0.00286	0.000627925	0.00053778
501.167908	0.723279	-0.004848	0.001807	0.002846	0.000627923	0.000537776
501.167267	0.724838	-0.004595	0.001941	0.00283	0.000627922	0.000537771
501.166595	0.726285	-0.004389	0.00184	0.002814	0.00062792	0.000537767
501.165955	0.727318	-0.004256	0.001407	0.0028	0.000627918	0.000537763
501.165283	0.727863	-0.004184	0.000749	0.002788	0.000627917	0.000537759
501.164612	0.72806	-0.00415	0.000136	0.00278	0.000627915	0.000537755
501.163971	0.7281	-0.004138	-0.000176	0.002776	0.000627913	0.00053775
501.1633	0.720602	-0.005231	0.001332	0.002879	0.000627912	0.000537746
501.162628	0.720976	-0.005169	0.001424	0.002874	0.00062791	0.000537742
501.161987	0.721857	-0.005021	0.001612	0.002864	0.000627908	0.000537738
501.161316	0.723179	-0.004805	0.001831	0.00285	0.000627907	0.000537734
501.160675	0.724735	-0.004575	0.001976	0.002835	0.000627905	0.00053773
501.160004	0.726186	-0.00439	0.001891	0.002819	0.000627903	0.000537726
501.159332	0.727233	-0.004276	0.001477	0.002804	0.000627902	0.000537722
501.158691	0.727797	-0.004215	0.000836	0.002792	0.0006279	0.000537718
501.15802	0.728009	-0.004187	0.000235	0.002784	0.000627898	0.000537714
501.157349	0.728056	-0.004178	-0.000072	0.002781	0.000627897	0.00053771
501.156708	0.720428	-0.005027	0.001345	0.002889	0.000627895	0.000537707
501.156036	0.720796	-0.004979	0.001441	0.002884	0.000627893	0.000537703
501.155365	0.72166	-0.004863	0.001638	0.002874	0.000627892	0.000537699
501.154724	0.722962	-0.004693	0.001871	0.002861	0.00062789	0.000537695
501.154053	0.724502	-0.004516	0.002039	0.002845	0.000627888	0.000537692

**Table 2:** The friction Reynolds numbers, three-dimensional components of the velocity, gauge pressure fluctuations, Wall shear stresses, and Kolmogorov length scales at  $Re_\delta = 800$ ,  $\lambda = 10$ ,  $25 < E_z < 50$  and  $\tau/T = 3/8$ .

$Re_\tau$	$u^*$ (m/s)	$v^*$ (m/s)	$w^*$ (m/s)	$p^{*'} (Pa)$	$\tau_w^*$ ( $m^2/s^2$ )	$\Lambda^*$ (m)
501.153412	0.725956	-0.004383	0.001989	0.002829	0.000627887	0.000537688
501.15274	0.727031	-0.004309	0.001621	0.002814	0.000627885	0.000537684
501.152069	0.727634	-0.004277	0.001025	0.002803	0.000627884	0.000537681
501.151428	0.727881	-0.004264	0.000454	0.002794	0.000627882	0.000537677
501.150757	0.727946	-0.00426	0.000161	0.002791	0.00062788	0.000537674
501.150085	0.720215	-0.004689	0.001334	0.002903	0.000627879	0.00053767
501.149445	0.720571	-0.004661	0.001434	0.002899	0.000627877	0.000537667
501.148773	0.721407	-0.004593	0.001641	0.002889	0.000627875	0.000537663
501.148132	0.722667	-0.004493	0.001891	0.002876	0.000627874	0.00053766
501.147461	0.724169	-0.004397	0.002087	0.00286	0.000627872	0.000537657
501.14679	0.725611	-0.004341	0.002089	0.002844	0.00062787	0.000537653
501.146149	0.726713	-0.004331	0.001793	0.00283	0.000627869	0.00053765
501.145477	0.727369	-0.004342	0.001272	0.002818	0.000627867	0.000537647
501.144806	0.727666	-0.004354	0.000758	0.002809	0.000627865	0.000537643
501.144165	0.727755	-0.004359	0.00049	0.002806	0.000627864	0.00053764
501.143494	0.720022	-0.004227	0.001271	0.002921	0.000627862	0.000537637
501.142853	0.720361	-0.004224	0.001374	0.002917	0.00062786	0.000537634
501.142181	0.721155	-0.004213	0.001588	0.002908	0.000627859	0.000537631
501.14151	0.722349	-0.004198	0.001853	0.002895	0.000627857	0.000537628
501.140869	0.72378	-0.0042	0.002079	0.002879	0.000627855	0.000537624
501.140198	0.725182	-0.004239	0.002139	0.002864	0.000627854	0.000537621
501.139526	0.726293	-0.004307	0.001934	0.002849	0.000627852	0.000537618
501.138855	0.726998	-0.004374	0.001516	0.002836	0.00062785	0.000537615
501.138214	0.727351	-0.004419	0.001084	0.002828	0.000627849	0.000537613
501.137543	0.72747	-0.004437	0.000854	0.002824	0.000627847	0.00053761

**Table 3:** The friction Reynolds numbers, three-dimensional components of the velocity, gauge pressure fluctuations, Wall shear stresses, and Kolmogorov length scales at  $Re_\delta = 800$ ,  $\lambda = 10$ ,  $50 < E_z < 75$  and  $\tau/T = 3/8$ .

$Re_\tau$	$u^*$ (m/s)	$v^*$ (m/s)	$w^*$ (m/s)	$p^{*l}$ (Pa)	$\tau_w^*$ ( $m^2/s^2$ )	$\Lambda^*$ (m)
501.136902	0.71989	-0.00369	0.001145	0.002941	0.000627845	0.000537607
501.13623	0.720207	-0.003711	0.001249	0.002937	0.000627844	0.000537604
501.135559	0.720948	-0.003757	0.001467	0.002928	0.000627842	0.000537601
501.134918	0.722056	-0.003827	0.00174	0.002915	0.000627841	0.000537598
501.134247	0.723389	-0.003929	0.00199	0.0029	0.000627839	0.000537595
501.133575	0.724716	-0.004065	0.002105	0.002884	0.000627837	0.000537593
501.132935	0.725809	-0.004214	0.001997	0.002869	0.000627836	0.00053759
501.132263	0.726546	-0.004342	0.001696	0.002857	0.000627834	0.000537587
501.131622	0.726946	-0.004424	0.001362	0.002848	0.000627832	0.000537585
501.130951	0.727093	-0.004458	0.001179	0.002844	0.000627831	0.000537582
501.13028	0.719827	-0.003154	0.000972	0.002959	0.000627829	0.00053758
501.129608	0.720122	-0.003195	0.001075	0.002956	0.000627827	0.000537577
501.128967	0.720803	-0.003289	0.001291	0.002947	0.000627826	0.000537575
501.128296	0.721818	-0.003431	0.001568	0.002935	0.000627824	0.000537572
501.127655	0.723038	-0.003617	0.001832	0.00292	0.000627822	0.00053757
501.126984	0.724271	-0.003837	0.001991	0.002904	0.000627821	0.000537567
501.126312	0.72532	-0.004058	0.00197	0.002889	0.000627819	0.000537565
501.125671	0.726065	-0.004241	0.001781	0.002877	0.000627817	0.000537562
501.125	0.726496	-0.004358	0.001543	0.002868	0.000627816	0.00053756
501.124329	0.726663	-0.004407	0.001408	0.002864	0.000627814	0.000537558
501.123688	0.719811	-0.002702	0.00079	0.002975	0.000627812	0.000537555
501.123016	0.720083	-0.002757	0.000891	0.002972	0.000627811	0.000537553
501.122345	0.72071	-0.002883	0.001102	0.002964	0.000627809	0.000537551
501.121704	0.721639	-0.003075	0.001377	0.002952	0.000627807	0.000537549

**Table 4:** The friction Reynolds numbers, three-dimensional components of the velocity, gauge pressure fluctuations, Wall shear stresses, and Kolmogorov length scales at  $Re_\delta = 800$ ,  $\lambda = 10$ ,  $75 < E_z < 100$  and  $\tau/T = 3/8$ .

$Re_\tau$	$u^*$ (m/s)	$v^*$ (m/s)	$w^*$ (m/s)	$p^{*'} (Pa)$	$\tau_w^*$ ( $m^2/s^2$ )	$\Lambda^*$ (m)
501.121033	0.722756	-0.003322	0.001649	0.002937	0.000627806	0.000537547
501.120361	0.723897	-0.003602	0.00184	0.002921	0.000627804	0.000537544
501.11972	0.724892	-0.003876	0.001884	0.002906	0.000627802	0.000537542
501.119049	0.725627	-0.004101	0.001783	0.002893	0.000627801	0.00053754
501.118378	0.726073	-0.004246	0.001626	0.002884	0.000627799	0.000537538
501.117737	0.726252	-0.004307	0.001531	0.00288	0.000627797	0.000537536
501.117065	0.71981	-0.002393	0.000645	0.002986	0.000627796	0.000537534
501.116394	0.720066	-0.002456	0.000743	0.002983	0.000627794	0.000537532
501.115753	0.720653	-0.0026	0.00095	0.002975	0.000627792	0.00053753
501.115082	0.721519	-0.00282	0.001221	0.002963	0.000627791	0.000537528
501.11441	0.722562	-0.003102	0.001496	0.002949	0.000627789	0.000537526
501.11377	0.723635	-0.003417	0.001706	0.002933	0.000627787	0.000537524
501.113098	0.724585	-0.003724	0.001792	0.002917	0.000627786	0.000537523
501.112427	0.725306	-0.003974	0.001749	0.002904	0.000627784	0.000537521
501.111755	0.725756	-0.004138	0.001645	0.002895	0.000627783	0.000537519
501.111115	0.725941	-0.004207	0.001577	0.002891	0.000627781	0.000537517
501.110443	0.71981	-0.002259	0.000576	0.002991	0.000627779	0.000537515
501.109802	0.720059	-0.002324	0.000672	0.002988	0.000627778	0.000537514
501.109131	0.720627	-0.002475	0.000877	0.00298	0.000627776	0.000537512
501.108459	0.721465	-0.002706	0.001146	0.002968	0.000627774	0.00053751
501.107788	0.722475	-0.003001	0.001422	0.002954	0.000627773	0.000537509
501.107147	0.723516	-0.00333	0.00164	0.002938	0.000627771	0.000537507
501.106476	0.724446	-0.003649	0.001743	0.002923	0.000627769	0.000537505
501.105835	0.725159	-0.00391	0.001725	0.002909	0.000627768	0.000537504
501.105164	0.725609	-0.004081	0.001643	0.0029	0.000627766	0.000537502
501.104492	0.725795	-0.004153	0.001587	0.002896	0.000627764	0.000537501